Segmentation de l'os cortical pour la prédiction des fractures ostéoporotiques. Application à l'imagerie in vivo (HRpQCT).

Mohamed Hafri

Centre Val de Loire UNIVERSITÉ
Spirit of the Loire Valley

UNIVERSITÉ D'ORLÉANS

UNIVERSITE D'ORLEANS

ÉCOLE DOCTORALE SANTE, SCIENCES BIOLOGIQUES ET CHIMIE DU VIVANT

Laboratoire I3MTO - EA 4708

Thèse présentée par :

Mohamed HAFRI

soutenue le : **23 Novembre 2017**

pour obtenir le grade de : **Docteur de l'Université d'Orléans**

Discipline/ Spécialité : **Traitement du Signal et des Images**

Segmentation de l'os cortical pour la prédiction des fractures ostéoporotiques. Application à l'imagerie in vivo (HRpQCT)

Thèse dirigée par :

Rachid JENNANE	Professeur, Université d'Orléans
Eric LESPESSAILLES	HDR, Praticien Hospitalier, CHR Orléans

RAPPORTEURS :

Hervé DELIENGETTE	DR INRIA Sophia-Antipolis
Clovis TAUBER	Maître de conférences, HDR, Université de Tours

JURY :

Eva JAKAB-TOTH	DR - CNRS Orléans, Président du jury
Hervé DELIENGETTE	DR - INRIA Sophia-Antipolis
Clovis TAUBER	Maître de conférences, HDR, Université de Tours
Julien PACCOU	Praticien Hospitalier, HDR, Université Lille
Rachid JENNANE	Professeur, Université d'Orléans
Eric LESPESSAILLES	HDR, Praticien Hospitalier, CHR Orléans

Dedication

To those suffering in silence from Osteoporosis

‘My object is not to establish that I was right but to find out if I am. In fact we shall question everything all over again and we shall go forward not in seven-league boots but at a snail’s pace. And whatever we wish to find we shall regard, once found, with particular mistrust.’

Excerpt from Scene 9, Life of Galileo, Bertolt Brecht

Mohamed HAFRI

Segmentation de l'os cortical pour la prédiction des fractures ostéoporotiques. Application à l'imagerie in vivo (HRpQCT)

Résumé :
Cette thèse concerne la segmentation d'images HRpQCT et l'évaluation d'indices morphologiques de l'os cortical pour le diagnostic de l'ostéoporose et la prédiction des fractures osseuses. Dans un premier temps, deux méthodes sont proposées pour la segmentation de l'os cortical. La première utilise une nouvelle approche des contours actifs basée sur la logique floue suivie d'une nouvelle technique de remplissage développée pour imiter le comportement des opérateurs pour séparer l'os cortical de l'os trabéculaire. La deuxième approche est une technique 3D à double contours actifs combinant à la fois les informations locales le long et entre les deux contours. Les deux approches de segmentation sont comparées à celles de l'état de l'art afin de valider leurs performances. Dans un second temps, différents indices extraits de l'os cortical sont utilisés pour déterminer leur potentiel de prédiction des fractures ostéoporotiques. Les résultats obtenus montent que l'analyse globale de l'os cortical masque des variations potentiellement importantes. Par conséquent, une décomposition régionale de l'enveloppe corticale est proposée afin d'améliorer la prédiction du risque fracturaire.

Mots clés : Segmentation, contours actifs, ostéoporose, os cortical, fracture

Cortical bone segmentation for the prediction of osteoporotic fractures. Application in vivo (HRpQCT)

Abstract :
This thesis concerns the segmentation of HRpQCT images and the evaluation of the cortical bone parameters for the osteoporosis characterization and the fracture prediction. Firstly, two approaches were proposed to segment the cortical bone. The first uses a new fuzzy energy active contours approach followed by a new filling technique designed to mimic the behaviour of clinicians while extracting the cortical bone from the trabecular one. The second approach is a local based 3D dual active contours approach proposed to separate between three regions constituting the image. To move, this approach combines the local information along each point in the two contours conjointly with the information between them. The segmentation results of these approaches were confronted to the state of the art methods to validate their performance. Secondly, different parameters were extracted from the segmented cortical bone to monitor the association of these parameters with the osteoporotic fracture prediction. Global analysis of the cortical bone obscures potentially important regional variations. Therefore, regional cortical decomposition was proposed to illustrate that cortical sub-regions could improve the evaluation of fracture risk than the global analysis of the cortical bone.

Keywords : Segmentation, active contours, osteoporosis, cortical bone, fracture

Laboratoire I3MTO - EA 4708

Contents

Abstract **4**

1 Bone Tissue **5**

1.1 Introduction . . . 5

1.2 Structure of the bone . . . 6

1.2.1 Cortical Bone . . . 6

1.2.2 Trabecular Bone . . . 7

1.2.3 Bone Modeling and Remodeling . . . 7

1.3 Osteoporosis . . . 10

1.3.1 Definition . . . 10

1.3.2 Epidemiology . . . 11

1.3.3 Etiology . . . 12

1.4 Conclusion . . . 13

2 Bone Imaging **14**

2.1 Introduction . . . 14

2.2 Quantitative bone assessment . . . 15

2.2.1 Digital X-Ray Radiogrammetry . . . 15

2.2.2 Dual-energy X-ray absorptiometry (DXA) . . . 16

2.3 Qualitative bone assessment . . . 20

2.3.1 High-resolution MRI . . . 22

2.3.2 High Resolution peripheral Quantitative Computed Tomography (HRpQCT) . . . 23

2.4 Conclusion . . . 26

3 Image Segmentation using Active contours **27**

3.1 Introduction . . . 27

3.2 Active contours . . . 28

3.2.1 Snakes . . . 29

3.2.2 Level Set . . . 30

3.3 Methods . . . 31

3.3.1 Edge-based Active Contours . . . 31

3.3.2 Region-based Active Contours . . . 33
3.3.3 Local Region Based Active Contours . . . 35
3.3.4 Hybrid Active Contours . . . 37
3.3.5 Texture-based Active Contours . . . 38
3.3.6 Fuzzy Active Contours . . . 39
3.4 Conclusion . . . 41

4 HRpQCT Image segmentation 43
4.1 Introduction . . . 43
4.2 State of art methods . . . 43
4.2.1 Dual threshold . . . 43
4.2.2 Burghardt technique . . . 44
4.2.3 Valentinitsch technique . . . 45
4.2.4 Zebaze technique . . . 46
4.3 Subjects recruited in the study . . . 48
4.4 Quantitative metrics for evaluation . . . 49
4.4.1 Ground truth . . . 49
4.4.2 Dice similarity coefficient . . . 50
4.4.3 Absolute volume difference . . . 51
4.4.4 Hausdorff distance . . . 51
4.5 Conclusion . . . 52

5 Proposed Active Contours approaches for HRpQCT Image Segmentation 53
5.1 Introduction . . . 53
5.2 Method 1: Fuzzy energy based HRpQCT cortical bone segmentation . . . 53
5.2.1 Fuzzy energy active contours performance . . . 58
5.3 Method 2: Dual Active Contours . . . 61
5.3.1 Outer contour energy . . . 63
5.3.2 Inner contour energy . . . 64
5.3.3 Implementation . . . 67
5.3.4 DAC's performance . . . 67
5.4 Conclusion . . . 73

6 Osteoporotic Fractures Prediction 75
6.1 Introduction . . . 75
6.2 Extracted parameters from the cortical bone . . . 75
6.2.1 Global parameters . . . 75
6.2.2 Local parameters . . . 76
6.3 Database . . . 78

6.4 Statistical analysis 79
6.5 Results 81
6.5.1 Fracture prediction using cortical global parameters 81
6.5.2 Fracture prediction using the local cortical parameters 82
6.6 Discussion 85
6.7 Conclusion 87

A Statistic Tools used for Predictions **91**
A.1 Logistic regression 91
A.2 ROC Curves 92
A.3 Cox proportional hazard model 94

Bibliography **95**

List of Tables

2.1 The four diagnostic categories designed by WHO and IOF to assess Osteoporosis using T-score 18

2.2 Clinical Risk Factors Considered in FRAX tool 19

2.3 Definition and description of bone morphology parameters 21

5.1 Comparison of the accuracy of the different methods versus the ground truth in the case of the radius using different metrics 60

5.2 Comparison of the accuracy of the different methods versus the ground truth in the case of the tibia using different metrics 61

5.3 Comparison of the accuracy of the different methods versus the GT using different metrics 70

6.1 Description of the Employed Cortical and Porosity Parameters 76

6.2 Baseline characteristics of the employed database 79

6.3 The Statistical Performance of DAC and Xtreme CT Segmentation results on the Predictions of Fractures 82

6.4 The Statistical Classification Rates of the Local Cortical Parameters by Quadrant 84

6.5 Association Between Multiple HR-pQCT Cortical Bone Variables and Fractures Using Cox Model 85

A.1 Confusion Matrix 92

List of Figures

1.1 Illustration of the cortical and trabecular bone structure 6

1.2 The Bone Remodeling Cycle 8

2.1 Parameters that contribute to the bone strength. 15

2.2 The regions of interest used for the calculations of BMD in DXR 16

2.3 The sites scanned routinely for the calculations of BMD in DXA 17

2.4 Fracture rate, BMD distribution, and number of fractured based on NORA [29]. 18

2.5 FRAX algorithm for the assessment of fracture probability 20

2.6 Sphere fitting technique for trabecular thickness and separation measurement 21

2.7 Tibia scan of a patient using Xtreme CT scanner (a), the scout view (b), and 2D ultra-distal scan of tibia (c) and distal scan (d) 23

2.8 The bone quality parameters extracted from the HRpQCT images 25

3.1 Active Contours Models 28

3.2 Segmentation result of edge based technique (geodesic active contours [97]) left and region based (active contours without edges [85]) right 34

3.3 Segmentation result of local based active contours against global. (a) the initialization of the contours, (b), (c), and (d) are the segmentation results of the Chan veze [85], Chunming [112] and Lankton [113] respectively . . . 35

3.4 The segmentation result of the local [112], hybrid [147] and fuzzy hybrid [148] techniques on two heart MR images respectively. Source [148] 41

4.1 Summary of the two steps to extract the cortical bone in the Dual threshold techniques. Source [151] 44

4.2 Summary of the two steps to extract the cortical bone in the Burghardt techniques. Source [59] 45

4.3 (A) HRpQCT distal slice of the radius, where the Arm originates from 'C' to P0. (B) A magnification of the Arm to show its contents (background, and bone edges). (C) The attenuation profile. The zone 'K' to 'M'is the transitional zone between background and cortical (excluded in their study). The zone 'M' to 'N' and 'O' to 'C' are the cortical and trabecular compartments respectively. Finally, the zone 'N' to 'O' is the transitional zone between cortical and trabecular [160]. 47

4.4 2D segmentation result of radius produced by the operator using ITK-SNAP (a), 3D Reconstruction of the segmentation result using ITK-SNAP (b) 50

5.1 The minimization algorithm of the proposed fuzzy active contours energy. 56

5.2 Segmentation results on ultra-distal slice of radius, using (a) proposed approach, and (b) FEBAC method 57

5.3 An example of a background pixel (value = 0) surrounded by four bone pixels (value = 1). In this case, the value of the background pixel turns to 1. A pixel of value = *, is either 0 or 1. 57

5.4 The flowchart of the proposed algorithm to extract the cortical bone . . . 59

5.5 Comparison between the result of the manual segmentation (GT) and the different approaches in the case of the tibia (first row) and the radius (second). Highlighted in red are the over-estimation of the mask. The cortical breaks (highlighted in green) are apparent on all the approaches except in our proposed technique. 61

5.6 The neighbourhood of each point x (black small dot) along both curves is represented by the spheroid $S(x, .)$. This spheroid is split by the contour into local interior (green = u_x) and local exterior (blue = v_x) (a). The spheroid of each point along the curve C_2 is split by the two contours C_1 and C_2 and only the region between them is considered (green) (b). 62

5.7 Convergence and timing properties of DAC. The inner contour starts evolving at the iteration 85 where the outer contour converged. 68

5.8 Results of the segmentation using the proposed DAC approach (b, e) and Lankton [113] (c, and f)on synthetic images created from Brodatz database and using the same contour initialization (a, and d) 69

5.9 The segmentation result of the proposed DAC approach and Lankton [113] applied on radius bone HRpQCT image (first row) and bladder wall MRI (second row) 70

5.10 Comparison between the result of the manual segmentation (GT) and the different approaches in the case of radius. Cortical breaks are highlighted in red, they are apparent on all the approaches except in DAC. 71

5.11 The effect of the radius $R_{x,y}$ on the convergence of the outer curve, the 30 pixels radius is represented in red in (a) and the 10 pixels one is in blue. A good segmentation result is achieved using $R_{x,y} = 30$ pixels in (b). The non incorporation of the bone pixels in $R_{x,y} = 10$ pixels provides a bad segmentation result (c). 71

5.12 The obtained inner contour using $R_{x,y} = 30$ pixels (a) and $R_{x,y} = 10$ pixels (b). 72

5.13 Initial contours distance effect 73

5.14 The effect of bad and good initialisation result 73

5.15 The proposed pre-processing algorithm to initialize DAC method. 74

6.1 Illustration of the different steps to calculate the average cortical thickness, of a 2D distal radius slice (a), followed by the Euclidean distance transform (b), and the local maxima (c) 76

6.2 In red, the ellipse fitted to the ultra-distal scan of the radius bone using least squares method. The four quadrants used for the regional analysis are also illustrated. 78

6.3 ROC curves for a composite clinical variables, cortical parameters, porosity parameters, and all the previous models using (a) the DAC's segmentation result(b) Xtreme CT technique result 81

6.4 ROC curve for the “Quadrant 1”of the radius bone using the four models . 82
6.5 ROC of the “Quadrant 2 ”parameters of the cortical bone of the radius . . 84
6.6 ROC curve of the “Quadrant 3”parameters of the cortical bone of radius using the four models 86
6.7 ROC curve of the “Quadrant 4”parameters of the cortical bone of the radius using the four models 86

A.1 Example of ROC curve. The blue dotted line corresponds to the ideal curve with sensitivity and specificity equal to 1. The gray area symbolizes the area under the curve (AUC). 94

Introduction

Motivations

Osteoporosis is a skeletal pathology characterized by a decrease in the bone density and a change (deterioration) in the bone micro-architecture. As bones become more porous and fragile, the risk of bone fracture is greatly increased. This pathology is usually referred as a silent disease, because, often there are no symptoms until the first fracture occurs. This leads to an alteration of the quality of the life or even to the death of the patient.

The bone is a living, growing tissue that undergoes a constant cycle of bone modeling/remodeling throughout life. This process ensures that old damaged bone is removed and replaced with a new, mechanically stronger bone to preserve the bone rigidity and strength. Osteoporosis appears when an imbalance in this cycle (modeling/remodeling) happens. This occurs with the skeleton aging and different other factors, such as: tobacco, alcohol consumption, menopause,etc.

Each bone is composed of two compartments, cortical and trabecular bone. The cortical bone is the solid outer shell and trabecular bone is the inner mesh of spongy look. After menopause, the bone loss is more apparent in the trabecular bone than it is in the cortical one. Therefore, researches have been focused on studying the relationship between the trabecular bone and the fragility fractures, neglecting the role of the cortical bone. Despite the fact that about 80% of fractures in old age arise at sites that are mainly cortical, and happen after the age of 65, where most bone loss is cortical, not trabecular.

With the population aging, bone pathologies in particular osteoporosis have become increasingly widespread along with an increase in the associated care cost. Therefore, different imaging technologies have been developed to further comprehend these pathologies and monitor the response or nonresponse to therapies. Among the different imaging technologies, High Resolution peripheral Quantitative Computed Tomography (HRpQCT)

technique is considered one of the most interesting developments to assess the bone strength. This technology opened a new perspectives in the three dimensional *in-vivo* exploration of the bone tissue with a high resolution of $\sim 82\mu m$. Along this advancement in image acquisition and quality, different parameters of the cortical and trabecular bone are now available. However, an accurate extraction of these parameters depends mainly on the employed segmentation technique to separate the cortical and trabecular bones.

This thesis is therefore focused on studying the cortical bone, which represents 80% of the human skeleton. Acquisitions from HRpQCT scanner allowed us to analyze the cortical bone in the radius and the tibia sites.

Objectives

Image segmentation is the first step in structural image analysis. It simplifies the understanding of the image by dividing it into meaningful structures (regions). In our case, it is the problem of separating between the cortical and trabecular bone in HRpQCT images. Defining an accurate image segmentation method is a challenging task, because it affects the results of all the following steps. Several segmentation techniques have been proposed in the literature. Among the state of the art techniques, Active Contours Models have received more attention and have been extensively used in medical image segmentation.

Active Contours, as the name implies, its idea is based on evolving a contour (also referred as a curve) in the image domain using two forces. The first one, often called external force, pulls the contour towards the features of interest. The other one, often called internal force ensures the smoothness of the contour during evolution.

Based on Active Contours Models, we have proposed two approaches to segment cortical bone in HRpQCT images. The first approach consists of a new fuzzy energy active contours approach, to segment the bone (cortical and trabecular) in HRpQCT images. Afterwards, a post-processing algorithm is used to separate the two bones. The second approach is a novel 3D dual active contours technique able to segment the cortical bone and its erosions automatically. This approach introduces a new concept, where the two contours evolve minimizing a shared energy, to encapsulate the object of interest between the two contours.

The performance of these two approaches is performed on the QUALYOR database.

Different similarity measures are used to validate the performance of the two proposed approaches compared to state of the art techniques.

Furthermore, an additional objective of this thesis is to predict the osteoporotic fractures. After the image segmentation step, we quantified the different cortical parameters to establish a relationship between these parameters and patients prone to fractures. The predictive capabilities of the proposed approach were compared with the HRpQCT scanner. Based on these results, we deduced that global analysis of the cortical bone obscure potentially important regional variations. Therefore, the second study focused on partitioning the cortical bone to four regions to study the association between the regional cortical parameters and the incident Fractures.

Thesis Plan

This thesis is divided into three parts. The first part consists of 2 chapters, that present successively notions on bone tissue, osteoporosis, and then state of the art on imaging modalities.

Chapter 1 presents bone tissue. The characteristics of the later, whether chemical, cellular or histological are discussed. Then a detailed description of the bone tissue remodeling phase is explained, and how an alteration of its mechanism can be of concern for bone loss (osteoporosis). The etiology and epidemiology of this disease in worldwide and in France in particular is also discussed.

Chapter 2 is devoted to the state of the art of different imaging methods to characterize the bone tissue. These techniques have been categorized into two groups based on the provided information (Bone density and quality). The advantages and disadvantages of each method are discussed in particular the case of HRpQCT images. Finally, the application of these techniques to predict osteoporotic fractures is illustrated.

Chapter 3 provides the state of the art of image segmentation methods with a particular focus on active contours. A detailed survey of the latter is given. Based on the external force, the active contours techniques are divided into two categories. One uses the edge information and the other uses the pixels variations. Furthermore, different variations of active contours are also outlined.

The second part of the thesis is composed of two chapters outlining the two first contri-

butions of this work.

Chapter 4 presents the HRpQCT Image segmentation problem, starting briefly with the state of the art techniques. Then, a detailed presentation of the database QUALYOR of patients used for the segmentation and for the prediction of osteoporotic fractures is provided. Finally, the different similarity metrics used for the performance validation are provided.

Chapter 5 details the proposed active contours based HRpQCT segmentation methods. Starting with the first proposed fuzzy energy active contours method to segment the bone from background, followed by a post-processing algorithm applied to separate the cortical and trabecular bones. The second contribution consists in the 3D Dual active contours. This approach presents a novel framework of active contours that employ the energy of two curves to segment objects that share the same intensity level with different textures.

Chapter 6 is dedicated to the use of the proposed segmentation techniques in identifying patients prone to fractures. A local cortical region study was evaluated to demonstrate the fact that global analysis can obscure potentially important regional variations in the cortical structure.

Finally, this manuscript is concluded with a brief summary of the thesis, and prospects for future studies.

Chapter 1

Bone Tissue

1.1 Introduction

Despite appearing dry and lifeless, the human bone is a highly specialized supporting framework of the body, characterized by its rigidity, hardness, and power of regeneration and repair. Therefore, before discussing methods of characterization of the bone, it is useful to recall the bone structure and physiology to further understand the different bone pathologies, in particular osteoporosis.

The bone is made mostly of collagen protein which provides a soft framework, and a calcium phosphate mineral which adds strength and hardens the framework. The bone is mostly composed of two components, cortical and trabecular bone. The cortical bone is a thick and solid outer shell that surrounds the marrow space, and the inner bone (Figure 1.1). The second component is an inner mesh of spongy look known as cancelous or trabecular bone, with blood and bone marrow between the struts of bone [1] (Figure 1.1).

The bone is a living, growing tissue that undergoes a constant cycle of bone modeling/remodeling throughout life to remove old, damaged bone and replace it with new, mechanically stronger bone to preserve the bone strength. With the skeleton aging, coupled with several factors an imbalance in the bone remodeling process occurs, hence, a modification of the mechanical properties of the skeleton resulting in a weak and fragile bones prone to fractures. This leads to a disease called osteoporosis.

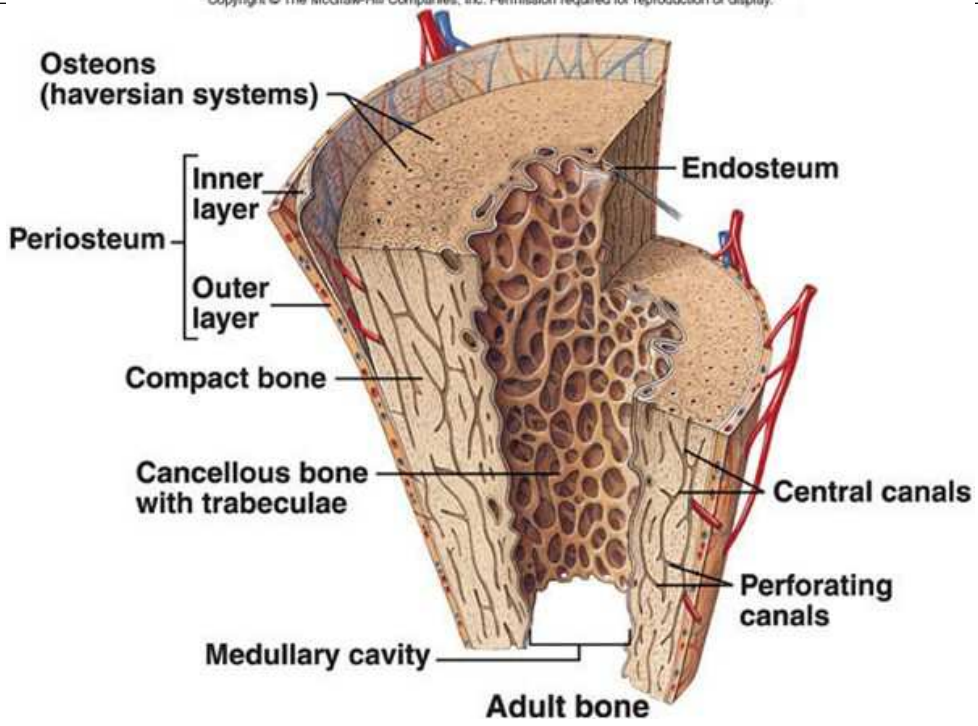

Figure 1.1: Illustration of the cortical and trabecular bone structure
https://basicmedicalkey.com/skeletal-tissues/

1.2 Structure of the bone

The adult human skeleton is composed of 80% cortical (compact) bone and 20% trabecular (spongy) bone [2]. As the name of the two bones imply, they are different in density and how tightly the bone tissue is packed together.

1.2.1 Cortical Bone

Cortical bone is the firmer thick outer layer of bone tissue which supports the whole body weight and covers the internal surface. At microscopical level (Figure 1.1), the cortical bone is composed of closely packed osteons also referred as Haversian systems. These osteons consist of a set of rings (lamellae) centred over a canal called the Haversian canal. Between these rings, the bone cells (osteocytes) are located in spaces called lacunae. The Haversian canals contain blood vessels that are parallel to the long axis of the bone. These blood vessels interconnect through perforating canals (Volksman), with the vessels on the surface of the bone.

Cortical bone is enclosed by an outer, and inner surfaces called periosteal and endosteal surfaces, respectively. The periosteum (outer surface) is a membrane that surrounds the cortical bone, except at joints where the bone is lined by articular cartilage. It protects, nourishes, aides in the bone formation, and plays an important role in appo-

sitional growth and fracture repair.

The endosteum is a membranous structure covering the inner surface of cortical and cancellous bone and the blood vessel canals (Volkmann's canals) present in bone. [3]

1.2.2 Trabecular Bone

Compared to cortical, the trabecular bone is lighter and less dense, it can be found at the end of long bones and within the interior of vertebrae. Microscopically (Figure 1.1), trabecular bone consists of plates (trabeculae) and bars of bone adjacent to small, irregular cavities that contain red bone marrow. It may appear that the trabeculae are arranged in a haphazard manner, but actually they are organized so as to provide a maximum strength to the bone, similar to braces that are used to support a building. The trabeculae of spongy bone follow the lines of stress and can realign if the direction of stress changes. [3]

The bone constantly undergoes the process of regeneration, reshape and repair during lifetime to help it adapt to changing biomechanical forces, and also remove old, micro-damaged bone and replace it with new, mechanically stronger bone. This two processes are referred as bone modeling and remodeling.

There are three types of cells that contribute to bone homeostasis. Osteoblasts, Osteoclasts, and Osteocytes. Osteoblasts are the bone-forming cells that create new bone, Osteoclasts are the bone-resorbtion cells that remove and break down bone, and osteocytes are mature bone cells. An equilibrium between osteoblasts formation and osteoclasts resorbtion maintains the bone tissue status.

1.2.3 Bone Modeling and Remodeling

Throughout one's lifetime, the human skeleton changes its size and shape, and this is characterized predominantly by two processes : bone modeling and remodeling.

Bone Modeling

The bone modeling (reshaping) occurs intensively in the first two decades where it involves the growth throughout the childhood and shaping of the bone. It can also occur following a bone fracture or mechanical stress. Therefore, during this process, bones widen

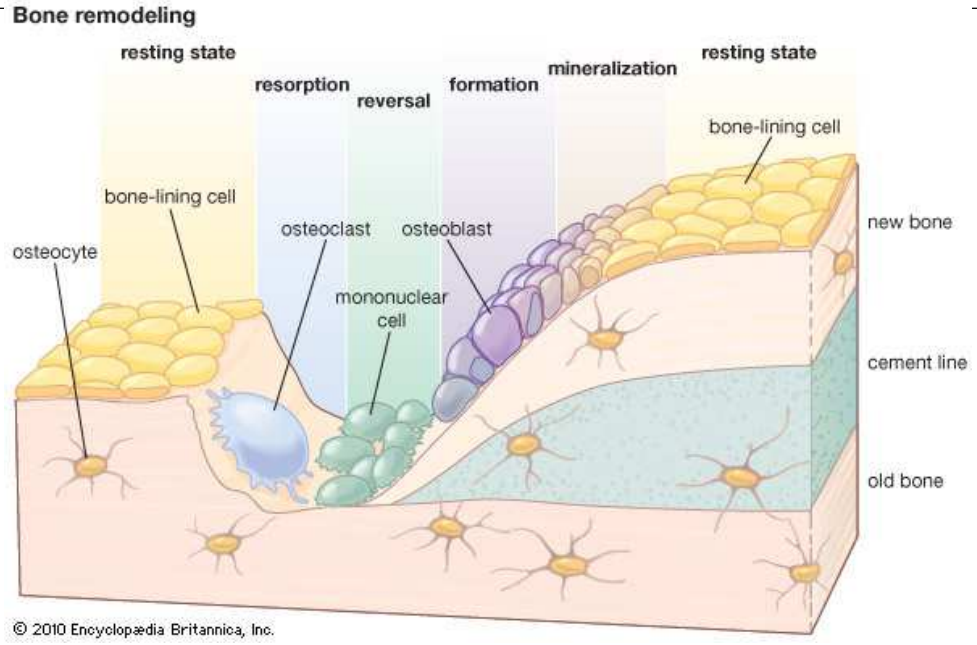

Figure 1.2: The Bone Remodeling Cycle. Source : Encyclopedia Britannica

and/or change their overall shape in response to physiologic influences or mechanical forces as described by Wolff's law, leading to gradual adjustment of the skeleton to the forces that it encounters.

In response to bio-mechanical forces and fractures, bones change and old damaged bone tissue are removed and replaced by a new bone tissues on the affected surfaces.

Bone Remodeling

Bone remodeling is a lifelong process wherein old damaged bone tissue is removed (a subprocess called bone resorption) and new bone tissue is added (a subprocess called bone formation). It is estimated that 5 to 10% of the skeletal is renewed each year. In addition to being a process that happens continuously and throughout life, bone remodeling can occur following injuries like fractures and also bone micro-damage to prevent damage accumulation which can happen following normal activities [4]. Furthermore, bone remodeling also responds to mechanical loading. This explains the fact that bone can be added into certain locations where it is required and removed where it is not.

Normal bone remodeling cycle requires a balance between the bone resorption and bone formation. This balance depends on the activation of two cells, osteoclasts for resorption and osteoblasts for formation. Based on the development of these two cell types, the bone remodeling cycle can be divided into the following six states:

- Quiscent Phase: the bone is at rest- where bone cells are seen layed on the endosteal

surface.

- Activation Phase: as the name implies, this phase is the activation of the endosteal surface prior to resorption. This phase includes an interaction between the osteoclast and osteoblast precursor cells. This leads to the differentiation, migration, and maturation of osteoclasts which will be attached to the mineralized bone surface to start resorption [5, 6].
- Resorption Phase: The matured osteoclasts start dissolving mineralized bone and degrading the bone matrix.
- Reversal Phase: it is the phase where osteoblasts finished resorption and signals has been emitted to announce the end of bone resorption and the beginning of bone formation. These signals are yet to be identified[3].
- Formation Phase: the osteoclasts are replaced by osteoblasts with underlying new osteoid matrix
- Mineralization Phase: 30 days after the depostition of new osteoid and under the action of phosphatases secreted by the osteoblasts, the mineralization phase begin. This process lasts 3 months in the trabecular bone and more than 4 months (130 days) in the cortical one.

The skeleton is a metabolically active organ that undergoes continuous remodeling throughout life which is estimated to take a duration of 2-8 months. The main functions of the bone remodeling process are the preservation of structural integrity and stiffness of the skeleton, and also maintaining the calcium and phosphorus homeostasis to subserve metabolic functions. Until reaching the bone mass peak (30 years), the two subprocess (resorption and formation) are positively balanced. From this stage, resorption will dominate the formation gradually reducing the bone mass resulting in certain cases a very fragile bones, referred as the osteoporosis disease.

For women, bone loss is fastest in the first few years after menopause, and it continues into the post-menopausal years. Osteoporosis which mainly affects women but may also affect men will develop when bone resorption occurs too quickly or when replacement occurs too slowly. Osteoporosis is more likely to develop if you did not reach optimal peak bone mass during your bone-building years.

1.3 Osteoporosis

1.3.1 Definition

According to the World Health Organization, Osteoporosis, or porous bone, is a disease characterized by low bone mass and structural deterioration of the bone tissue, leading to bone fragility and an increased risk of fractures of the hip, spine, and other skeletal sites [7].

Beyond the third decade, an imbalance in the mechanisms of bone formation and resorption is noticed in favor of the latter. With the skeleton aging, this imbalance is further heightened, hence a modification of the mechanical properties of the skeleton resulting in a weak and fragile bones prone to fractures. When the the risk of fractures is particularly high, this stage is then considered as osteoporosis.

The amount of bone loss relies predominately on the remodeling process. This process is initiated on the surfaces of the bone. Hence, it is obvious that a bone with a large exposed surface will be remodeled rapidly [8]. This justifies the fact that trabecular bone which has a bigger bone surface is more exposed to bone remodeling compared to the cortical bone [8]. Therefore, bone loss is more apparent in the trabecular bone than it is in the cortical. This finding coupled with fractures of the vertebral body, which is a structure containing large amounts of trabecular bone, have shifted the focus of the researchers, on only studying the relationship between the trabecular bone and fragility fractures [9, 10]. This neglects the role of the cortical bone in bone pathologies and in particular bone loss (osteoporosis). Despite the fact that, about 80% of fractures in old age are non-vertebral, and arise at sites that are mainly cortical, and happen after the age of 60, when the rate of trabecular bone loss decelerates [11].

A recent study [12] has prevailed contrary to previous views, that the peripheral bone loss in the first 15 years after menopause makes only a small contribution to the total bone loss. Moreover, most old age fractures occur at predominately cortical sites after the age 65, where most bone loss is cortical, not trabecular [13]. This what motivated the research conducted in this thesis concerning the segmentation and the characterization of the cortical bone.

1.3.2 Epidemiology

Prevalence

Due to the impact on the quality of life and economic burden induced by fractures, osteoporosis has become a major public health issue throughout the world [14]. Approximately 200 million people in the world are osteoporotic and 8.9 million fractures occur each year worldwide [15]. This is related to the growing percentage of the elderly population worldwide, as people age, bone mass declines and therefore the risk of fractures increases. Here are some statistical facts about France:

- 4 out of 10 women over the age of 50 are affected by osteoporosis as 1 out of 8 men are.
- After 80 years of age, 70% of women are osteoporotic.
- 50,000 to 150,000 new cases of vertebral fractures occur each year.
- The mortality rate is higher in men (10-14% versus 5% in women) related to the lifestyle.
- The morbidity rate is also important: 50% of patients with hip fractures permanently lose their independence.

Economic burden

In 2010, osteoporosis cost the French health system approximately €4.9 billion, with an annual cost projected to approach €6.1 billion by the year of 2025. [16] These medical costs include first year costs, subsequent year costs and pharmacological fracture prevention costs amounted in 2010 to €3.179 billion, €1.329 billion and €346 million, respectively.

This increase of cost is proportionally related to the number of elderly population (over age 50) which expected to increase from 22,6 million in 2010 to 27,1 million in 2025 [16]. And because osteoporosis is a silent disease, the majority of this population doesn't find out that they have osteoporosis until a fracture occurs. Therefore, the total number of fractures is estimated to rise from 377,000 in 2010 to 491,000 in 2025. [16] The hip, vertebrae and forearm are the three main sites of osteoporotic fractures. Due to the importance of the consequences on the quality, and the lifetime of the patient, fractures of the hip and vertebrae are the most monitored. Hip fractures are associated with

increased hospitalizations and surgical procedures. These operations lead to prolonged or permanent immobilizations and are associated with mortality. In fact, in about 20% of the cases, death occurs in the year following the fracture [17]. This is due, in particular to the cardiac, pulmonary or infectious complications that can occur rapidly after surgery in the elderly population [36]. On the other hand, vertebral fractures can induce pain, severe deformations of the column, and mortality [18].

1.3.3 Etiology

There are four types of osteoporosis: primary, secondary, osteogenesis imperfecta, and idiopathic juvenile. Primary osteoporosis is the most common type of osteoporosis, it is related to skeletal senescence and menopause in women. Secondary osteoporosis is much less frequent, it occurs as a result of taking certain medicines, such as oral or high-dose inhaled corticosteroids. It may also happen as a result of metabolic or endocrine diseases. The third type is Osteogenesis imperfecta, which is a rare form of osteoporosis that is present at birth and can cause bone breaks for no apparent reasons. Another rare form of osteoporosis is the Idiopathic juvenile osteoporosis which occurs only on children between the age of 8 to 14.

In this manuscript, only the primary osteoporosis is studied. It affects both men and women of 70 years of age or higher. It is a multi-factorial disease, and several epidemiological surveys have gathered the different risk factors:

- Menopause is the main risk factor for osteoporosis, because of the sudden decrease in estrogen levels [19]. Estrogen deficiency increases bone resorption by increasing the number of osteoclasts (by promoting their formation and decreasing their apoptosis) while stimulating their activities [20].
- Genetic factors: a family history of fractures, particularly, hip fractures [21]
- Nutritional and environmental factors: low calcium intake, vitamin D deficiency, alcoholism, smoking, physical inactivity, leanness [22].
- Occurrence of a first fracture event: vertebral compression or non-vertebral fracture.
- Taking medicines for the treatment of certain conditions such as rheumatoid arthritis, hyperthyroidism, hypercorticism, etc.

As previously mentioned, menopause is the main risk factor for osteoporosis, therefore, our study was carried out on a population of menopausal women. In this type

of population, bone loss was significantly associated with an increased risk of fracture [23, 24].

1.4 Conclusion

In this chapter, different informations concerning the bone tissue were presented, including its structure and functions, finishing with the osteoporosis disease along with its epideomiology and etiology. The public health impact of this pathology justifies the interest in developing more efficient and less costly methods to characterize the bone tissue and estimate the bone fragility resulted by this disease. Bone strength reflects the integration of 2 main features, bone density and bone quality. Based on these features several imaging techniques have been proposed such as DXA, CT, MRI, HRpQCT, etc. The following chapter provides a detailed survey of existing imaging technologies regarding the osteoporosis disease.

Chapter 2

Bone Imaging

2.1 Introduction

Osteoporosis is the most common metabolic bone disorder, characterized by a compromised bone strength resulting in brittle bones that can break easily [25], leading to a chronic pain, deformity and reduced mobility. Unfortunately, while treatments for osteoporosis are in place, currently no cure exists [26]. However, an early diagnosis of the bone status can help prevent the osteoportic fractures [27]. This preventive system is based on the use of pharmacotherapy which needs a clear guidelines to be initiated, because they are expensive and can produce side effects [28]. Therefore, diagnostic imaging techniques should be put in place to monitor and assess the response or nonresponse to these pharmacotherapies. In the last decades, the gold standard for assessing the bone strength in osteoporotic studies was based on the Bone Mineral Density (BMD). However, different studies [29, 30] have illustrated that BMD is not an accurate predictor for osteoporotic fractures. This is because BMD alone does not reflect the bone strength, as it needs to be integrated with the bone quality (Figure 2.1)[31, 32]. Bone quality is characterized by bone geometry, turnover, microarchitecture, modeling/remodeling, and material content (mineral, collagen, crystal structure and micro-damage) [33]. Correctly diagnosing and interpreting fragility fractures with all available imaging modalities is one of the major responsibilities facing the osteoporosis studies.

In this chapter, the use of the early methods of quantitative skeletal assessment based on BMD in particular Dual-energy X-ray Absorptiometry (DXA) and its advantages and disadvantages are discussed. Furthermore, qualitative skeletal assessment techniques to

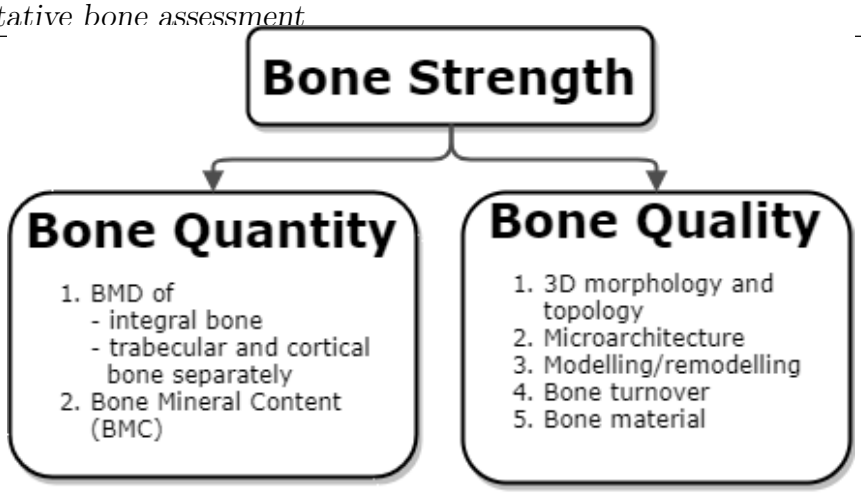

Figure 2.1: Parameters that contribute to the bone strength.

study the bone microarchitecture are examined with a particular focus on High Resolution peripheral Quantitative Computed Tomography (HRpQCT). Finally, the different parameters extracted from these imaging modalities and their feasibility in the fracture prediction are discussed.

2.2 Quantitative bone assessment

2.2.1 Digital X-Ray Radiogrammetry

Radiogrammetry is the first quantitative method of skeletal assessment. This technique uses the conventional radiographs to make quantitative measurements of the bone, such as cortical thickness and width. This method was most commonly applied to the diaphysis of the second metacarpal of the non-dominant hand, with the cortical thickness measured and calculated as a percentage of the midshaft bone diameter of the 'metacarpal index'.

An automated digital version of this, referred as Digital X-ray Radiogrammetry (DXR) was described in [35, 34]. The basic concept of this methodology is to automatically locate several regions around the digital hand radiographs and segment the diaphysis into cortical and medular parts (Figure 2.2). From this segmentation, the average thickness, width and porosity of the cortical bone are calculated to provide an estimate of the metacarpal BMD using the following formula:

$$BMD_{DXR} = c \times VPA_{comb} \times (1 - p) \tag{2.1}$$

Figure 2.2: The regions of interest used for the calculations of BMD estimate are shown as the highlighted areas. In the metacarpals, the cortical thickness is determined on both sides (radial and ulnar sides), while in the radius and ulna only the radial and ulnar sides respectively are used. **Source** [34]

where, c is an empirical density constant used to calibrate the BMD_{DXR} so that the BMD_{DXR} on average is equal to the BMD_{DXA} of the mid-distal forearm region, p is the fraction of the cortical bone that is not occupied by bone [36], and VPA_{comb} is the combined bone Volume Per Area, and is the average VPA of each bone regions. The VPA of a single bone is computed assuming that this bone is cylindrical, T is its cortical thickness and W is its width. :

$$VPA = \pi \times T \times (1 - T/W) \tag{2.2}$$

In the case of the short term in vivo precision, the coefficient of variation (CV) of this technique is reported to be between 0.60% and 1.00%. This high level of precision can capture the changes in BMD over short periods (6 – 12 months) of follow-up. Furthermore, in osteoporotic studies, DXR has been shown to predict hip, wrist and vertebral fractures[37, 38, 39].

2.2.2 Dual-energy X-ray absorptiometry (DXA)

DXA introduced to clinical use in 1987 is the most widely used technique for bone densitometry in research studies and clinical diagnosis [40]. The patient is radio-graphed

with two X-Ray beams with differing peak kilo-voltage (30–50 and 70 keV) that allows it to subtract the soft tissue component. This enables the measurement of the areal BMD on the lumbar spine (L1–L4), proximal femur, and distal radius (Figure 2.3).

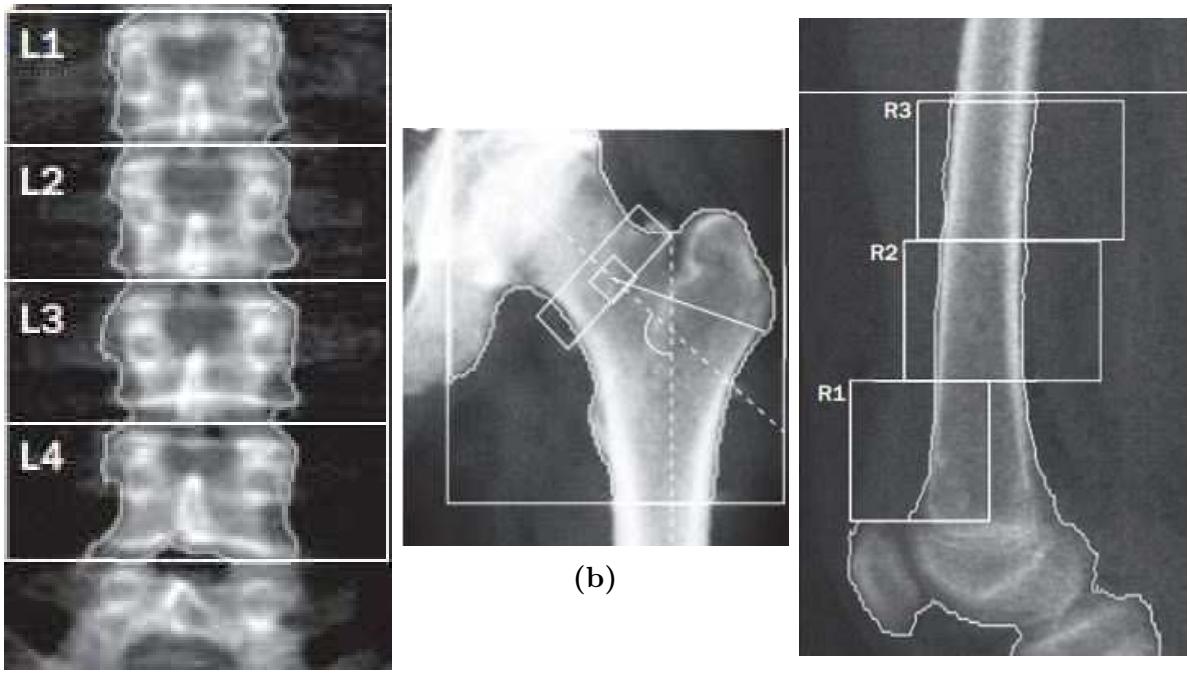

(a) (b) (c)

Figure 2.3: The sites scanned routinely, and from which diagnosis of osteoporosis is made, are (a) lumbar spine L1–L4, (b) proximal femur neck, and (c) distal femur.

In addition to the areal BMD (in g/cm2), this technique provides other parameters such as: bone mineral contents (BMC in g/c^2m), bone area (cm^2), T scores and Z scores. T scores are standard deviations compared with a young adult reference population, while Z scores are standard deviations compared with an age-matched reference population [41] and can be calculated as follows:

$$T - score = \frac{\text{Measured BMD} - \text{Young adult mean BMD}}{\text{Young adult population SD}} \tag{2.3}$$

$$Z - score = \frac{\text{Measured BMD} - \text{Age matched mean BMD}}{\text{Age matched population SD}} \tag{2.4}$$

Based on the T score calculated over female population, four essential diagnostic categories have been established by the World Health Organization (WHO) and the International Osteoporosis Foundation (IOF) [42] to assess osteoporosis using DXA:

Despite being used in the clinical routine for the diagnosis of osteoporosis, DXA suffers from several limitations mainly in its two dimensional nature, because it provides

Table 2.1: The four diagnostic categories designed by WHO and IOF to assess Osteoporosis using T-score

Status	$T-score$
Normal	$\geqslant -1$
Low bone mass (Osteopenia)	$-2.5 < T-score < -1$
Osteoporosis	$\leqslant -2.5$
Severe Osteoporosis	< -2.5 with one or more fragility fracture in the past

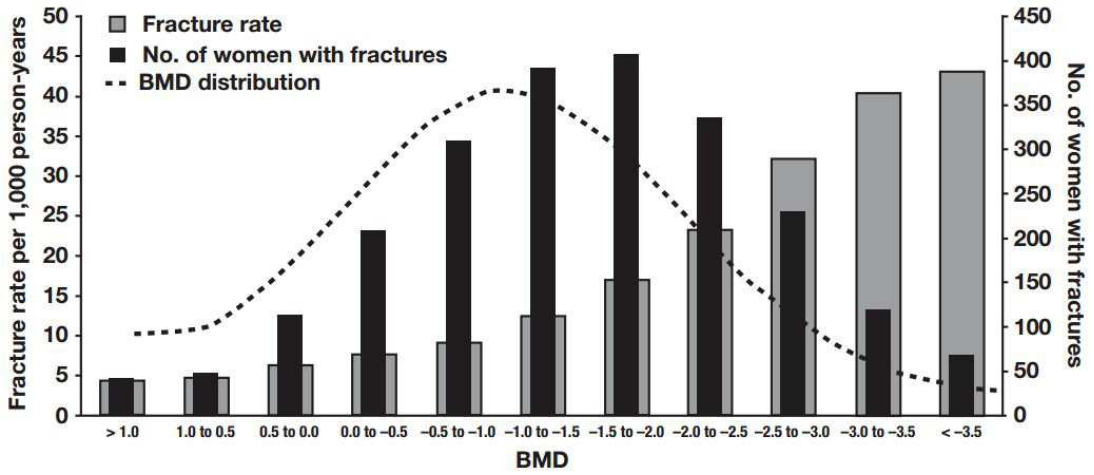

Figure 2.4: Fracture rate, BMD distribution, and number of fractured based on NORA [29].

a 2D projection of the 3D bone structure. Therefore, it cannot capture the 3D bone morphology nor its microarchitecture. Furthermore, different studies [29, 30] have illustrated that BMD cannot be used alone to predict osteoporotic fractures because less than 50% of the variation in the bone strength is attributable to variations in BMD [43].

For instance, The US National Osteoporosis Risk Assessment (NORA) study [29] revealed that 82% post-menopausal women with a fracture after one year of follow-up had a $T-score > -2.5$ and 67% had a $T-score > -2.0$ as illustrated in Figure 2.4. Similarly, in a Rotterdam cohort [30], 56% of the non-vertebral fractures in the women and 79% in the men were belonging to osteopenic individuals with a $-2.5 < T-score < -1$. This is mainly due to the fact that BMD does not represent many factors that influence bone strength, and a variety of non skeletal factors that contribute to fragility are not considered. Therefore, efforts have been made to formulate a new system to better predict fracture risk using different factors other than the BMD. A Fracture Risk Assessment tool (FRAX) was proposed in [44]. This tool takes in consideration different clinical factors illustrated in Table 2.2 to compute the 10-year risk of hip and other osteoporotic fractures.

The FRAX algorithm has been developed after studying population-based cohorts

Table 2.2: Clinical Risk Factors Considered in FRAX tool

Clinical Risk Factors	Description
Country of residence	Available in different states now
Age	Accepts ages between 40 and 90 years
Sex	Male/Female
Race	offered only in US
Weight, Height	Calculate Body Mass Index (BMI in kg/m2)
History of fragility fracture	Including radiographic evidence of vertebral compression fracture
Family history of osteoporosis	Hip fracture in mother or father
Current smoking	
Corticosteroid use	Exposed to $\geqslant$ 5 mg/day of prednisolone for $\geqslant$ 3 mo (or equivalent doses of other glucocorticoids)
Rheumatoid arthritis	Diagnosis confirmed by a health-care professional
Secondary osteoporosis	Type-I diabetes, osteogenesis imperfecta in adults, untreated long-standing hypothyroidism and hypogonadism or premature menopause, chronic malnutrition or malabsorption, and chronic liver disease
Alcohol intake	$>$ 3 units/day (a unit of alcohol is equivalent to a glass of beer [285 mL], an ounce [30 mL] of spirits, or a medium-sized glass of wine [120 mL])

from Europe, North America, Asia and Australia, integrating clinical risk factors, with or without BMD at the femoral neck, to produce finally a 10-year probability of hip and major osteoporotic fracture Figure 2.5.

However, several limitations need to be considered while using the FRAX tool [45], due to the fact that, the reported rates of major osteoporotic fractures at sites other than the hip may not be accurate [30]. This is because, all patients with hip fracture are admitted in hospitals and therefore recruited in the cohort. However, patients with a wrist or proximal humeral fracture are usually excluded and treated as outpatients. This leads to an underestimation of the fracture probability associated with these sites.

Furthermore, Other densitometric techniques have been described in the literature but haven't received the proper attention such as Quantitative CT which can unlike DXA produce volumetric(3D) measurement of the lumbar spine and the proximal femur. Moreover, cross-sectional studies have shown that BMD measured using quantitative CT for the spine can discriminate individuals with fragility fractures better than BMD measured using DXA [46, 47]. However, QCT still suffers from several drawbacks, including its higher radiation dose (0.06 – 2.9 mSv), the limited number of longitudinal scientific stud-

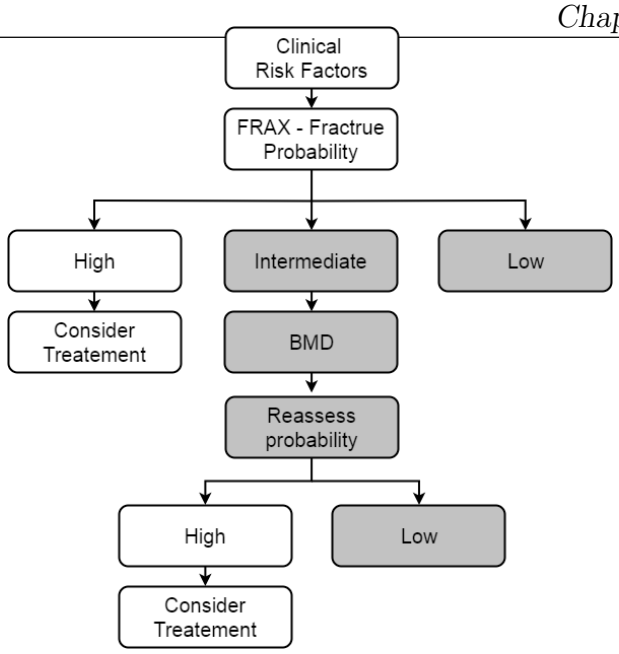

Figure 2.5: FRAX algorithm for the assessment of fracture probability

ies monitoring the role of QCT in predicting osteoporotic fractures, and more importantly, the QCT $T-scores$ are yet to be used in the definition of osteoporosis [27].

2.3 Qualitative bone assessment

One of the most important factors that motivated the assessment of the bone strength using its structure (quality) is because of the non-reliability of the BMD based techniques. As has been stated by the US National Osteoporosis Risk Assessment study [29] which revealed that only 18% of patients with a T score <-2.5 have fractures. This finding indicates that the bone strength is can be in fact explained using additional parameters to BMD to better determine the osteoporosis effect and the fracture risk.

The standard method to quantitatively describe the bone architecture is the estimation of morphometric indices, which was previously achieved using the histomorphometry parameters extracted from bone biopsies [48].

These parameters represent the morphological and topological characteristics of the trabecular bone such as the thickness of the trabeculae (Tb.Th), and their spacing (Tb.Sp : Trabecular separation) or the characteristics of the cortical bone such as the cortical thickness (Ct.Th), and the cortical porosity (Ct.Po) as they are further described in Table 2.3.

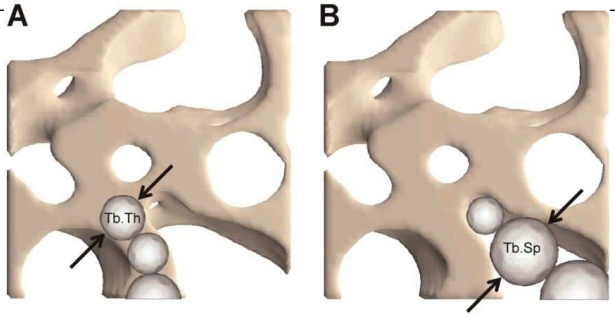

Figure 2.6: Sphere fitting technique for trabecular thickness and separation measurement

Table 2.3: Definition and description of bone morphology parameters

Abbreviation	Description	unit
TV	Total volume = Volume of the entire region of interest	mm^3
BV	Bone volume = Volume of the region segmented as bone	mm^3
BS	Bone surface = Surface of the region segmented as bone	mm^2
BV/TV	Bone volume fraction = Ratio of the segmented bone volume to the total volume of the region of interest	%
BS/TV	Bone surface density = Ratio of the segmented bone surface to the total volume of the region of interest	mm^2/mm^3
BS/BV	Specific bone surface = Ratio of the segmented bone surface to the segmented bone volume	mm^2/mm^3
Tb.N	Trabecular number = the average number of trabeculae per unit length	1/mm
Tb.Th	Trabecular thickness = Mean thickness of trabeculae, assessed using direct 3D methods	mm
Tb.Sp	Trabecular separation = Mean distance between trabeculae	mm
Tb.Th.SD	Standard deviation of trabecular thickness	mm
Tb.Sp.SD	Standard deviation of trabecular separation	mm
Ct.V	Cortical Volume	mm^3
Ct.Ar	Cortical bone area = cortical volume (Ct.V)÷(number of slices × slice thickness)	mm^2
Tt.Ar	Total cross-sectional area inside the periosteal envelope	mm
Ct.Th	Average cortical thickness	mm
Ct.Th.SD	Standard deviation of cortical thickness	mm
Ct.Po	Cortical porosity = the volume of pores (Po.V, mm^3) ÷ the volume of cortical bone (Ct.V, mm^3)	%
Po.N	Pores Number	n
Avg.Po.V	Average Pore Volume = Po.V ÷ Po.N	mm^3
Po.Dn	Pore density = Po.N ÷ Ct.V	

The calculation of these parameters should be based on 3D calculations. For Ct.Th, Tb.Th, Tb.Sp, and Tb.N a sphere-fitting technique, where for thickness measurement

spheres are fitted to the object and for separation the spheres are fitted to the background [49](Figure 2.6). Afterwards, the diameter of the largest possible sphere that can be fitted through each voxel is computed and then the average of these diameters is considered the mean thickness or separation. If the image resolution is sufficient like in the case of HRpQCT, further measurement can be computed for cortical bone such as cortical porosity (Ct.Po, as Po.V/Ct.V, %), total pore volume (Po.V, mm^3), pore number (Po.N, #), average pore volume (Po.V/ Po.N, mm^3), the standard deviation of the pore volume (Po.V.SD, mm^3), and pore density (Po.N/Ct.V, mm^3).

In the recent years, researchers were focused on the development and improvement of noninvasive high resolution imaging technologies such as: MRI and QCT to characterize bone structure using these parameters, which was previously achievable only using invasive bone biopsy [48].

2.3.1 High-resolution MRI

Magnetic resonance imaging (MRI) uses magnetic fields and radiation frequency rather than ionization used in CT and conventional radiography. In MRI, it is the combination of an intense magnetic field, gradients of magnetic fields in the three directions of space and radiofrequency pulses that generate images in three dimensions. The alignment of the magnetic moments of the protons of water as a result of the application of an intense magnetic field produces a resultant magnetization. However, high resolution MRI is limited by its relatively low signal-to-noise ratio compared to QCT. Moreover, *in vivo* MRI takes long acquisition times (12 mins), which makes it susceptible to motion artifacts. Furthermore, the spatial resolution with MRI is not in the range of trabecular dimensions (in-plane resolution, 0.15-0.3 mm2; section thickness, 0.3-1 mm), which results in false over/under estimation of the trabecular parameters.

The possibility of obtaining three dimensional images without the use of radiation makes this technique attractive for scientific and clinical studies. Furthermore, it provides the best current resolution with clinical routine devices [50]. However, this technique has been mainly established for peripheral imaging of the distal radius, tibia, and calcaneus.

A number of studies were performed that demonstrated that MRI can provide additional information to BMD for the differentiation between patients with and without fragility fractures [51, 52, 53]. A very limited number of longitudinal studies have shown

the possibility of monitoring the effect of treatments on bone formation [54]. However, the use of MRI remains confined to research because of its low availability and cost [55].

2.3.2 High Resolution peripheral Quantitative Computed Tomography (HRpQCT)

In the past twenty years, one of the most interesting developments to assess bone strength was the introduction of high resolution peripheral QCT scanners. This opened new perspectives in the exploration of the bone tissue. This imaging technology is based on a computerized processing of X-ray attenuation (measured in Hounsfield Units, HU) for the acquisition of sectional images, in the same way as a conventional CT scan does.

This relatively low radiation (<3 μSv) and non-invasive method provides a new in vivo information on the three-dimensional bone microarchitecture and volumetric BMD of the cortical and trabecular bones in the appendicular sites, commonly the radius and the tibia (Section 2.3.2) with a voxel size of 82 μm.

The scanner performing the HRpQCT images is currently dominated by one single manufacturer (XtremeCT, Scanco Medical AG, Brütisellen, Switzerland) [56].

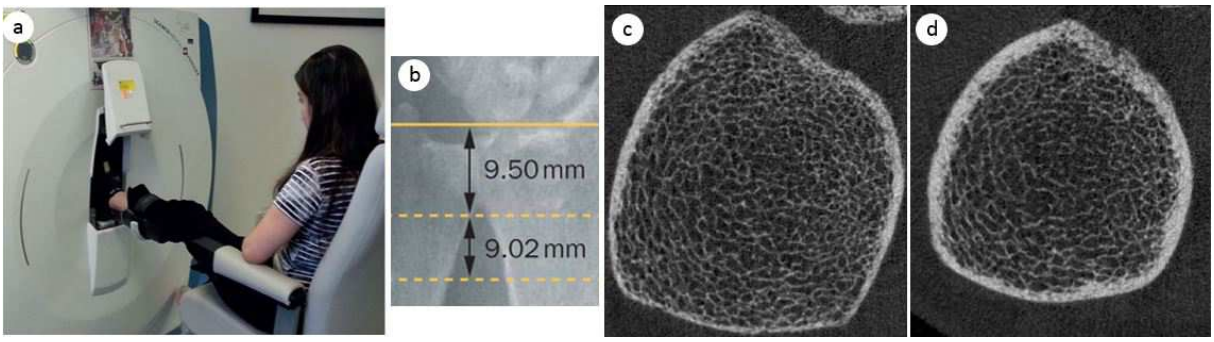

Figure 2.7: Tibia scan of a patient using Xtreme CT scanner (a), the scout view (b), and 2D ultra-distal scan of tibia (c) and distal scan (d)

The standard scanning procedure of HRpQCT starts by immobilizing the non dominant limb (hand or leg) of the patient in a carbon fiber shell to avoid artifacts resulting from motion. Initially, a 2D X-ray scan (referred as a scout view) is obtained to determine the precise region to be scanned as illustrated in Section 2.3.2b. On the Scout-View, a reference line has to be set. This reference line determines the position of the site to be scanned with a fixed offset from this line (in mm or %), depending on the control file settings (by default it is 9.50 mm for radius and 22.5 mm for tibia). Each site includes

110 slices, totaling an extension of 9.02 mm (110 × 0.082 mm) along the axial axis of the bone. The first slices close to the articulation are referred as ultra-distal slices (Section 2.3.2c) where the trabecular bone predominates and the cortical bone is thin. On the other hand, along the axial axis when the cortical bone is thickening up, these slices are referred as distal slices (Section 2.3.2d). The acquisition of this 3D images takes approximately 3 minutes using the default human peripheral *in vivo* scanning protocol : X-Ray tube current = 95 100 mA, X-Ray tube potential = 60 kVp, voxel size = 82 μm, and a 1536 × 1536 matrix.

What makes HRpQCT an interesting imaging technology is the clinical need for an imaging modality with lower radiation dose and better spatial resolution. The low dose radiation is related to the low radio-sensitivity of the targeted anatomical zones. However, by limiting itself to the peripheral regions, HRpQCT imaging excludes the analysis of the lumbar spine and the proximal regions of the tibia and therefore the main fracture sites [27].

Similarly to CT scanners, the HRpQCT imaging could be distorted by different artifacts such as ring, metal, or motion artifacts [57].

Ring artifact: Occasionally, this defect occurs when a mis-calibration or a failure of one or more detector elements in the scanner. This phenomenon creates an artifact that looks like rings or half rings around the isocentre (rotation center) of the reconstructed image and are usually visible on multiple slices at the same location. This artifacts can be resolved by a recalibration of the scanner.

Motion artifact: During scanning, the radiation source is rotating relative to the sample, to obtain different X-Ray projections from multiple angles. If the patient moves within the scanning rotation, the projections will not fit together properly during reconstruction, resulting in distortion of the object. For this reason, it is important that the patient stays immobilized during the scanning procedure so no motion artifact occurs.

Metal artifact: Scanning metals produce a star shaped artifacts in the reconstructed image, because they have a very high linear attenuation coefficients and absorb the X-ray beam totally. In our study, none of the recruited patients had a metal implant, therefore, the metal artifact didn't occur.

In addition to the morphometric parameters calculated from the binary segmenta-

tions of cortical and trabecular bones, the Xtreme CT scanner can estimate the volumetric BMD separately for cortical and trabecular bones. Furthermore, Finite Element Analysis (FEA) can be applied to these data sets and apparent bio-mechanical properties (eg: stiffness, elastic modulus) can be computed by decomposing the trabecular bone structure into small cubic elements (ie, the voxels) with assumed mechanical properties [58] (Figure 2.8).

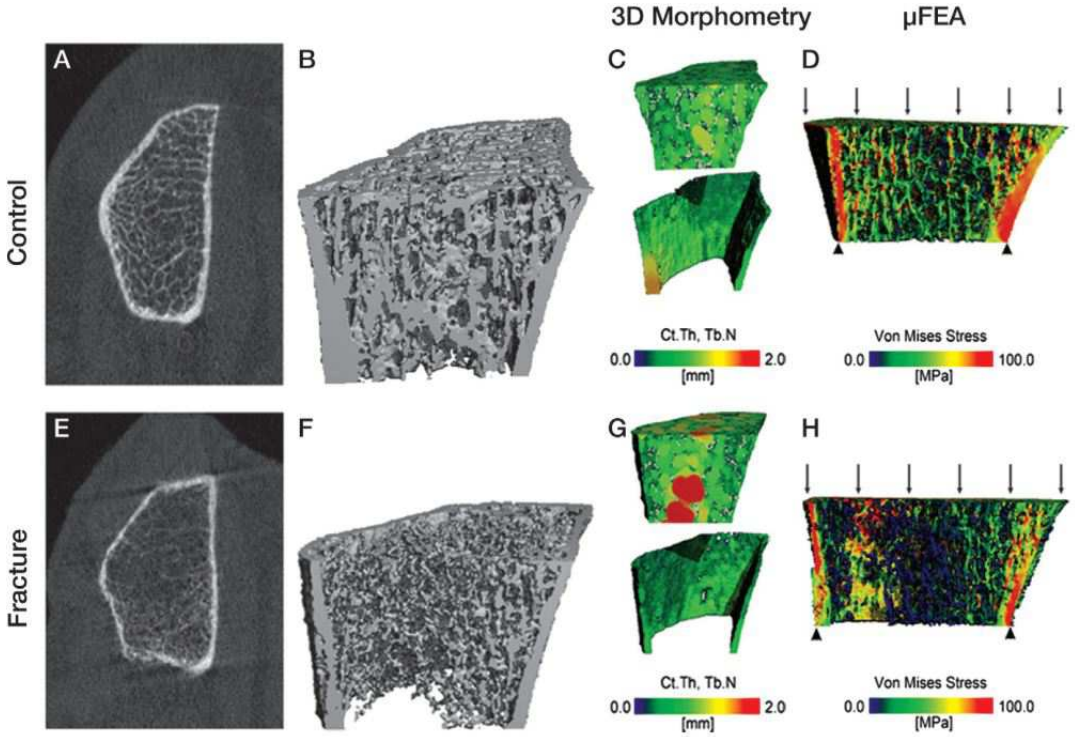

Figure 2.8: Different results extracted from the HRpQCT imaging studies to illustrate the bone quality differences between a healthy control subject (top) and a patient with hip fracture (bottom). (A, E) are The 2D tomograms and B, F, 3D surface renderings. C, G, represent the 3D morphometry of both bones. D, H, Finite Element Analysis data (Image courtesy of Andrew Burghardt [59].)

A very large number of clinical studies performed using HRpQCT data have demonstrated promising results in fracture risk assessment, predominantly in postmenopausal women with osteopenia and osteoporosis [60, 61, 62, 63]. In [64] the importance of structural parameters has been highlighted when they found that the bone structure contributes to fracture risk independently of areal BMD (aBMD). Another study [65] have examined the parameters BV/TV, Tb.N, Ct.Th, and Ct.BMD, and found that they were significantly different between those with wrist fracture compared with those with hip fracture. Stein *et. al* [66] also compared postmenopausal women with (n=68) and without (n=101) previous fracture and found that those with fracture had reduced volumetric BMD, more microarchitectural deterioration, and had lower estimated bone strength by

FEA. However, no measurement could adequately discriminate fracture types [66]. Therefore, different attempts have been conducted using different parameters and/or advanced statistical techniques to discriminate fractures types.

The combination of different parameters to discriminate fracture types have been initiated by [67, 68] using principal component analysis (PCA). Both studies highlighted the importance of the cortical bone (Ct.BMD, Ct.Th, and FE estimates) in determining bone strength, and discriminating wrist fractures cases [68] from other fractures [67]. A recent study has examined patients with type 2 diabetes and suggested that cortical porosity measurements are useful to assess increased fracture risk [59]. Unlike using DXA BMD which was increased in patients with type 2 diabetes. This is another reason to revoke the usage of DXA BMD and to prove that it is not well-suited for fracture risk diagnosis.

In addition to postemenaupausal women studies, differences in bone micro-architecture have been observed in men with and without fractures [69, 70]. These studies demonstrated that FE estimates and microarchitecture parameters are associated with all types of fractures. Furthermore, Graeff C *et. al* [70] showed the superiority of HRpQCT parameters on DXA in discriminating vertebral fractures in men with glucocorticoid-induced osteoporosis.

2.4 Conclusion

Along this advancement in image acquisition and quality, attention now is focused on the development of image analysis techniques to quantify the microarchitectural parameters of the bone. The first step in structural image analysis is the image segmentation, which is defined as the process of understanding the image by dividing it into meaningful structures (regions). In our case, it's the separation between the cortical and the trabecular bone in HRpQCT images, which is a very critical step to accurately generate reliable bone morphometry [57]. The following chapter provides an elaborate depiction of the image segmentation problem and the different state of the art techniques previously published with a special focus on active contours approaches.

Chapter 3

Image Segmentation using Active contours

3.1 Introduction

Image segmentation is the first step in structural imaSge analysis. It simplifies the understanding of the image and divides it into meaningful structures (regions) that share the same characteristics such as intensity level, color, or texture. The goal of the segmentation is, therefore, to partition the image domain into homogeneous regions corresponding to individual objects.

However, It is considered a challenging task to find a segmentation technique that works on several types of images. Since a method applied to one image may not reproduce the same result compared to another. Therefore, several segmentation techniques have been proposed throughout the years. These methods can be divided into two main categories: model-free (unsupervised) methods and knowledge-based (supervised) methods. Unsupervised techniques segment the image based on a certain similarity criterion aiming at grouping together pixels with consistent visual properties. On the other hand, supervised methods are based on training a classifier using predefined informations such as: shape, texture, etc, to seek a solution that is a compromise between the one produced from the training phase and the one expressed in the test phase. Due to its popularity and the number of publications, only the first type is discussed in this chapter.

Among the popular model-free techniques, we find thresholding techniques, where the intensities of the image pixels are compared to a certain threshold defined automatically

or by the operator[71, 72, 73]. Clustering techniques which group the image pixels into clusters based on their shared characteristics, so the difference between these pixels is minimal [74, 75, 76, 77, 78, 79]. Graph based methods including normalized cuts[80], graph-cuts [81]. Watershed segmentation [82, 83], and variational methods including Mumford-shah technique [84] and its active contours variants [85, 86].

In the remainder of this chapter, we will focus on the Active Contours Models (ACM) and review the different variant approaches proposed based on it. The goal of this chapter is to provide first a theoretical background of the active contours approach, and then the different formulations proposed based on it (Figure 3.1).

3.2 Active contours

Since they were first introduced by Kass *et al.* [87], ACM have received more attention and have been extensively used in medical image segmentation. The idea is to evolve a curve in the image domain using two forces, one computed from the image data, often called external force, which pulls the contour towards the features of interest and another one referred as internal force to ensure the smoothness of the contour during evolution.

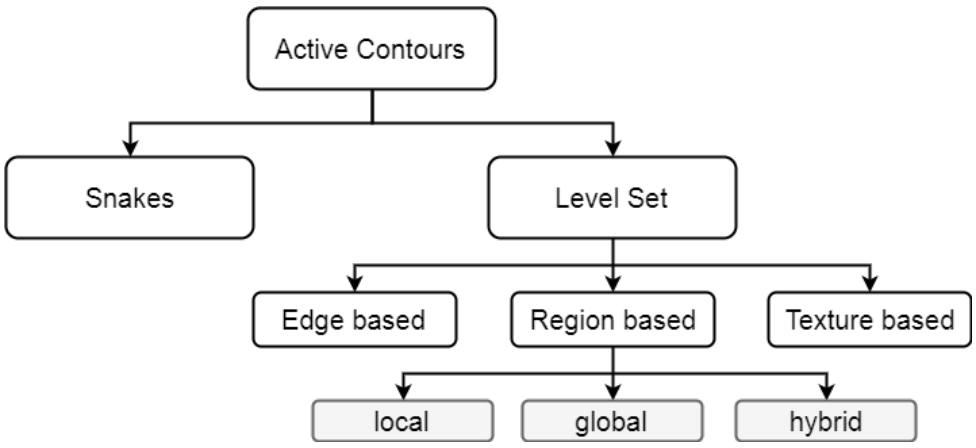

Figure 3.1: Active Contours Models

As illustrated in Figure 3.1, ACM are categorized based on how they defined (snakes or level set) further explanation of each representation is in the following section. Level set based ACM have received more attention in the recent years, and according to the external force, there are two kinds of ACM: edge and region-based. Edge based ACM use the information of the objects boundaries usually the gradient. Region based ACM use the statistical information of image intensity within each region. However, classical ACM cannot handle intensity inhomogeneity and noise level in medical images, therefore,

several variants of active contours have been proposed such as: local based ACM, Fuzzy ACM, Texture based ACM, etc (Figure 3.1).

3.2.1 Snakes

The first model of active contour was proposed by Kass *et al.* [87] and named snakes due to the appearance of the contour's evolution. The contour C can be defined as follows:

$$C(s) = (x(s), y(s)) : 0 \leqslant s \leqslant L : \Re \longrightarrow \Omega \tag{3.1}$$

where L denotes the length of the contour C, and Ω denotes the entire domain of an image $I(x, y)$. An energy function $E(C)$ can then be defined such as:

$$E(C) = E_{int} + E_{ext} \tag{3.2}$$

where E_{int} and E_{ext} respectively represent the internal energy and external energy functions. The internal energy function determines the regularity, *i.e.* the smooth shape, of the contour. A common choice for the internal energy is a functional given by :

$$E_{int} = \int_0^L \alpha|C'(s)| + \beta|C''(s)|^2 ds \tag{3.3}$$

Here α controls the tension of the contour, and β controls the rigidity of the contour. As for the external energy term which represents the criteria of contour evolution which depends on the image, it is defined as follows :

$$E_{ext} = \int_0^L \frac{1}{\lambda|\Delta G_\sigma * I(x, y)|} \tag{3.4}$$

where G_σ is a Gaussian smoothing filter with the standard deviation σ, and λ is a suitably chosen constant. Solving the problem of snakes is to find the contour that minimizes the total energy term with the given set of weights α, β, and λ.

The classic snakes provide an accurate segmentation only if the initial contour is given sufficiently near the edges of the object of interest because they make use of only the local information along the contour. Estimating a proper position of initial contours without prior knowledge is a difficult problem. In addition, classic snakes cannot detect more than one boundary simultaneously because the snakes maintain the same topology during the

evolution stage. This means, snakes cannot split to multiple boundaries or merge from multiple initial contours [88]. And then, it comes the level set theory proposed by [89] to solve this problem.

In this thesis, we are interested only on the level set based active contours methods because of their popularity, their performance, and their abundance among published papers.

3.2.2 Level Set

Level set theory is a formulation to implement active contours that was proposed by Osher and Sethian [89]. They represented a contour implicitly via a two-dimensional Lipschitz-continuous function $\phi : \Omega \rightarrow \Re$ defined on the image plane. The function $\phi(x, y)$ is called level set function, and a particular level, usually the zero level of $\phi(x, y)$ is defined as the contour, such as:

$$C = \{(x, y) : \phi(x, y) = 0\}, \forall (x, y) \in \Omega, \tag{3.5}$$

where Ω denotes the entire image plane. With this definition, the evolution of the contour is equivalent to the evolution of the level set function, i.e. $\partial C/\partial t = \partial \phi(x, y)/\partial t$. The advantage of using the zero level is that a contour can be defined as the border between a positive area and a negative one, so the contours can be identified by just checking the sign of $\phi(x, y)$.

The initial level set function $\phi_0(x, y)$ may be given by the signed distance from the initial contour such as,

$$\begin{aligned} \phi_0(x, y) &= \phi(x, y) : t = 0 \\ &= \pm D((x, y), N_{x,y}(C_0)), \forall (x, y) \in \Omega \end{aligned} \tag{3.6}$$

where $\pm D(x, y)$ denotes a signed distance between x and y, and $N_{x,y}(C_0)$ denotes the nearest neighbor pixel to the initial contours $C_0 = C(t = 0)$ from (x, y).

The deformation of the contour is generally represented in a numerical form as a Partial Differential Equation(PDE). A formulation of the contour evolution using the magnitude of the gradient of $\phi(x, y)$ was initially proposed by Osher and Sethian [90, 91],

as :

$$\frac{\delta\phi(x,y)}{\delta t} = |\nabla\phi(x,y)|(v + \epsilon\kappa(\phi(x,y))) \tag{3.7}$$

where v denotes a constant speed term to push or pull the contour, $\kappa(.) : \Omega \to \Re$ denotes the mean curvature of the level set function $\phi(x,y)$ given by:

$$\kappa(\phi(x,y)) = div(\frac{\nabla\phi}{||\nabla\phi||}) \tag{3.8}$$

The role of the curvature term is to control the regularity of the contour as the internal energy term does in the classic snakes model. ϵ controls the balance between the regularity and robustness of the contour evolution.

Another form of contour evolution was proposed by Chan and Vese [92,]. The contour length $|C|$ can be approximated by a function of $\phi(x,y)$, such as:

$$\begin{aligned} |C| &= \int_\Omega |\nabla H(\phi(x,y))| dxdy \\ &= \int_\Omega \delta(\phi(x,y))|\nabla\phi(x,y)| dxdy \end{aligned} \tag{3.9}$$

where, $H(.)$ denotes the regularized form of the Heaviside function and $\delta(.)$ its derivative.

The contour evolution is therefore defined:

$$\frac{\partial\phi(x,y)}{\partial t} = \delta(\phi(x,y))\kappa(\phi(x,y)), \tag{3.10}$$

3.3 Methods

3.3.1 Edge-based Active Contours

Geometric active contour

The Geometric ACM was proposed by Caselles *et al.* [93] by adding an additional term, called stopping function, to the speed function. It was the first level set implemented ACM for the image segmentation problem. Malladi *et al.* [91, 94] proposed a similar model:

$$\frac{\partial\phi(x,y)}{\partial t} = g(I(x,y))|\nabla\phi(x,y)|(v + \kappa(\phi(x,y))) \tag{3.11}$$

where $g(.) : \Omega \rightarrow \Re$ denotes the stopping function, i.e. a positive and decreasing function of the image gradient. A simple example of the stopping function is:

$$g(I(x,y)) = \frac{1}{1 + |\nabla I(x,y)|^n} \tag{3.12}$$

where n is given as 1 in [93] and 2 in [91].The contours move in the normal direction with a speed of $g(I(x,y))(\kappa(\phi(x,y)) + v)$, and therefore stops on the edges, where $g(.)$ vanishes. The curvature term $\kappa(.)$ maintains the regularity of the contours, while the constant term v accelerates and keeps the contour evolution by minimizing the enclosed area [95].

Geodesic active contour

The Geodesic ACM was proposed by Caselles *et al.* [96, 97]. Kichenassamy *et al.* [98] and Yezzi *et al.* [92] also proposed a similar active contour model. Based on the principle of the classic dynamic systems, solving the active contour problem is equivalent to finding a path of minimal distance, called geodesic curve [99] given by:

$$\frac{\partial C}{\partial t} = (g(I(x,y))\kappa(\phi(x,y)) - \nabla g(I(x,y)).N)N, \tag{3.13}$$

where N denotes the inward unit normal. From the relation between a contour and a level set function and the level set formulation of the steepest descent method, solving this geodesic problem is equivalent to searching for the steady state of the level set evolution equation [96] and can be expressed as follows:

$$\frac{\sigma\phi(x,y)}{\sigma t} = g(I(x,y))|\nabla\phi(x,y)|(v + \kappa(\phi(x,y))) + \nabla g(I(x,y)).\nabla\phi(x,y) \tag{3.14}$$

where v is an additional speed term to accelerate the evolution. The equivalence between classic snakes and geodesic active contours has been also shown by other authors [100, 101, 102, 103] in slightly different views. It is evident that the geodesic active contour model is identical to the geometric active contour model except for the added term $\nabla g(I(x,y)).\nabla\phi(x,y)$

More recently, Pratondo *et al.* [104] proposed a robust edge stopping function for the geodesic active contours to solve the problem of poorly defined boundaries in medical images. The basic idea is, in addition to gradient stopping function they use a machine

learning method to construct a probability score of each pixel to be classified as a foreground. The chance that a boundary exists is high when an ambiguous classification occurs, i.e., the probability score is 0.5. Based on this definition a fuzzy edge stopping function was defined as follows:

$$p(s) = (2(s - 0.5))^2 \tag{3.15}$$

Where s is the probability score for the foreground. However, this technique is considered a supervised active contours approach [104] that depends on the training classifier probability results. Due to the structure of the speed functions and the stopping functions defined above, edge based active contour models have a few disadvantages. Because of the constant term v, edge based active contour models evolve the contour towards only one direction, either inside or outside. Therefore, an initial contour should be placed completely inside or outside the ROI (region of interest), and some level of a prior knowledge is still required. Since edge-based active contours rely on the image gradient operation, this type of active contours may skip the blurry boundaries, and they are sensitive to local minima or noise as edge-based segmentation does.

3.3.2 Region-based Active Contours

Among the different formulations of active contours, region based ACM is the most popular, because it does not depend on the phase of initialization unlike edge based methods. Most region-based active contour models consist of two parts: the regularity part, which determines the smooth shape of the contours, and the energy minimization part, which searches for the uniformity of the desired feature within a subset. A nice characteristic of global region-based ACM is that the initial contours can be located anywhere in the image as region-based segmentation relies on the global energy minimization rather than local energy minimization. Therefore, less prior knowledge is required than edge-based ACM. Figure 3.2 illustrates the segmentation result of edge based technique [97] against region based one [85].

Piecewise-constant active contour

Piecewise-constant ACM was proposed by Chan and Vese [105, 106] using the Mumford-Shah segmentation model [107, 84]. Piecewise-constant ACM moves deformable contours

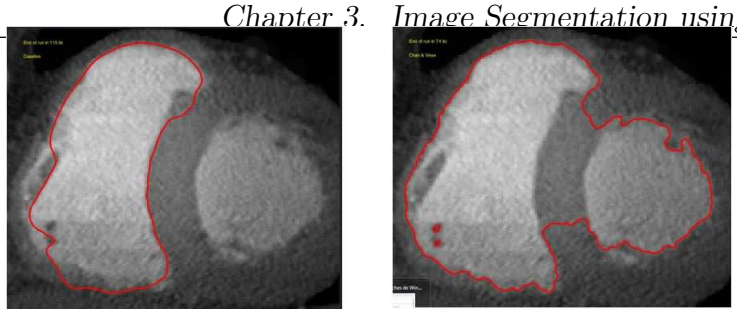

Figure 3.2: Segmentation result of edge based technique (geodesic active contours [97]) left and region based (active contours without edges [85]) right

minimizing an energy function instead of searching for edges. A constant approximates the statistical information of image intensity within a subset, and a set of constants, i.e. a piecewise-constant, approximate the statistics of image intensity along the entire domain of an image. The energy function measures the difference between the piecewise-constant and the actual image intensity at every image pixel. The level set evolution equation is given by:

$$\frac{\sigma\phi(x,y)}{\sigma t} = \delta_\epsilon(\phi(x,y))[v\kappa(\phi(x,y)) - (I(x,y)-\mu_1)^2 - (I(x,y)-\mu_2)^2] \tag{3.16}$$

where μ_0 and μ_1 respectively denote the mean of the image intensity within the two regions (outside and inside the contours).

Piecewise-smooth active contour

An extension of piecewise-constant ACM using a set of smoothed partial images, was also proposed by Chan and Vese [108, 108, 109, 110, 111]. The same segmentation energy employed in the piecewise-constant model to partition an image is used. But in this model each subset is also represented by its smoothed representation. The level set evolution equation is given by:

$$\begin{aligned}\frac{\sigma\phi(x,y)}{\sigma t} = \delta_\epsilon(\phi(x,y))[v\kappa(\phi(x,y)) - (I(x,y)-\mu_1)^2 - (I(x,y)-\mu_2)^2 \\ - \omega(|\nabla\mu_1(x,y)|^2 - |\nabla\mu_0(x,y)|^2)]\end{aligned} \tag{3.17}$$

where $\mu_0(x,y)$ and $\mu_1(x,y)$ denote the smoothed images within the outside and inside of contours. However, traditional region-based models rely on the idea that the intensity of images is homogeneous. Because the contours evolve under the assumption that the image consists of two distinct homogeneous regions. This means that the outside and inside contour regions have different mean pixel intensity, which is not the case in images

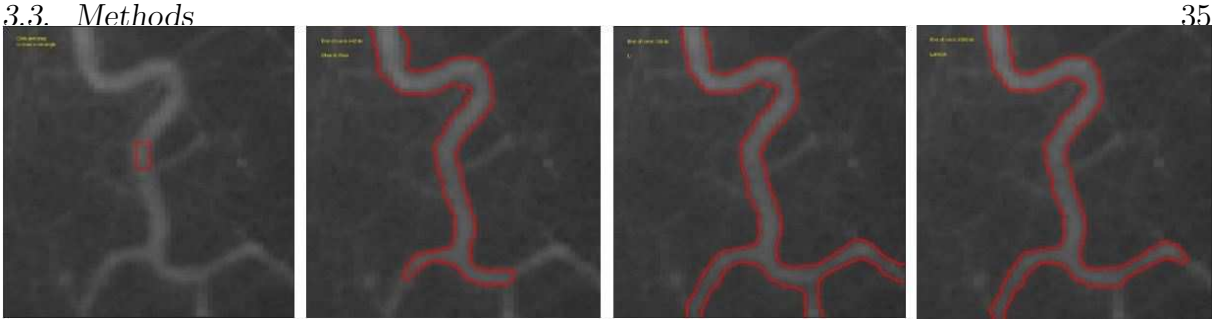

Figure 3.3: Segmentation result of local based active contours against global. (a) the initialization of the contours, (b), (c), and (d) are the segmentation results of the Chan veze [85], Chunming [112] and Lankton [113] respectively

with intensity inhomogeneity such as medical images MRI, PET, CT, etc. In what follows, only the fitting energy of each method will be expressed, because the regularity term is the same for all the methods, using either the curvature $\kappa(.)$ or the length of the contour $|C|$.

Due to global region based active contours problem with intensity inhomogeneity, as illustrated in (Figure 3.3), Chan Veze [85] wasn't able to segment properly the vessel image, unlike Chunming [112] and Lankton [113] who uses a local region based ACM [114, 115, 116, 117, 118, 119, 62] that will be detailed next.

3.3.3 Local Region Based Active Contours

In [115, 116], Chunming Li *et al.* proposed an efficient region-based ACM to segment inhomogeneous images using the intensity information of the local regions at a controllable scale. A data fitting energy is defined using functions that locally approximate the image intensities on the two sides of the contour. The proposed method by [116] segments inhomogeneous images by employing a local binary fitting (LBF) energy with a kernel function. The energy function is expressed as follows:

$$E = \sum_{i=1}^{2} \lambda_i \int_{\Omega_i} K(x-y)|I(y) - \mu_i(x)|^2 dy \tag{3.18}$$

where, λ_1 and λ_2 are positive constants, and $\mu_1(x)$ and $\mu_2(x)$ are two values that approximate the image intensities in $\Omega_1(insideC)$ and $\Omega_2(outsideC)$, respectively. The intensity pixels $I(y)$ represent the local region centered at the point x, whose size can be controlled using the kernel function. In [116] the choice of the kernel is Gaussian, defined as follows:

$$K_\sigma(u) = \frac{1}{(2\pi)^{n/2}\gamma^n} e^{-|u|^2/2\gamma^2} \tag{3.19}$$

with a scale parameter $\gamma > 0$.

A different formulation of this technique was proposed by C. He *et al.* [119] where they replaced the Gaussian kernel with a "mollifying" kernel with compact support and added a weight to the energy function. The added weight function is defined by a local entropy derived from a gray level distribution of the image [120]. The proposed energy functional is defined as follows:

$$E = \sum_{i=1}^{2} \lambda_i \int_{\Omega} E_x(X)(\int_{\Omega_i} K_p(x-y)|I(y) - \mu_i(x)|^2 dy)dx \tag{3.20}$$

where, $E_x(X) = E(x, B(x,r))$ is the local entropy of $x \in \Omega$,
$B(x,r) = y : |x-y| \leq r, r > 0$, the kernel K_p is chosen as a mollifying kernel of the form:

$$K_p(u) = \frac{1}{p^2}\psi(\frac{u}{p}), u \in \Re^2 \tag{3.21}$$

where $p > 0$ is a scale parameter and the function $\psi(u)$ is a symmetric mollifier defined as follows:

$$\psi(u) = \begin{cases} Ae^{\frac{-1}{(1-|u|^2)}}, & \text{if } |u| \leq 1 \\ 0, & \text{if } |u| > 1 \end{cases} \tag{3.22}$$

where the constant $A > 0$ is selected so that $\int_{\Re^2} \psi(u)du = 1$.

Another, localized energy based ACM was proposed by Lankton *et al.* [117] to localize any region-based energy in a fully variational way. The analysis of local regions leads to the construction of a family of local energies at each point along the curve. In order to optimize these local energies, each point along the curve is considered separately, and moves to minimize the energy computed in its own local region using a ball. To compute these local energies, the local neighborhoods of each point x are split into local interior and local exterior by the evolving curve. The energy optimization is then obtained by fitting a model to each local region, and therefore, it can be defined as follows:

$$E(\phi) = \int_{\Omega_x} \delta\phi(x) \int_{\Omega_y} B(x,r).F(I(y), \phi(y))dydx \tag{3.23}$$

where, B is a ball function used as a mask to extract the local region of each point x. F is a generic internal energy function representing the local adherence to a given model at each point along the contour. Different region based energy functions F were employed such

as: uniform modeling energy [106], mean separation [121], and the histogram separation (HS) energy using the Bhattacharyya coefficient [122, 123].

3.3.4 Hybrid Active Contours

The first integration of global and local information was the integration of edge and region based information that has been proposed by a several authors. Geodesic active region is a supervised ACM, proposed by Paragios [124, 125], incorporating both edge and region-based energy in the same function. A statistical analysis based on the Minimum Description Length (MDL) criterion and the Maximum Likelihood (ML) principle for the observed density function, for example: an image histogram, which indicates the number of sub-regions and the statistical Probability Density Function (PDF) within those sub-regions using a mixture of Gaussian elements. Regional probability is estimated from the statistical PDF based on prior knowledge, i.e. training samples. Then, the boundary information is determined by a probabilistic edge detector, estimated from the regional probabilities of neighborhood [126]. For example, an image pixel is more likely an edge pixel if the neighborhood pixels, located on the opposite sides, have high regional probabilities for a different class. The level set evolution equation is given by

$$\frac{\delta\phi(x,y)}{\delta t} = |\nabla\phi(x,y)| * [\alpha \sum_{b} w_b log(\frac{p_1(I_b(x,y))}{p_2(I_b(x,y))}) + (1 - \alpha g(p_e(x,y))\kappa(\phi(x,y)) + \nabla g(p_e(x,y)).\frac{\nabla\phi(x,y)}{|\phi(x,y)|})] \tag{3.24}$$

where $I_b(x,y)$ denotes the $b-th$ band of a multispectral image "$I(x,y)$". $p_i(I_b(x,y))$ denotes the regional probability presenting for a pixel $I_b(x,y)$ to belong to a sub-region i, $p_e(x,y)$ denotes the probabilistic edge detector so that a boundary pixel is located at (x,y), and $g(p_e)$ denotes a positive and decreasing function of the probability. Jehan-Besson *et al.* also proposed an ACM [127, 128] minimizing an energy criterion involving both region and boundary functional. These functionals are derived through a shape derivative approach instead of classical calculus of variation. They focus on the statistical property, i.e. the PDF of the color histogram of a sub-region. Many hybrid approaches have been proposed all over the years [129, 130, 131, 132, 133], they all use use two functional energy one based on global, and the other based on local information.

3.3.5 Texture-based Active Contours

Despite the high accuracy of edge, and region based ACM on image segmentation, they are not very efficient on outdoor object detection and segmentation. This is because outside scenery is composed of different patterns (textures). Therefore, different ACM variants have been proposed based on image texture.

Structure tensor featrues

The proposed approach [134] extracts the classical structure tensor texture parameters [135, 136, 137] using the following formula:

$$J_p = K_p * (\nabla I \nabla I^T) = \begin{pmatrix} K_p * I_x^2 & K_p * I_x I_y \\ K_p * I_x I_y & K_p * I_y^2 \end{pmatrix} \tag{3.25}$$

where, K_p is a Gaussian kernel and p is its standard deviation. Instead of using the original image I in the ACM energy minimization problem, a vector valued image $u = (u1, u2, u3, u4)$ obtained by smoothing $(I, I_x^2, I_y^2, I_{xy})$ is used in the fitting energy function. Moreover, the image segmentation in [134] was formulated as maximizing the a posteriori partitioning probability $p(G(\Omega)|I)$ where $G(\Omega) = \{\Omega_1, \Omega_2\}$ is a partition of the image domain. Let $p_1(u(x))$ and $p_2(u(x))$ be the probability density functions for the value $u(x)$ to be in Ω_1 (inside contour) and Ω_2 (outside contour), respectively. The image segmentation using the structure tensor parameters can be found by minimizing the following energy:

$$E = -\int_{\Omega_1} logp_1(u(x))dx - \int_{\Omega_2} logp_2(u(x))dx \tag{3.26}$$

Gabor features

Sagiv et. al. [138] proposed a texture based active contours using the Gabor feature space [139] and the 2D Riemannian manifold of local features [140] for both edge based, and region based active contours. For edge active contours, based on the 2-D submanifold of texture features, and using the natural Riemannian metric defined on it, a novel edge stopping function was defined as follows:

$$E(texture(x, y)) = \frac{1}{det(g_{\mu v})} \tag{3.27}$$

where, $g_{\mu v}$ is the Gaussian smoothed derivatives of the image used as a metric for the Gaussian-Beltrami flow. For the region based active contours, they used the vector valued active contours [85] and the Gabor transforms obtained when convolving Gabor filters with the image. Let u_0 be the textured image, and $u_0^i, (i = 1, \ldots, N)$, be N Gabor transforms of the original image. The fitting energy term is then defined as follows:

$$E = \int_{\Omega_1} 1/N \sum_{i=1}^{N} \lambda_+^i |u_0^i(x,y) - c_+^i| - \int_{\Omega_2} 1/N \sum_{i=1}^{N} \lambda_-^i |u_0^i(x,y) - c_-^i| \tag{3.28}$$

where, λ_-^i and $\lambda_+^i > 0$ are fixed parameters for each Gabor channel, c_+^i, c_-^i are the averages of each Gabor channel in Ω_1 and Ω_2, respectively.

LBP features

Another interesting texture based active contours technique is based on the LBP features [141]. It utilizes the vectors $D_i(x,y)$, $i = 1, 2, ..., b$, where each component $D_i(x,y)$ corresponds to the ith bin of the LBP distribution, and $b = 2^P$ is the number of bins comprising each distribution. $D_i(x,y)$ encodes the textural properties of $k \times k$-pixel image regions centered at pixel (x,y). Moreover, the log-likelihood statistic was suggested by [141] as an accurate similarity measure for LBP distributions. Therefore, the fitting energy term is now defined as follows:

$$E = \int_{\Omega_1} 1/b \sum_{i=1}^{b} \lambda_+^i (1 - D^i(x,y) log(c_+^i)) - \int_{\Omega_2} \lambda_-^i (1 - D^i(x,y) log(c_-^i)) \tag{3.29}$$

Similarly using the vector based active contours, different techniques were developed based on Principal Component Analysis (PCA) [142, 143], the fractal dimension feature [144], the Bhattacharyya Gradient Flow [123], and the intensity covariance matrices [145].

3.3.6 Fuzzy Active Contours

Another interesting variant was proposed using the inclusion of the fuzzy logic in the region based ACM energy [85].

Fuzzy region based active contours

Krinidis and Chatzis [146] proposed the usage of the fuzzy clustering logic in the active contours model as an external force to pull the curve towards more robust and

noise resistant clusters. The authors [146] demonstrated its capability of handling the noise of the image as well as the boundaries discontinuity. The Fuzzy Energy Based Active Contours (FEBAC) model proposed by Krinidis and Chatzis [146] defined a new pseudo level set formulation using the fuzzy membership function $u \in [0, 1]$, defined as follows:

$$\begin{aligned} C =& (x, y) \in I : u(x, y) = 0.5, \\ inside(C) =& (x, y) \in I : u(x, y) > 0.5, \\ outside(C) =& (x, y) \in I : u(x, y) < 0.5 \end{aligned} \tag{3.30}$$

The energy function is therefore reformulated:

$$E = \lambda_1 \int_\Omega [u(x, y)]^m |I(x, y) - \mu_1| dxdy + \lambda_2 \int_\Omega [1 - u(x, y)]^m |I(x, y) - \mu_2| dxdy \tag{3.31}$$

where μ_1 and μ_2 are the average constants of the regions inside and outside the contour, respectively. They can be calculated as follows:

$$\mu_1 = \frac{\int_\Omega [u(x, y)]^m I(x, y)\, dx}{\int_\Omega [u(x, y)]^m\, dx}, \mu_2 = \frac{\int_\Omega [1 - u(x, y)]^m I(x, y)\, dx}{\int_\Omega [1 - u(x, y)]^m\, dx}, \tag{3.32}$$

The membership function $u(x, y) \in [0, 1]$ is the degree of membership of $I(x, y)$ to the inside of C, and m is a weighting exponent on each fuzzy membership, defined as follow:

$$u(x, y) = \frac{1}{1 + (\frac{\lambda_1 (I(x,y) - \mu_1)^2}{\lambda_2 (I(x,y) - \mu_2)^2})^{(1/m-1)}} \tag{3.33}$$

The segmentation result can be obtained finally after energy minimization by checking if $u(x, y) > 0.5$.

Global and local fuzzy energy active contours

A different hybrid representation of this approach was proposed by Kuo-Kai *et al.* in [149, 150] and Thieu *et al.* in [130, 148].The proposed approach of [149] takes into consideration both global and local region statistical information. They both added the local information of each pixel to the fitting term of each region. In this case, there will be a global function to assure the convergence of the contour and a local function to capture

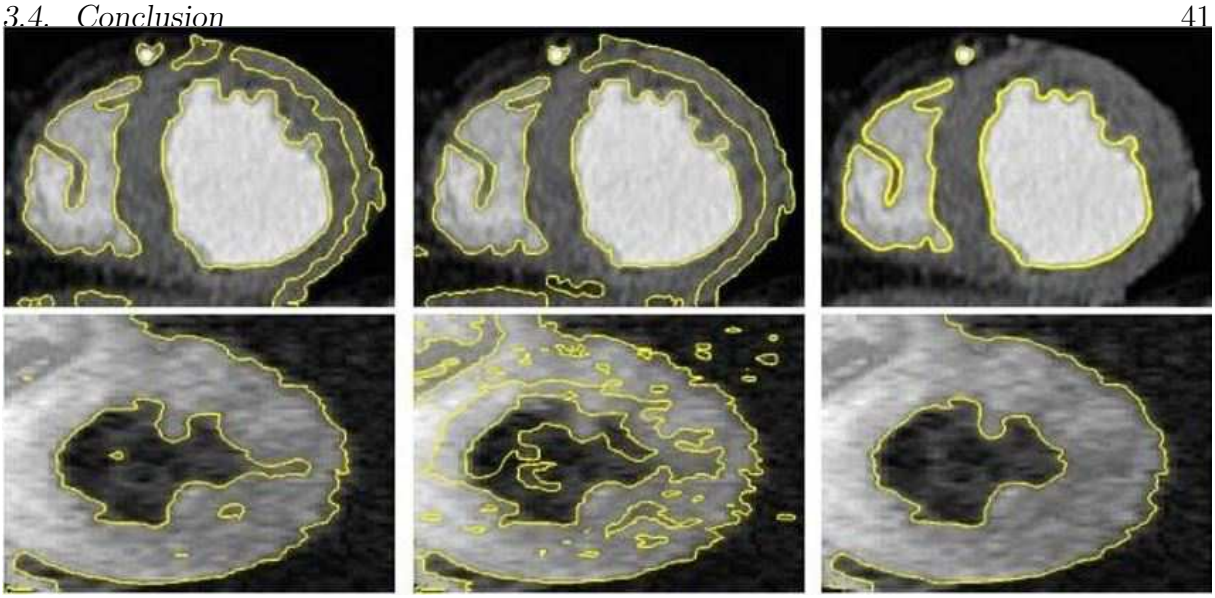

Figure 3.4: The segmentation result of the local [112], hybrid [147] and fuzzy hybrid [148] techniques on two heart MR images respectively. Source [148]

the inhomogeneity of each region.

$$\begin{aligned} E =& \beta \sum_{i=1}^{2} \int_{\Omega} \lambda_i (v_i(x))^m |I(x) - c_i|^2 dx + \\ & (1-\beta) \sum_{i=1}^{2} \lambda_i \int_{\Omega} (\int [v_i(y)]^m G_\sigma(x-y) |I(y) - f_i(x)|^2 dy) dx \end{aligned} \tag{3.34}$$

where the first term is the global term and the second is the local one. $v_1 = u$, $v_2 = 1 - u$, $f1(x)$ and $f_2(x)$ are two local functions used to approximate the intensity means of two local regions around the point x inside and outside the contour, respectively. β is a weight parameter, and G_σ is a Gaussian kernel.

3.4 Conclusion

Active contours models are considered one of the popular approaches for a variety of applications, particularly in medical image segmentation. They are based upon the utilization of deformable contours, which can move accordingly to internal forces and external forces derived from the image characteristics. In this chapter, a detailed overview was provided of different existing methods of active contours with particular focus on level set ACM. These various techniques are categorized in two groups based on the external force extracted from the image (Edge and region based). The latter group has received a tremendous amount of attention in medical image processing. Different modifications have been proposed all over the years, including localized energy, fuzzy logic integration,

texture information, etc. In the following chapter, we position the segmentation problem in the case of HRpQCT images, starting with the state of the art techniques, the patients database included in this study, and finally the quantitative metrics used for evaluating the different approaches.

Chapter 4

HRpQCT Image segmentation

4.1 Introduction

This chapter provides an overview of the different state of art techniques developed along the years to segment HRpQCT images. Then, a detailed presentation of the database of patients used for the segmentation and the prediction of osteoporotic fractures is provided. Finally, to validate the performance of the proposed approaches, three quantitative metrics are discussed.

4.2 State of art methods

4.2.1 Dual threshold

As the name of this approach [151] implies, it requires two threshold inputs, one to extract the periosteal and another to extract the endosteal surfaces of the output mask. Buie *et. al* proposed an algorithm of two steps where first the periosteal surface of the cortex is identified, and then the endosteal surface. In the first step, the image is binarized using the first threshold, then a median filter is applied to reduce the noise artifacts. 3D dilation and erosion operations (15 voxels, equivalent to 2.46mm), coupled with the connectivity filter are then used to close the marrow cavities in the trabecular bone. This ends the first step, which after closing the trabecular bone will result in the periosteal (outer) surface of the bone.

In the second step the original image is then re-thresholded using the second threshold, and masked with output of the first step, leaving only the marrow cavities. Dilation

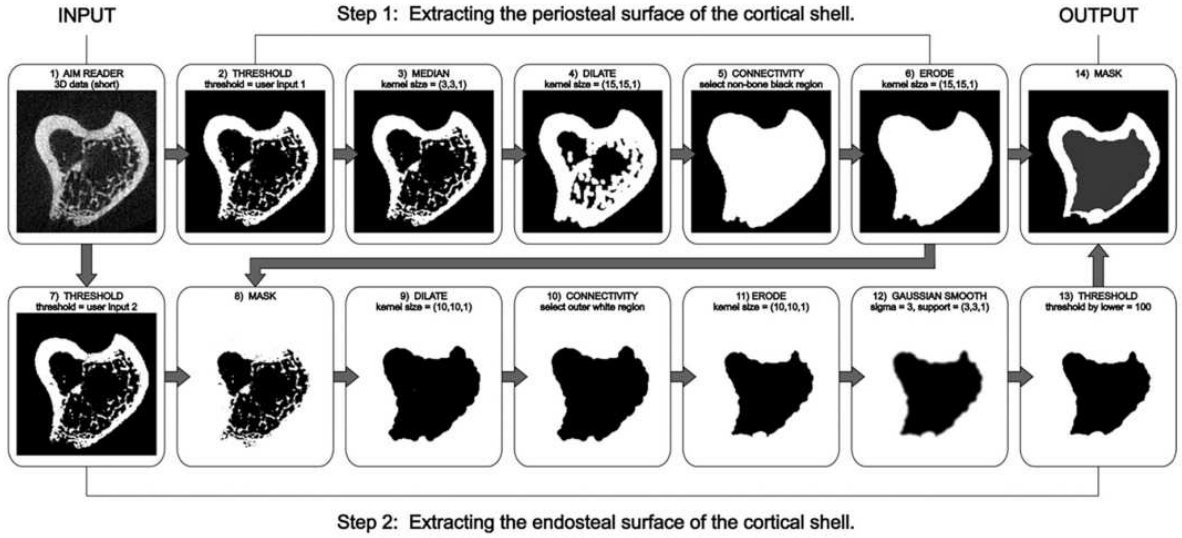

Figure 4.1: Summary of the two steps to extract the cortical bone in the Dual threshold techniques. Source [151]

.

and erosion operations are then used to reconnect the marrow cavities, thus eliminating trabeculae, allowing extraction of a trabecular region mask via a connectivity filter. The region is Gaussian smoothed and thresholded to reduce roughness of the endosteal surface. The cortical bone mask is then extracted through a simple combination of the output of the two steps (Figure 4.1).

4.2.2 Burghardt technique

An update of the Dual threshold approach was proposed by Burghardt *et al.* [152]. It is currently the default algorithm implemented in the Xtreme CT scanner. The proposed approach can be split down into 3 steps. The first two stages are to extract the cortical bone, and the last one is to estimate the pores in the cortical bone. The first step starts with applying the Laplace-Hamming filter, which effectively smooths the image and accentuate edges, then a fixed global threshold (40% of the maximum possible gray-scale value) is applied to binarize the image[153]. Afterwards, morphological operations (3D Dilation and erosion same size of [151]) with 2D connectivity filter are used to identify the periosteal surface.

As for the second step to extract the endosteal surface. It starts by inverting the original binary bone structure image (the output of the threshold phase in first step). This inverted image is then masked using the final output of the first step to leave only the marrow voxels. A 2D connectivity criterion to select the single largest mutually connected object is used to identify the background, thereby partially removing internal

trabeculae. A 3D thickness threshold (2 voxels) is then used to remove thin, disconnected trabeculae, and cortical cavities. This step is done to prevent small cortical pores from being included in the following dilation step, where they would otherwise be identified as part of the marrow space. Next, the same morphological operations applied on the first step are used to identify the endosteal surface. Finally, the binary difference between the first and second step yields the cortical bone mask (Figure 4.2).

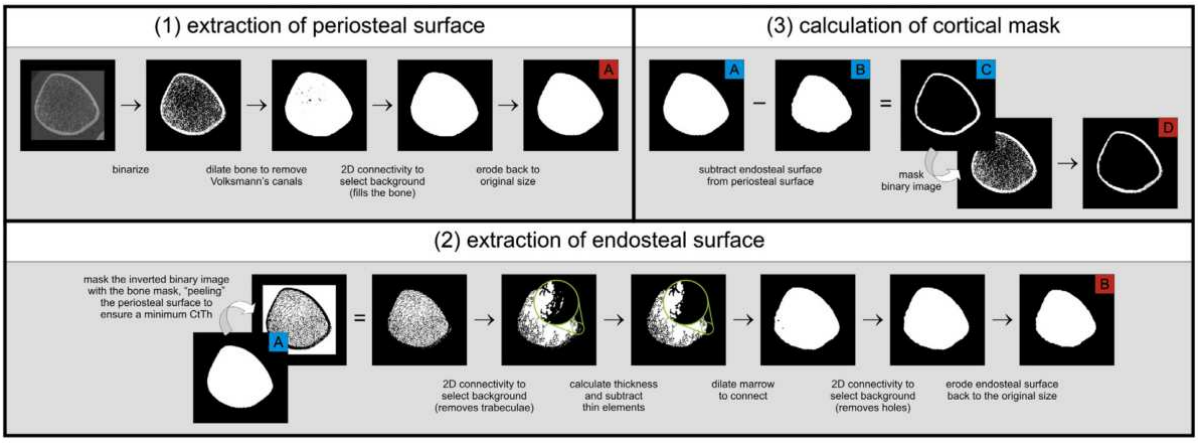

Figure 4.2: Summary of the two steps to extract the cortical bone in the Burghardt techniques. Source [59]

.

The third step uses the cortical mask extracted at the end of the first two steps and mask the binary image of the bone. The pore is defined as the void voxels in the cortical compartment that are surrounded by bone (referred as high confidence pores). These pores are identified by applying a 2D connectivity filter to select the small black holes in the cortical bone, excluding those connected to the marrow or the background (considered low confidence pores). Then, a hysteresis region-growing process, constrained to the z-direction, to correspond with the primary osteonal orientation, is applied to extract low-confidence pore voxels longitudinally connected to high-confidence pore voxels (i.e., seeds). Afterwards, the high, and low-confidence pores connected to high ones are combined together and added to the cortical bone, and a 2D connectivity filter is then applied to capture any residual intracortical void. Finally, pores with a volume smaller than 5 voxels are discarded as they likely represent noise or other artefactual features.

4.2.3 Valentinitsch technique

Another approach for the segmentation of HRpQCT bone images was proposed by Valentinitsch *et. al* [154]. This approach is a machine learning algorithm that uses the 3D texture to differentiate between the cortical and the trabecular bone. The background

voxels are excluded from analysis by using the auto contouring algorithm provided by the manufacturer. In the training phases, a trained operator segmented manually 14 distal radius images. Then, for each voxel in the image a local texture descriptor was calculated based on a cube of $15 \times 15 \times 15$ surrounding voxels [155]. The employed texture descriptor was based on: a three-dimensional gray level co-occurrence matrix (3D GLCM) [156, 157], the local structure tensor, and the Hessian matrix [158]. The authors justified the use of 3D GLCM to extract informations regarding the distribution of voxels within the cube. The structure tensor, and Hessian matrix capture the local image properties, such as tubularity, or flatness [159]. Afterwards, the random forest classifier is then trained using this feature space to capture the relationship between the features and the class membership of the voxels.

The training and testing of this approach was performed in a leave-one-out cross validation fashion. Therefore, they used 13 data samples for training and applied the classifier on 1 sample. They iterated this procedure so that there is a always disjoint between the training, and testing. However, the small number of data is not sufficient to cover the high variability introduced by normal anatomy of the bone. Therefore, this approach didn't receive enough attention, because of its poor accuracy and incapability of handling thin cortical bones [154].

4.2.4 Zebaze technique

This proposed approach by Zebaze et. al [160] segments the bone into three regions: cortical, trabecular and the transitional zone between them. This method works only on the last 40 slices of the bone, it begins by identifying a point in the middle (not necessary the centroid 'C') within the marrow cavity(Figure 4.3). From this point, a rectangular region of interest (ROI) starts and extends to the edge of the entire image. The ROI (Arm as identified by the authors) is selected so that its length is perpendicular to the bone surface. The Arm width (AW) is selected to be narrow enough to ensure that the periosteal edge of the bone within the Arm is locally linear but contains two or more rows of voxels. This avoids discontinuities due to noise or pores resulting in irregularities of bone boundaries after segmentation. $AW = R_i \times tan(acos(\theta))$ and is automatically quantified as a function of the distance between 'C' and the nearest periosteal surface (R_i). The value of (θ) is 0.98, chosen close to 1 so that the local portion of the periosteal

surface is almost linear.

After the extraction of this Arm (Figure 4.3), the attenuation profile curve is easily extracted. The separation between the different regions of the bone is illustrated in Figure 4.3. After analyzing the first ROI, the Arm sweeps in steps of 0.1° analyzing consecutive and overlapping Arms (ROIs) until a rotation of 360° is completed and the entire cross sectional slice has been assessed. This method however, is restricted only to the 40 most proximal slices because the cortical bone in the first 70 slices is thin and hard to identify [160]. This is the reason why the comparison against this approach is not considered in this thesis, because it classifies the bone into 3 overlapping regions instead of 2, and cannot handle thin cortices (prominent place of fractures, and the main focus of this thesis).

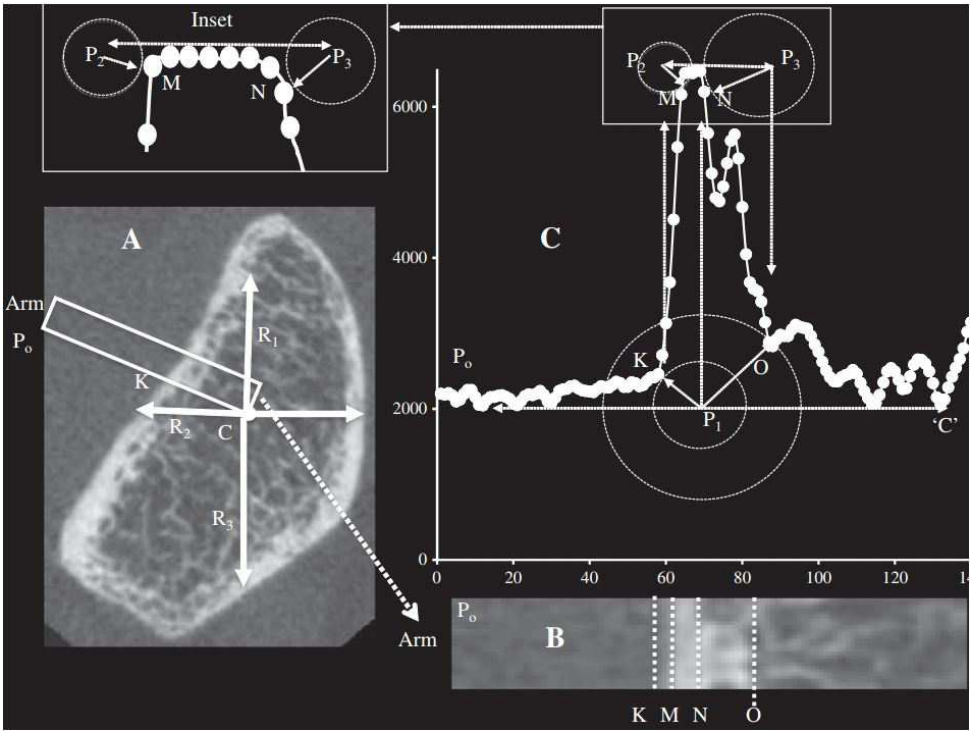

Figure 4.3: (A) HRpQCT distal slice of the radius, where the Arm originates from 'C' to P0. (B) A magnification of the Arm to show its contents (background, and bone edges). (C) The attenuation profile. The zone 'K' to 'M'is the transitional zone between background and cortical (excluded in their study). The zone 'M' to 'N' and 'O' to 'C' are the cortical and trabecular compartments respectively. Finally, the zone 'N' to 'O' is the transitional zone between cortical and trabecular [160].

As for the quantification of porosity in the cortical compartment. This approach quantifies the pores voxel by voxel, because the median size of Haversian canals is $50\mu m$ [161, 162]. It uses two terms (Level Of Fullness) LOF and (Level Of Void) LOV to identify the pores in the cortical bone. LOF is estimated by knowing the attenuation of a voxel in the background (no mineralized bone) known as P and the attenuation of a voxel that

contains only mineralized bone known as B. If I_i is the attenuation of voxel 'i' then

$$LOF_i(\%) = (I_i - P)/(B - P) \tag{4.1}$$

The LOE of each voxel (i.e., porosity) is then calculated by : $100 - LOF(\%)$. The porosity of the entire cortical bone (Po) is the average of all LOEs of all voxels (LOE_i) where n is the total number of voxels within the cortical compartment

$$Po = \sum_{i=1}^{n} LOE_i/n \tag{4.2}$$

4.3 Subjects recruited in the study

The HRpQCT data employed in this thesis is from the QUALYOR (Qualité Osseuse et Amélioration de la prédiction du risque fracturaire à LYon et ORléans) cohort with the ClinicalTrials.gov Identifier is NCT01150032. The cohort's objective is to test the bone quality variables (Trabecular/ Cortical parameters) to predict the risk of fracture in women identified as at low or at medium risk using BMD. This study includes 1525 menopausal women (1000 scanned in Lyon and 525 in Orléans), only Orléans data were available during the thesis. These women were recruited for 5 years study (from 2011 to 2016). The inclusion criteria were identified as: postmenopausal women, with age $\geqslant 50$ years, and osteopenic without fracture. For the non-inclusion criteria, participants were not accepted if they had one of the following conditions:

- Corticotherapy,
- antecedent treatment of osteoporosis,
- antecedent vertebral and non-vertebral fractures,
- Hormone treatment of menopause in progress,
- Taking drugs that are likely to affect bone metabolism,
- clinical signs of hepatic, cardiac, or respiratory insufficiency,
- Life expectancy < 4 years or serious illness which could affect the maintaining of the participant in the study for 48 months

For each woman, a face to face survey with rheumatologist was conducted and a written informed consent for the participation was obtained. The Qualyor study was

carried out in accordance with the recommendations of the revised version of the Helsinki declaration adopted by the world Medical Association in Seoul in 2008. The Patient Protection Committee (CPP Sud-Est IV) gave its approval to this study. Afterwards, two steps were conducted, the first concerned the clinical parameters: previous fracture, parents fracture, tobacco alcohol consumption, weight, height, etc. The second step concerned the imaging of patients where three scans took place:

- DXA scan to measure the BMD at hip, spine and wrist using the HOLOGIC Discovery,
- BMA scan of the calcaneum to analyze the bone texture,
- HRpQCT scan of the radius and tibia to measure cortical and trabecular bone parameters

In this study, only the latter is considered. The scan of radius and tibia are performed using the Xtreme CT scanner. The image scanning takes approximately 3 minutes per patient using the default human peripheral *in vivo* scanning protocol (60 kVp, 1000 A, 100 ms integration time, frame averaging of 1 and radiation dose of less than 3 μSv), to produce a 3D image of 110 slices (9.02 mm thick section (0.082 * 110 mm).

In the first part of the thesis (segmentation phase) from the 525 patients of QUALYOR in Orléans hospital, only 20 patients were considered to produce 20 radius and 20 tibia images. The performance of the proposed approaches was compared against the state of art techniques results using 40 images. In the 5 years period of this study, 45 patients have experienced 56 fractures (20 radius, 17 vertebral, 5 malleolus, 4 femoral neck, 3 pubic bone, 1 kneecap, and 1 elbow). In the second part of this thesis (Prediction of osteoporotic fractures), 176 patients (145 control, and 31 fractured) were selected based on the quality of the obtained acquisition (no artifacts) using the criterion of Piala *et. al* [163].

4.4 Quantitative metrics for evaluation

4.4.1 Ground truth

Unlike the literature techniques, to validate any method, a manual segmentation of the *in vivo* image of each patient was constructed using the ITK-SNAP software [164], which contains predefined image processing techniques developed for medical diagnosis

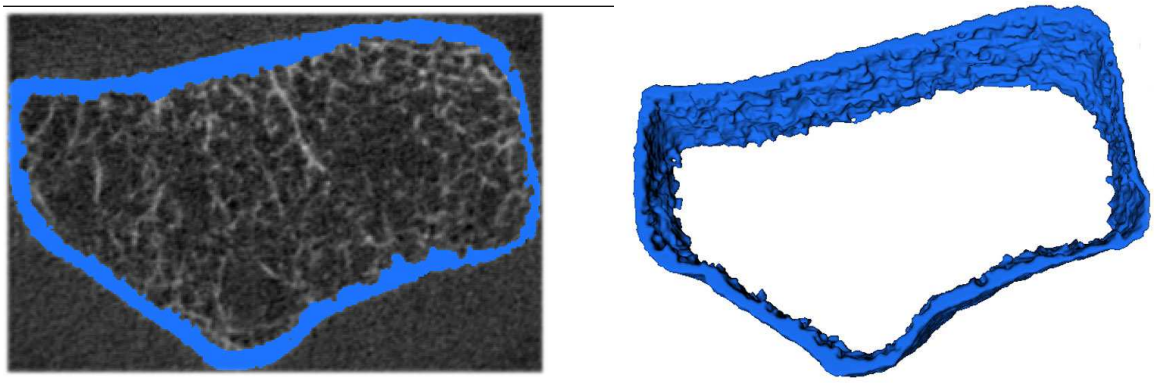

(a) (b)

Figure 4.4: 2D segmentation result of radius produced by the operator using ITK-SNAP (a), 3D Reconstruction of the segmentation result using ITK-SNAP (b)

aid. A trained operator segmented manually the 110 slices of the volume of the database. The manual segmentation process uses the default region based Chan-Vese active contours algorithm [85] implemented in ITK-SNAP. The process starts with placing manually circles on the cortical bone. Then, these circles start evolving in the image to cover all the cortical bone. Finally, the operator corrects the constructed volume and removes the false accepted voxels as it is illustrated in Figure 4.4

The manually segmented image of each dataset is used as gold standard to be compared with the segmentation result of each approach. Unlike the literature studies that focus only on cortical thickness error (Ct.Th error) and cortical total volume error (Ct.TV error), different volumetric and distance based measures were used in this study to evaluate the performance of each approach including the two proposed ones.

4.4.2 Dice similarity coefficient

The Dice Similarity Coefficient (DSC) [165] measures the spatial overlap between the gold standard result (G) and the computed segmentation result (S). DSC values are expressed in percentage ranging between 0 (no overlap) and 100% (perfect agreement). DSC is obtained using Equation (4.3):

$$DSC = \frac{2|S \bigcap G|}{|S| + |G|} \times 100 \tag{4.3}$$

where $|.|$ denotes the number of non zero elements. This metric takes into consideration the spatial distribution of the cortical bone by considering both non-cortical voxels (background and trabecular) classified as cortical and cortical voxels classified as trabecular or

background. Consequently, this measure is more accurate than simple volume or cortical thickness estimation employed in the literature studies, which could lead to overall small volume errors associated with largely inaccurate segmentations.

4.4.3 Absolute volume difference

The Absolute Volumetric Difference (AVD) is calculated as the ratio of the absolute difference between the gold standard volume (V_G) and the segmented volume (V_S) to the gold standard volume. The AVD is computed using the following formula :

$$AVD = \frac{|V_S - V_G|}{V_G} \times 100 \tag{4.4}$$

where V_G and V_S can be computed by multiplying the number of labelled voxels by the voxel dimensions.

4.4.4 Hausdorff distance

The Hausdorff distance and the error measurement based on it are used to evaluate the difference between the generated mesh by the method (S) and the manual (ground truth) mesh (G). The Hausdorff distance error between two meshes is defined as the distance between the corresponding sections of the meshes. For each point p in S the minimum distance between p and all points in G is calculated as follows:

$$e(p, G) = \min_{p' \in G} d(p, p'), \tag{4.5}$$

where $d(,)$ denotes the Euclidean distance between two points. The Hausdorff distance between S and G is defined as follows:

$$E(S, G) = \max_{p \in S} e(p, G) \tag{4.6}$$

As referred in [166, 167], this distance is (not symmetric) i.e. $E(S, G) \neq E(G, S)$. It is then convenient to define a two-sided distance (symmetrical Hausdorff distance) as the maximum of $E(S, G)$ and $E(G, S)$. Two additional measurements can be defined based on the Hausdorff distance; the mean and root-mean-square errors. The mean error E_m

between two surfaces S and G is calculated as follows:

$$E_m = \frac{1}{|S|} \int_{p \in S} e(p, G) dS, \tag{4.7}$$

where $|S|$ denotes the area of S. From this, the definition of a root mean square error E_{rms} follows naturally:

$$E_{rms} = \sqrt{\frac{1}{|S|} \int_{p \in S} e(p, G)^2 dS} \tag{4.8}$$

For more details refer to [166, 167].

As a complementary measurement, a qualitative evaluation was conducted to assess the location predominance of segmentation errors and locate the misclassified trabecular and cortical voxels individually for each method.

4.5 Conclusion

This chapter provides the state of the art techniques of HRpQCT image segmentation methods including Dual threshold, Burghardt, Valentinitsch and Zebaze. Afterwards, a full description of the database employed in this thesis, followed by the different metrics used to evaluate the performance of the approaches.

On the following chapter, two new methods for HRpQCT image segmentation are proposed, one based on fuzzy energy active contours and the second presents a novel framework of 3D dual contours.

Chapter 5

Proposed Active Contours approaches for HRpQCT Image Segmentation

5.1 Introduction

This chapter encompasses the different contributions achieved during the thesis. First, a new fuzzy energy active contours approach coupled with a post-processing technique to separate the cortical bone from the trabecular is details. Second, a novel dual active contours approach able to segment the cortical bone and its erosions automatically. Then, finally to validate the performance of these approaches, the different measures illustrated in Chapter 4.4 have been implemented and compared to state of art techniques.

5.2 Method 1: Fuzzy energy based HRpQCT cortical bone segmentation

Classical active contours are sensitive to noise and cannot handle objects with ill defined boundaries, the case in HRpQCT images. The employment of fuzzy clustering logic [168, 131] has proved its applicability in active contours to solve the noise and the boundaries discontinuity problems.

The proposed fuzzy energy based active contours model assumes like most ACM, that the image is divided into two subsets. The idea is to move the deformable con-

tours minimizing an energy function that measures the difference between a constant that approximates the statistical information of the image intensity within a subset and the actual image intensity at every pixel of the image.

Let's assume that Ω is the image domain and C is a closed contour that separates the image Ω into two regions: ($InsideC$) and non bone ($OutsideC$), which both have distinct values of intensity, their energy function is defined as follows:

$$\begin{aligned} E(C, c_1, c_2, u) = \mu \cdot Length(C) + \lambda_1 \int_{\Omega} |I(x,y) - c_1|^2 [u(x,y)]^m \, dx \, dy \\ + \lambda_2 \int_{\Omega} |I(x,y) - c_2|^2 [1 - u(x,y)]^m) \, dx \, dy \end{aligned} \tag{5.1}$$

where the first term represents the regularization term (internal force) which assures the smooth shape of the contour. The length parameter μ has a scaling role, the smaller it is the more small objects can be detected. Therefore, in our study we fixed $\mu = 0$ so small trabeculae of the trabecular bone can be detected. The remaining terms of Equation (5.1) represent the fitting terms (external force), where the constants c_1 and c_2 are the averages of pixels intensity inside and outside C, respectively. $u(x, y) \in [0, 1]$ is the belonging (membership) function of the pixel $I(x, y)$ to inside the contour and m is a weighting exponent on this function.

$$c_1 = \frac{\int_{\Omega} [u(x,y)]^m I(x,y) \, dx}{\int_{\Omega} [u(x,y)]^m \, dx}, c_2 = \frac{\int_{\Omega} [1 - u(x,y)]^m I(x,y) \, dx}{\int_{\Omega} [1 - u(x,y)]^m \, dx}, \tag{5.2}$$

The proposed fuzzy membership function $u(x, y) \in [0, 1]$, is a Gaussian function assigned to each pixel, where it is inversely related to the distance of the pixel from the center of the cluster $InsideC$. Using the new fuzzy membership function, a new contour is derived. This contour is implicitly represented via a two dimensional lipschitz continuous function defined as follows:

$$\begin{aligned} C &\equiv \{(x,y) \in \Omega : u(x,y) = 0.05\}, \\ InsideC &\equiv \{(x,y) \in \Omega : u(x,y) > 0.05\}, \\ OutsideC &\equiv \{(x,y) \in \Omega : u(x,y) < 0.05\}, \end{aligned} \tag{5.3}$$

The proposed fuzzy membership function is designed to focus on the fuzzy inhomogeneous regions of the image. Therefore, the following function associated to each pixel will decrease iteratively depending on the intensity of the pixels of each cluster. The exponential function in Equation (5.4) was used to increase the intensity difference values so the very fuzzy pixels which are difficult to spot can be detected. The concept of the fuzzy membership function was changed here to give more interest to the inside contour region. In the case of pixels belonging to *OutsideC*, the denominator of Equation (5.4) is very high, hence $u(x, y)$ is very small. As for pixels belonging to *InsideC*, the denominator of Equation (5.4) is very small, hence the value of u(x,y) is bigger than those of the *OutsideC* case. The 0.05 value was chosen empirically after a set of tests, after noticing that the membership function of pixels *OutsideC* converge highly to 0. The function is defined as follows:

$$u(x,y) = \frac{m}{exp\left(\frac{\lambda_1 (I(x,y)-c_1)^2}{\lambda_2 (I(x,y)-c_2)^2}\right)} \tag{5.4}$$

The usual procedure to solve the minimization problem of active contours (Equation (5.1)) is to derive the Euler-Lagrange equation and then to use explicit time marching. However, the time and computational cost of this procedure are too high [168], therefore, in this study, we employed the following algorithm to minimize the energy of Equation (5.1):

To compute the difference between the new and old fuzzy energy for each image pixel I_o, the same equation proposed by [168] is used:

$$\begin{aligned} \triangle E = \lambda_1 s_1 \frac{[u_n^m - u_0^m](I_0 - c_1)^2}{s_1 + u_n^m - u_0^m} \\ + \lambda_2 s_2 \frac{[(1-u_n)^m - (1-u_o)^m](I_0 - c_2)^2}{s_2 + (1-u_n)^m - (1-u_o)^m} \end{aligned} \tag{5.5}$$

where I_o is the current pixel and u_o its corresponding degree of membership. u_n is the new membership function calculated using Equation (5.4), $s_1 = \sum_{i,j}[u(i,j)^m]$, and $s_2 = \sum_{i,j}[1 - u(i,j)]^m$. If $\triangle E < 0$, then change u_o with u_n value, else keep the old (u_o) value. This step is repeated for the whole image pixels using Jacobi iterations to compute the total energy E of the image. In [168], the authors explain the development of Equation (5.5).

The different steps to minimize the proposed energy are further explained in the

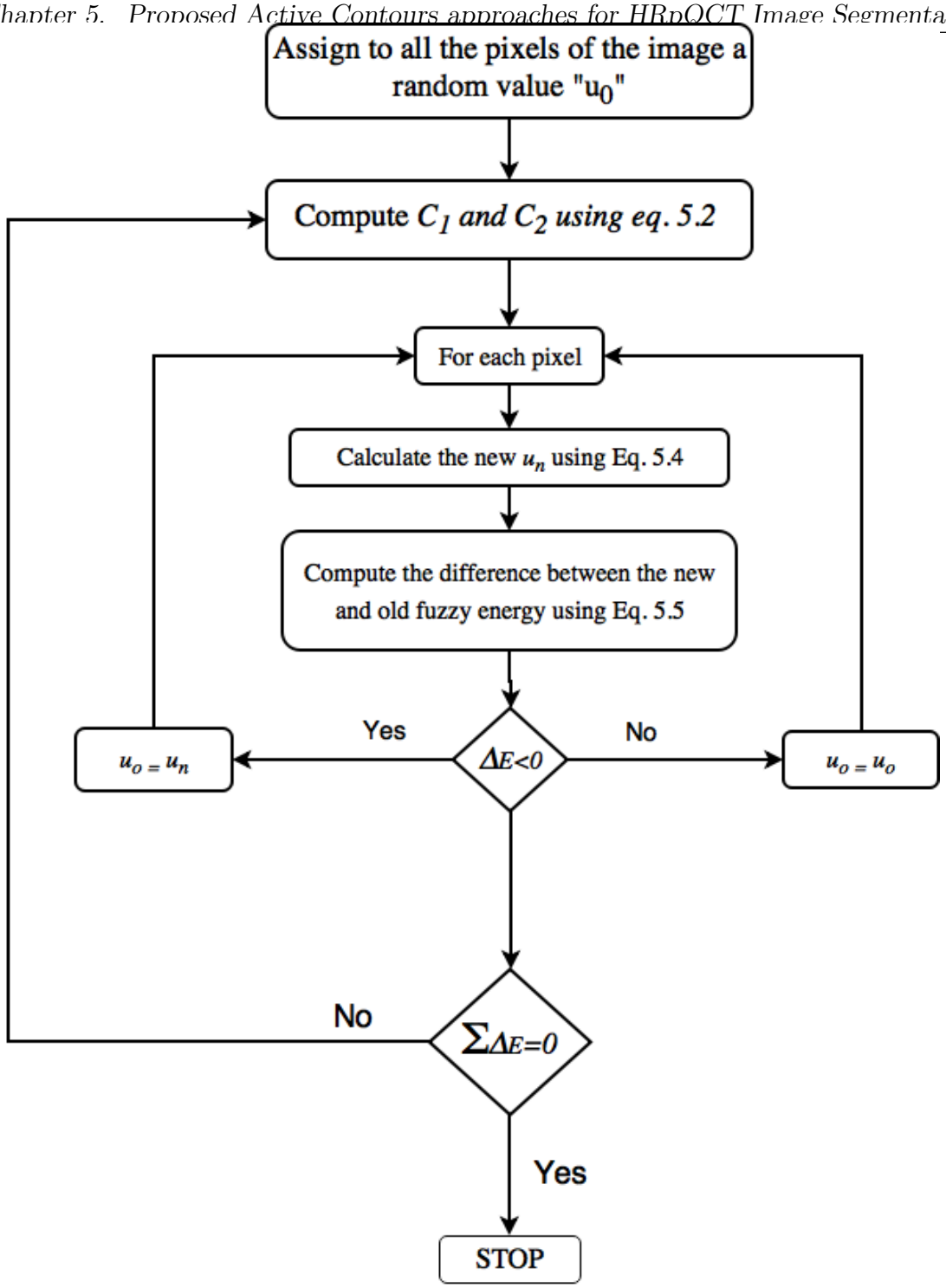

Figure 5.1: The minimization algorithm of the proposed fuzzy active contours energy.

flowchart (Figure 5.1)

Nevertheless, this proposed approach can only binarize the HR-pQCT image (separate the bone from the background). Figure 5.2 illustrate the result of the proposed approach in segmenting the bone from HRpQCT image compared to FEBAC. However, the aim of this thesis is to not only separate the bone from the background, but also to isolate the cortical bone from the trabecular one. To achieve this, we propose an approach that employs the proposed fuzzy active contour model followed by a post-processing al-

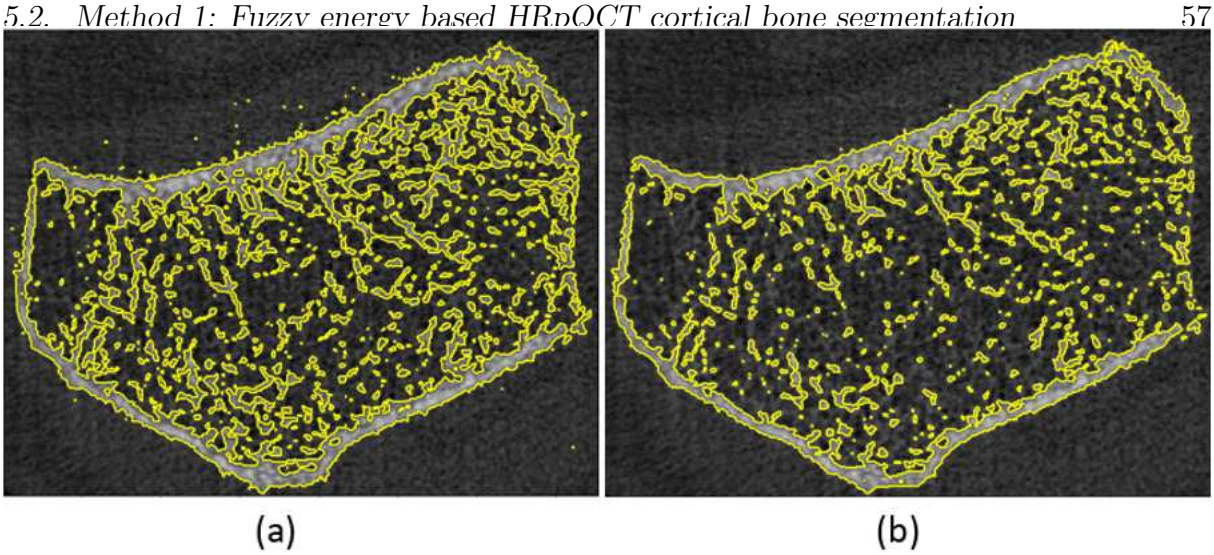

Figure 5.2: Segmentation results on ultra-distal slice of radius, using (a) proposed approach, and (b) FEBAC method

gorithm designed to mimic the clinicians behaviour while segmenting the inner contour of the cortical bone as defined in what follows.

Bone filling technique The bone filling algorithm was mainly developed to mimic the behaviour of clinicians in the delineation of the inner contour of the cortical bone. The structure of the trabecular bone resembles sponge or honeycomb with many open spaces connected by flat planes known as trabeculae. However, the proposed fuzzy energy active contours algorithm considers these spaces as background. To fill them, we have developed a filling algorithm that runs through the pixels of the image, and if it finds a background pixel surrounded by four bone pixels (two in the horizontal direction and two on the vertical one as illustrated in Fig. 5.3), this latter turns into a bone pixel. This novel filling technique is unlike the morphological operations and filling holes technique employed in [151, 152], because it can fill the trabecular spaces even when the cortical bone has breaks. Moreover, it produces a more uniform representation of the inner contour of the cortical bone.

*	*	1	*	*
*	*	0	*	*
1	0	0	0	1
*	*	0	*	*
*	*	1	*	*

→

*	*	1	*	*
*	*	0	*	*
1	0	1	0	1
*	*	0	*	*
*	*	1	*	*

Figure 5.3: An example of a background pixel (value = 0) surrounded by four bone pixels (value = 1). In this case, the value of the background pixel turns to 1. A pixel of value = *, is either 0 or 1.

The different steps of the algorithm are presented in the following:

Algorithm : Proposed protocol to extract the cortical bone

1: Binarize the image using the proposed fuzzy energy active contours model explained in details in Chapter 5.2
2: Remove the wrongfully identified pixels using a 3D connectivity filter
3: Fill in the trabecular bone using the proposed filling technique (see Chapter 5.2) to extract the periosteal surface (the outer contour of the cortical)
4: Apply morphological operation (dilation and erosion) using a small structuring element (disk of 5 pixels radius) to smoothen the outer contour of the cortical
5: Erode the output of step 4 using a disk of 10 pixels and apply the result as a mask on the output of step 1 to keep only the trabecular bone.
6: Apply a 3D connectivity filter to select the biggest white region, this removes the Haversian, Volkman's canals and the pores of the cortical bone
7: Fill in the trabecular space using the same filling technique used in step 3 to extract the trabecular area (the inner contour of the cortical).
8: Apply a 2D connectivity and a Gaussian filter on the output of step 7 to refine the segmentation result and remove the cortical pores
9: Subtract the result of step 8 from the one of step 4 to extract the cortical bone (Fig. 5.4).

A detailed illustration of the 9 steps to extract the cortical bone from the HR-pQCT image is provided in the flowchart of Figure 5.4, where each step of the algorithm is illustrated.

5.2.1 Fuzzy energy active contours performance

The performance of the proposed approach was compared to three methods in the ultra-distal site scan (thin cortices). The two first methods are the dual threshold (DT) method [151] and Burghardt technique (BT) [152]. The third method is FEBAC technique[168] followed by the same post-processing algorithm employed in our approach. The two other technique[154, 160] weren't included because of their inability of handling ultra-distal sites.

Table 5.1 shows the results of the comparison metrics described in Section 4.4 applied to the segmentation results of each method in the case of images of the radius. The mean and SD in Table 5.3 are calculated with respect to the whole dataset and not to the 110 slices for a selected subject. The performance of the proposed approach is very satisfactory, where it provided statistically the highest DSC (89 $\pm$ 0.72%). Both BT and DT produced an over or/and under estimation of the segmentation result compared to the ground truth, hence, the DSC is lower than our approach (BT: 87.18 $\pm$ 0.95%) and

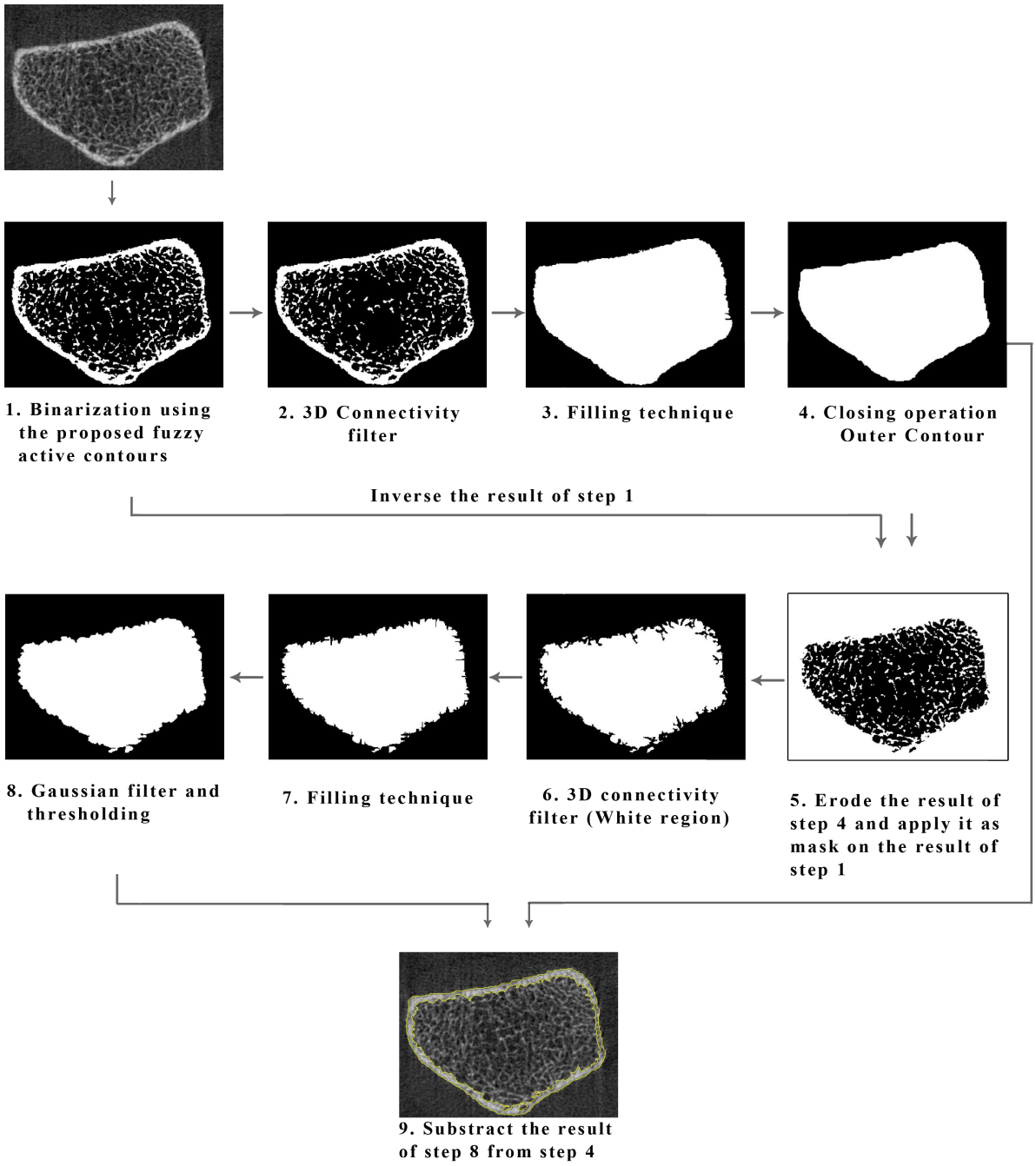

Figure 5.4: The flowchart of the proposed algorithm to extract the cortical bone

(DT: 83.31 ± 1.88). Similarly, the Hausdorff distance errors demonstrate the efficiency of the approach and its capability of handling thin cortices, unlike DT who produced the highest error in all dataset (E_m= 1.88 ± 1.53 and E_{rms} = 3.93 ± 3.88). This is mainly due to the two empirically chosen thresholds of the approach.

In the case of FEBAC method, the Hausdorff distance error between GT (ground truth) and FEBAC's result (E_m = 1.06 ± 0.12 and E_{rms} = 1.56 ± 0.33) is lower than DT error. However, for the DSC metric, FEBAC's approach provides the lowest value of the different methods. This is due to it's inability to handle the low intensity values of the

cortical bone. Therefore, the filling process cannot accurately extract the outer contour region (DSC = 71.9%)

For the segmentation volume error illustrated in Table 5.3 with the AVD metric, similarly the proposed approach provides the lowest value compared to the other methods. However, BT produced the highest error value (AVD = $15.03 \pm 7.42\%$), which contradicts the dice similarity coefficient and the Hausdorff distance results. This illustrates that using the AVD metric can lead to overall small volume errors associated with largely inaccurate segmentations. Therefore, this metric is considered as an unreliable error measure and cannot be used alone to evaluate the segmentation result as used in [151, 152, 154, 160].

Table 5.1: Comparison of the accuracy of the different methods versus the ground truth in the case of the radius using different metrics

Parameters	**Units**	**Proposed** Mean ± SD	**FEBAC** Mean ± SD	**BT** Mean ± SD	**DT** Mean ± SD
DSC	[%]	89 ± 0.72	81.93 ± 1.06	87.18 ± 0.95	83.31 ± 1.88
AVD	[%]	11.03 ± 4.76	14.77 ± 5.72	15.03 ± 7.42	12.59 ± 7.06
Mean error	[mm]	0.72 ± 0.08	1.06 ± 0.12	0.95 ± 0.1	1.88 ± 1.53
RMS error	[mm]	1.18 ± 0.09	1.56 ± 0.31	1.46 ± 0.33	3.93 ± 3.88

Table 5.2 illustrates the comparison of the different approaches in the tibia images. The overall agreement (DSC) between the segmentation result of the proposed method and FEBAC with GT is better than in the case of radius (proposed: $90.4 \pm 1.23\%$ and FEBAC: $87.18 \pm 0.96\%$). This is because the cortical bone in the tibia is larger and thicker than in the radius, hence, it is easier to segment. However, this is not the case for DT and BT, because of the complex structure of the inner contour in the image of the tibia, where over and under-estimation of the cortical bone occur.

In the AVD error rate, a different disproportion of the results is noticed like in the case of the radius. BT produced the highest error rate compared to DT and FEBAC. On the other hand the lowest AVD error in tibia dataset was produced by the FEBAC approach (2.44 ± 0.76). This contradicts DSC and Hausdorff results and demonstrates that the volume error is an unreliable evaluation metric.

Table 5.2: Comparison of the accuracy of the different methods versus the ground truth in the case of the tibia using different metrics

Parameters	Units	Proposed	FEBAC	BT	DT
		Mean ± SD	Mean ± SD	Mean ± SD	Mean ± SD
DSC	[%]	90.4 ± 1.23	87.18 ± 0.96	85.82 ± 2.92	83.14 ± 3.47
AVD	[%]	3.95 ± 2.8	2.44 ± 0.76	18.45 ± 9.26	10.57 ± 10.95
Mean error	[mm]	1.01 ± 0.09	1.23 ± 0.19	2.09 ± 1.49	3.58 ± 3.22
RMS error	[mm]	1.57 ± 0.47	1.64 ± 0.4	3.88 ± 2.94	8.33 ± 9.14

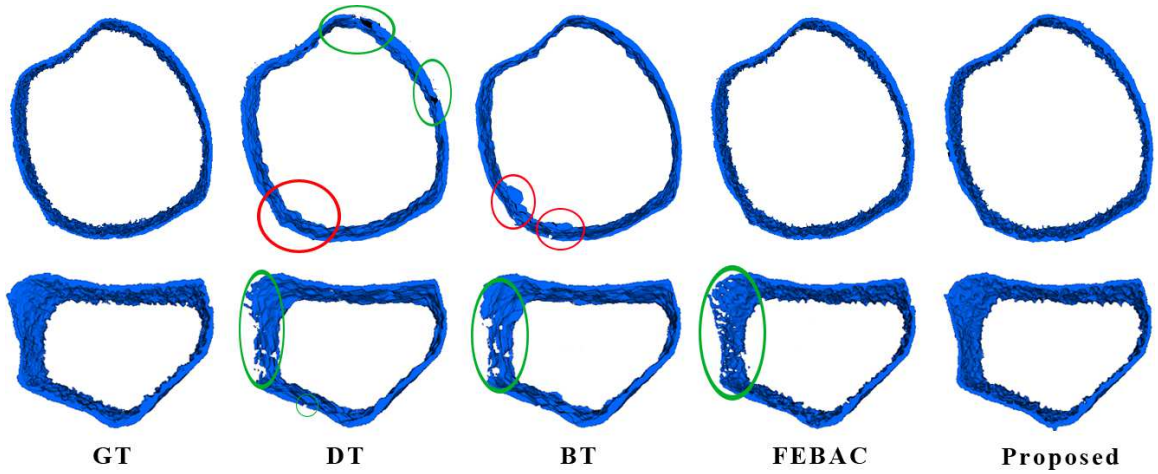

Figure 5.5: Comparison between the result of the manual segmentation (GT) and the different approaches in the case of the tibia (first row) and the radius (second). Highlighted in red are the over-estimation of the mask. The cortical breaks (highlighted in green) are apparent on all the approaches except in our proposed technique.

5.3 Method 2: Dual Active Contours

The only drawback with the previous approach is the post-processing algorithm, which only delineates the cortical mask and does not detect the cortical pores automatically. In this thesis, another active contours approach has been proposed based on the local energy.

This section presents the proposed energy framework to guide the dual active contours model. Due to the inhomogeneity of the different regions in medical images, within this framework, segmentation is not based on a global region model. Instead, a new concept is introduced, where the object of interest (foreground: cortical in our case) is considered between two curves.

The outer curve is dedicated to the outer contour of our desired object. For each point in the curve, the local energy inside and outside the curve is calculated. Then,

based on these calculations, the curve evolves to reduce the local energy as in [113]. Once the outer curve's energy is minimised, the inner curve is triggered and starts evolving to reduce the local energy between the two curves. This concept avoids the hypothesis that the active contours evolve to separate between two regions with different piecewise constant intensities.

Let I be an image in the Ω domain and C_1, C_2 are the dual closed contours. The outer contour C_1 is defined as the zero level set of a signed distance ϕ_1, i.e. $(C_1 = \{x|\phi_1(x) = 0\})$. The interior of the contour C_1 is then defined by the following Heaviside function:

$$H(\phi_1(x)) = \begin{cases} 1, & \phi_1(x) < -\epsilon \\ 0, & \phi_1(x) > \epsilon \\ \frac{1}{2}\{1 + \frac{2}{\pi}\arctan(\frac{\phi_1(x)}{\epsilon})\}, & \text{otherwise} \end{cases} \tag{5.6}$$

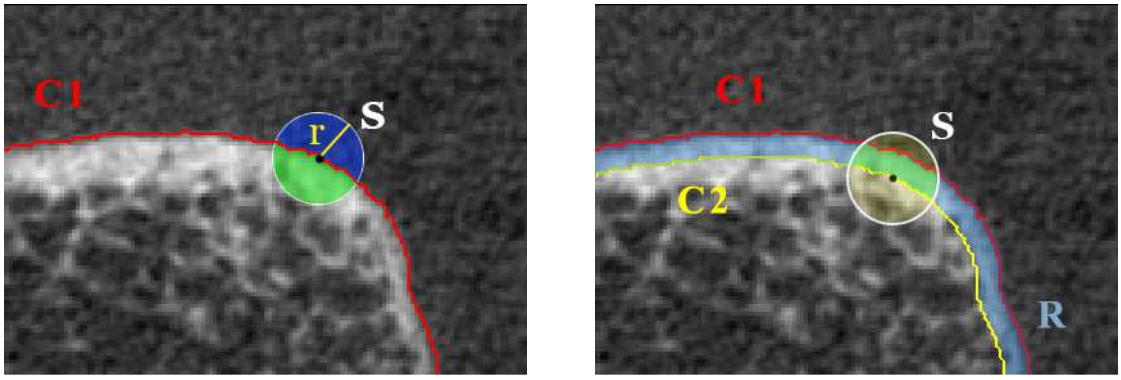

(a) **(b)**

Figure 5.6: The neighbourhood of each point x (black small dot) along both curves is represented by the spheroid $S(x,.)$. This spheroid is split by the contour into local interior (green $= u_x$) and local exterior (blue $= v_x$) (a). The spheroid of each point along the curve C_2 is split by the two contours C_1 and C_2 and only the region between them is considered (green) (b).

Based on the definition of the Heaviside function of C_1, it is easy to define another contour inside C_1, as illustrated in Figure. 5.6b. The initialisation of C_2 can be achieved using the following definition:

$$C_2 = \{x|H(\phi_1(x)) = t\}, \tag{5.7}$$

the smaller the parameter $t < 0$ is, the higher the distance between the two contours is. After the definition of C_2, its level set function $\phi_2(x)$ can be achieved using the following

equation:

$$\phi_2(x)) = \begin{cases} d(x, C_2), & x \in \Omega_{insideC_2} \\ -d(x, C_2), & x \in \Omega_{outsideC_2} \end{cases} \tag{5.8}$$

where $d(x, C_2)$ is the Euclidean distance between the point x and the contour C_2.
The energy of the new Dual Active Contours (DAC) model is based on the energy of the two contours and can be defined as follows:

$$E(\phi_1, \phi_2) = E(\phi_1) + \Gamma(C_1) \cdot E(\phi_2) \tag{5.9}$$

where, $\Gamma(C_1)$ is a weighting function that has a reverse relationship with the convergence of the first curve, and it is defined as follows:

$$\Gamma(C_1) = \begin{cases} 1, & E(\phi_1) = min(E(\phi_1)) \\ 0, & otherwise \end{cases} \tag{5.10}$$

The energy of C_1 and C_2 is defined in details in the following section. In addition to the energy of the two curves a constraint function was introduced to control and preserve the distance between the two curves. This can be set by the user based on the application, it is defined as follows :

$$D(\phi_1, \phi_2) = |D - d(\phi_1, \phi_2)| \tag{5.11}$$

where, D is the maximum distance allowed between the two surfaces ϕ_1 and ϕ_2, and $d(.,.)$ is the Euclidean distance between the two curves (surfaces in 3D).

5.3.1 Outer contour energy

For the energy of the first curve $E(\phi_1)$, the local active contour framework proposed by Lankton *et al.* [113] is used, where each point along the curve evolves reducing a local energy. The energy of contour C_1 is defined by the following function :

$$\begin{aligned} E(\phi_1) = \int_{\Omega_x} \delta(\phi_1(x)) \Bigg(\int_{\Omega_y} S(x,y) \cdot \big[H(\phi_1(y))(I(y) - u_x)^2 + \\ (1 - H(\phi_1)) \cdot (I(y) - v_x)^2 \big] dy \Bigg) dx, \end{aligned} \tag{5.12}$$

where Ω_x represents all the points x in the Ω domain and Ω_y represents the points y the neighbouring pixels of the point x. The constants u_x and v_x are the averages of the pixels intensity inside and outside the local neighbourhood of the point x. For simplicity reasons we define:

$$M_1(\phi) = H(\phi), \qquad M_2(\phi) = 1 - H(\phi),$$
$$f_1 = (I(y) - u_x)^2, \qquad \text{and } f_2 = (I(y) - v_x)^2.$$

$\delta(\phi_1(x))$ is the Dirac function which represents the derivative of the Heaviside function (eq. 5.6) and can be defined as follows:

$$\delta(\phi_1(x)) = \begin{cases} 1, & \phi_1(x) < -\epsilon \\ 0, & \phi_1(x) > \epsilon \\ \dfrac{\epsilon}{\pi(\epsilon^2 + \phi(x)^2)}, & \text{otherwise} \end{cases} \tag{5.13}$$

$$\begin{aligned} u_x &= \frac{\int_{\Omega_y} S(x,y) \cdot M_1(\phi_1(y)) \cdot I(y)\, dy}{\int_{\Omega_y} S(x,y) \cdot M_1(\phi_1(y))\, dy}, \\ v_x &= \frac{\int_{\Omega_y} S(x,y) \cdot M_2(\phi_1(y)) \cdot I(y)\, dy}{\int_{\Omega_y} S(x,y) \cdot M_2(\phi_1(y))\, dy}, \end{aligned} \tag{5.14}$$

$S(x,.)$ represents the local neighbourhood of the point x. The interaction of $S(x,.)$ with the interior and exterior regions is illustrated in Figure. 5.6a.

$$S(x,y) = \begin{cases} 1, & ||x - y|| < r \\ 0, & \text{otherwise} \end{cases} \tag{5.15}$$

where r represents the radius of the spheroid of the curve illustrated in Figure. 5.6. The bigger the radius, the more pixels are involved in the evolution of each point in the curve.

5.3.2 Inner contour energy

Once the energy of C_1 is minimised, the second contour C_2 starts evolving the same way of C_1 but using a novel local energy. Each point along the contour evolves reducing

a local energy defined as follows :

$$E(\phi_2) = \int_{\Omega_x} \delta(\phi_2(x)) \Big(\int_{\Omega_y} S(x,y) R(y) \cdot H(\phi_2(y)) ((I(y) - w_x)^2) dy \Big) dx \tag{5.16}$$

where the constant w_x represents the average of pixels intensities between the two curves, defined as follows:

$$w_x = \frac{\int_{\Omega_y} S(x,y) \cdot R(y) \cdot H(\phi_2(y)) \cdot I(y)\, dy}{\int_{\Omega_y} S(x,y) \cdot R(y) \cdot H(\phi_2(y))\, dy}, \tag{5.17}$$

$R(.)$ is a function developed to assure that only the points between the two curves are considered. The interaction of both $R(.)$ and $S(x,.)$ with the two curves is illustrated in Figure. 5.6b.

$$R(y) = \begin{cases} 1, & y \in \{R_{C_1} \setminus R_{C_2}\} \\ 0, & \text{otherwise} \end{cases} \tag{5.18}$$

where R_{C1} and R_{C2} are the regions inside C_1 and inside C_2, respectively.

Finally, to ensure the smoothness of the contour C_1, the commonly regularization term developed in [85] is used. The final energy functional of the dual contours is defined in details as follows:

$$\begin{aligned} E(\phi_1,\phi_2) = & \\ & \int_{\Omega_x} \delta(\phi_1(x)) \Big(\int_{\Omega_y} S(x,y) \cdot \big[\sum_{i=1}^{2} M_i(\phi_1(y)) \cdot f_i \big] dy \Big) dx \\ & + \Gamma(C_1) \int_{\Omega_x} \delta(\phi_2(x)) \Big(\int_{\Omega_y} S(x,y) \cdot R(y) \cdot H(\phi_2(y)) \cdot f_3 dy \Big) dx \\ & + \mu_1 \int_{\Omega_x} \delta\phi_1(x) || \bigtriangledown \phi_1(x) || dx + \Gamma(C_1) \cdot \mu_2 \int_{\Omega_x} \delta\phi_2(x) || \bigtriangledown \phi_2(x) || dx \end{aligned} \tag{5.19}$$

By taking the first variation of this energy with respect to ϕ_1 and ϕ_2, the following

evolution equation is obtained:

$$\begin{aligned}\frac{\delta(\phi_1,\phi_2)}{\delta t} &= \delta(\phi_1(x))\int_{\Omega_y} S(x,y)\cdot\delta(\phi_1(x))\cdot(f_1-f_2)dy \\ &+\Gamma(C_1)\cdot\delta(\phi_2(x))\int_{\Omega_y} S(x,y)\cdot R(y)\cdot\delta(\phi_2(y))\cdot f_3 dy \\ &+\mu_1\delta\phi_1(x)div(\frac{\bigtriangledown\phi_1(x)}{\mid\bigtriangledown\phi_1(x)\mid})+\Gamma(C1)\cdot\mu_2\delta\phi_2(x)div(\frac{\bigtriangledown\phi_2(x)}{\mid\bigtriangledown\phi_2(x)\mid})\end{aligned} \tag{5.20}$$

where $(f_1 - f_2)$ can be developed as follows:

$$f_1 - f_2 = u_x^2 - v_x^2 + 2I(y) * (u_x + v_x) \tag{5.21}$$

For simplicity reasons and for further development, we refer to the first term of eq. 5.20 as "A", the second as "B", the third as "C", and the fourth as "D".

At each time step dt, ϕ must be reinitialized to be the Signed Distance Function (SDF) to its zero-level curve. This procedure is assured through using the Sussman technique [169] to prevent the level set function of becoming too flat.

The steps of the proposed algorithm are detailed in the following algorithm:

Algorithm : The DAC algorithm

Initialize manually Contour C_1
Compute $\Gamma(C_1)$ using (eq. 5.10)
while $\Gamma(C_1) == 0$ **do**
  for each point $x \in C_1$ **do**
    Compute u_x and v_x using (eq. 5.14)
    Compute $f_1 - f_2$
    Compute the first term (A) of (eq. 5.20)
  end for
  Compute the third term (C) of (eq. 5.20)
  $\phi_1 = \phi_1 + (A + C) * dt$
  Reinitialize ϕ_1 to be SDF
  Compute $\Gamma(C_1)$
end while
Initialize ϕ_2 using (eq. 5.8)
while $\big(E(\phi_2) <> min(E(\phi_2))\big)$ **do**
  for each point $x \in C_2$ **do**
    Compute w_x using (eq. 5.17)
    Compute the second term (B) of (eq. 5.20)
  end for
  calculate the fourth term (D) of (eq. 5.20)
  $\phi_2 = \phi_2 + (B + D) * dt$
  Reinitialize ϕ_2 to be a SDF
end while

5.3.3 Implementation

In our method, the main computational cost of each iteration resides in the computation of u_x, v_x, w_x, F_1 and F_2. Based on [112], we noticed that all these terms can be rewritten as a suite of convolutions, for instance v_x can be written as follows :

$$v_x = \frac{S(x,y) * I - S(x,y) * (H(\phi_1)I)}{S(x,y) * \mathbb{1} - S(x,y) * H(\phi_1)} \tag{5.22}$$

where $*$ represents the convolution product and $\mathbb{1}$ is the matrix with the value $\mathbb{1}$ in all its elements. It is obvious that the terms $[S(x,y) * I]$ and $[S(x,y) * \mathbb{1}]$ do not depend on the evolution of ϕ_1, therefore, they can be computed once before the iterations of the proposed algorithm. The second term of the nominator and the denominator of v_x are the same in u_x. In the same way w_x can be computed.

With the help of the Fast Fourier Transform (FFT), the complexity of the convolution product can be reduced from $O(n^6)$ to $O(n^3 log^3 n)$. In this approach, the FFT operator was applied to all the convolutions operations to minimize quickly the energy of eq. 5.19, as it is illustrated in the experiments section.

The execution time, the computation complexity of the proposed approach, and the proposed implementation scheme were examined, using a 2.4 GHz dual core based PC to run the segmentation algorithm implemented in Matlab. First, we examined the effect of the employment of the convolution product on the outer curve. The testing was applied on an image of a radius bone with the following characteristics (198*284*40) with an outer contour of 10 pixels radius. Using the standard algorithm, each iteration takes approximately 35.7 seconds, and after applying the convolution process, the iteration time reduced to 12.5 seconds. With the employment of the FFT on the convolution product, the complexity of the algorithm is further reduced to achieve 2.5 seconds for each iteration.

Second we examines the convergence of the dual contours and their time properties while segmenting the tibia. Figure. 5.7 illustrates the interaction between the dual contours and the convergence of both of them.

5.3.4 DAC's performance

Different experiments were performed to investigate the performance of the proposed DAC approach on the segmentation of synthetic and medical images. Synthetic test

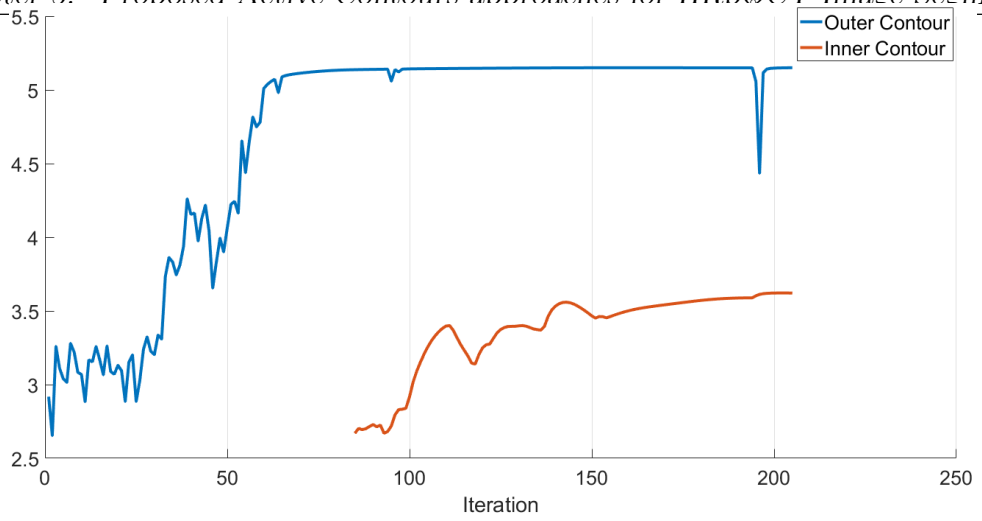

Figure 5.7: Convergence and timing properties of DAC. The inner contour starts evolving at the iteration 85 where the outer contour converged.

images were constructed from the Brodatz database [170].

For the real medical images, we used HR-pQCT bone image (radius), and an MRI Image of the bladder wall.

The obtained results are organised in three parts. The first part evaluates the proposed approach efficiency on synthetic images. The second part compares the performance of the proposed approach with the one achieved by the state of art techniques (Burghardt (BT) and dual threshold (DT)) on HRpQCT images. Whereas, the third part examines the effect of the different parameters of the DAC technique, starting with the local radius effect, the initial distance between the two contours and the proposed contours initialization method.

Segmentation of Synthetic Data

To provide a fair comparison, both compared methods used the same initial contour, which is painted in red. Figure. 5.8 illustrates an example of segmentation results obtained by the application of the DAC and Lankton approaches [113] on two different images. As can be seen, the proposed approach has successfully segmented the existing inhomogeneous area between the two regions. The Lankton method[113] was only capable of separating between the background and the outer boundary of the region of interest. This is because the contours of the proposed approach evolve with a constrained distance between them, along with the hypothesis that they are both reducing a shared energy. The Dice Similarity Coefficient (DSC) was calculated to compare the segmentation results. The average of the DAC approach is 98.2 ± 1.2. The results show that the

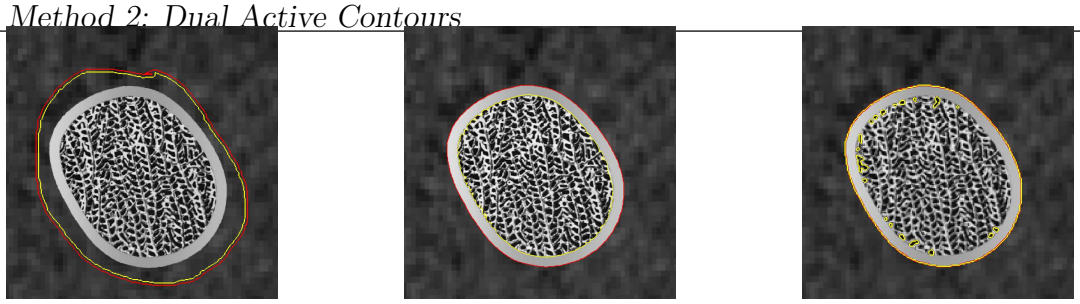

(a) Initialization **(b)** DAC **(c)** Lankton [113]

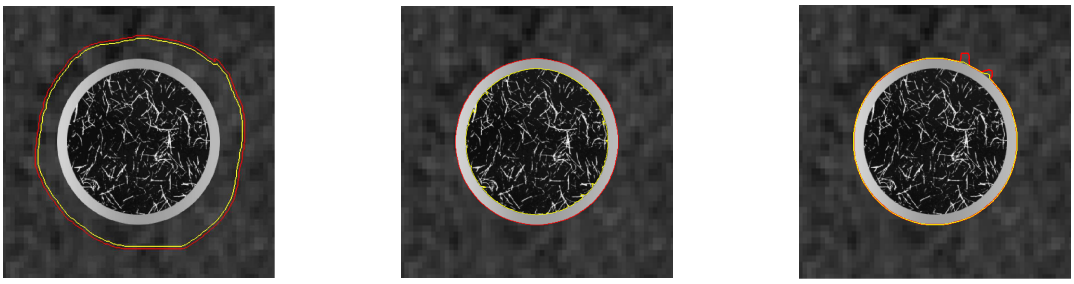

(d) Initialization **(e)** DAC **(f)** Lankton [113]

Figure 5.8: Results of the segmentation using the proposed DAC approach (b, e) and Lankton [113] (c, and f)on synthetic images created from Brodatz database and using the same contour initialization (a, and d)

DAC approach managed to segment accurately the different images despite the intensity overlaps between the different regions.

Segmentation of Medical images

Figure. 5.9 illustrates the segmentation result obtained by the application of the DAC and the Lankton methods on the HRpQCT and MRI image.

The DAC method produced the best result compared to Lankton's technique and in both cases the DAC managed to delineate accurately the cortical bone and the bladder wall.

To further validate the performance of DAC, similar to the previous method validation a database of 20 three dimensional HRpQCT images was used.

The average (DSC) metric of the DAC approach on the HRpQCT images is estimated to be 88.17% $\pm$ 2.09, and on MRI bladder wall is 98.2%.

As mentioned before, this is due to the shared energy of the two curves, along with the distance constraint between them.

Figure. 5.10 illustrates an example of the segmentation result obtained by the application of DAC and state of art techniques on an HRpQCT image of the radius. The different similarity measures computed are presented in Table 5.3. The DAC method

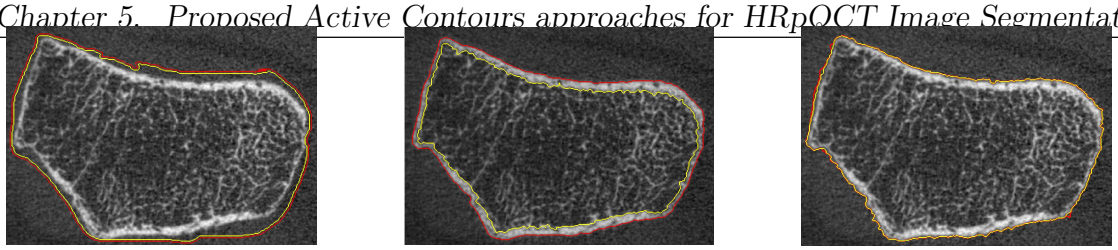

(a) Initialization **(b)** DAC **(c)** Lankton [113]

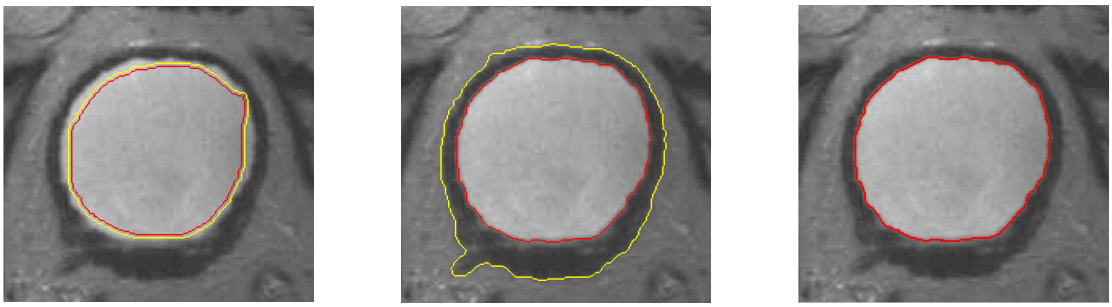

(d) Initialization **(e)** DAC **(f)** Lankton [113]

Figure 5.9: The segmentation result of the proposed DAC approach and Lankton [113] applied on radius bone HRpQCT image (first row) and bladder wall MRI (second row)

produced the best result using the different quality measures. The average (DSC) metric of the DAC approach is estimated to be 88.17% ± 2.09 compared to 83.65% ± 5.07 for BT and 81.12% ± 3.96 for DT. Results show that DAC managed to delineate the cortical compartment (Figure 5.10) compared to BT and DT who both produced an over or/and underestimation of the segmentation result compared to the GT.

In addition to DSC, the Hausdorff distance measure and the absolute volume error were used to further evaluate the 3D segmentation result. The Hausdorff distance (E_H) represents the maximum distance between the mesh of the GT and the mesh generated by the other approaches. Similar to DSC, DAC approach provided the best results with an error equal to 0.72 ± 0.08 mm. This demonstrates DAC efficiency and its capability of handling thin cortices, unlike DT who produced the highest error in all dataset (E_H = 1.88 ± 1.53) and cortical breaks can be seen (Figure 5.10). This is mainly due to the two empirically chosen thresholds of the approach.

Table 5.3: Comparison of the accuracy of the different methods versus the GT using different metrics

Parameters	**Units**	**DAC**	**BT**	**DT**
DSC	[%]	**88.17 ± 2.09**	83.65 ± 5.07	81.12 ± 3.96
E_H	[mm]	**0.72 ± 0.08**	0.95 ± 0.1	1.88 ± 1.53

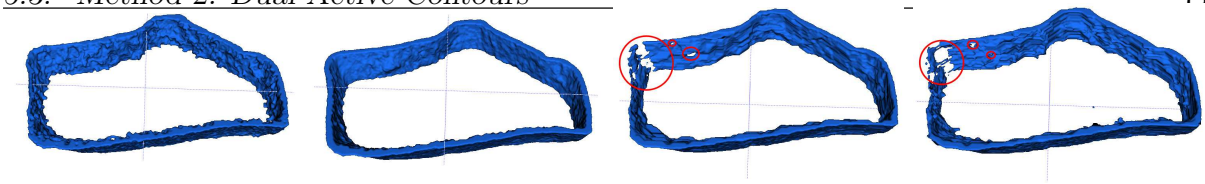

(a) GT **(b)** DAC **(c)** BT **(d)** DT

Figure 5.10: Comparison between the result of the manual segmentation (GT) and the different approaches in the case of radius. Cortical breaks are highlighted in red, they are apparent on all the approaches except in DAC.

Parameters effects

The proposed DAC approach depends on several parameters including the radius of the spheroid, the initialized distance between the two curves and the initialisation of the two contours. The effect of these parameters is studied in details in the following sections.

Radius sensitivity In the DAC approach, the radius r of the spheroid determines how local the information of the neighbouring pixels is incorporated into each point's movement. Therefore, for the outer contour, the choice of the radius should be selected based on the proximity of the contour to the object of interest along with the scale of this object. As stated in [113], larger radii are useful when attempting to segment large objects with less nearby clutter. This is the case in the HR-pQCT images. It is worth noting that the spheroid employed in our experiments has a pair of equal semi-axes (x and y) and a distinct third axis (z). First, we studied the effect of changing the radius along the (x and y-axis). Figure. 5.11 illustrates the effect of the selection of $R_{x,y}$ after 200 iterations. Using $R_{x,y} = 10$ pixels radius, the outer contour cannot detect a difference in the local neighbourhood. As a result, the contour cannot evolve and be attracted to the object, unlike the case of $R_{x,y} = 30$ pixels (Figure. 5.11).

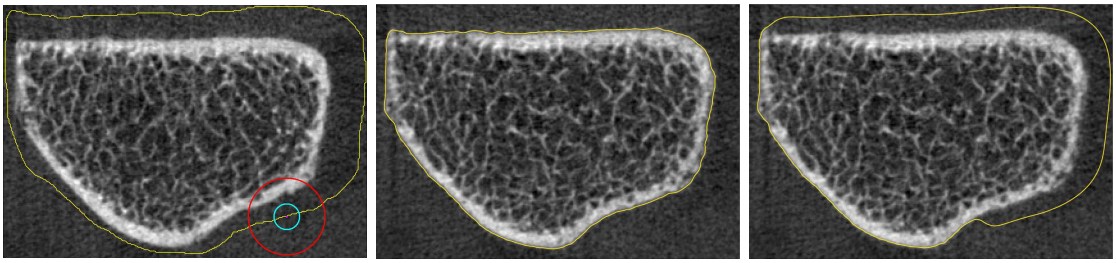

(a) Initial **(b)** 30 pixels **(c)** 10 pixels

Figure 5.11: The effect of the radius $R_{x,y}$ on the convergence of the outer curve, the 30 pixels radius is represented in red in (a) and the 10 pixels one is in blue. A good segmentation result is achieved using $R_{x,y} = 30$ pixels in (b). The non incorporation of the bone pixels in $R_{x,y} = 10$ pixels provides a bad segmentation result (c).

Furthermore, It can be noticed that in the $R_{x,y} = 30$ result, the change along the curve is smoother than the one of $R_{x,y} = 10$. However, this can lead to pixels misclassification and an over-estimation of the outside region of the cortical bone, as can be noticed in the boundaries of the contour for $R_{x,y} = 30$ (Figure. 5.11.b).

In the case of the inner curve, we also studied the effect of the different values of $R_{x,y}$. Figure. 5.12 illustrates the evolution of the inner contour using two different values of $R_{x,y}$ of the spheroid. In the case of $R_{x,y} = 30$ pixels, an over-estimation of the cortical compartment can be noticed, due to the big size of the radius. It is obvious that the larger the radius is, the more neighbouring pixels are incorporated into the movement of the contour. This explains the over-estimation in the case of $R_{x,y} = 30$ pixels unlike the $R_{x,y} = 10$ pixels segmentation result.

In the case of R_z, we noticed that the bigger the radius is, the more uniform the transition between the slices of the produced segmentation result is. The choice of R_z was fixed empirically to 5 pixels after a set of tests.

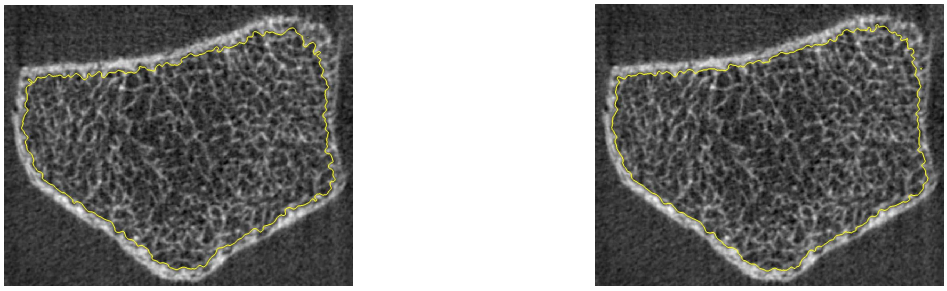

(a) R = 30 pixels **(b)** R = 10 pixels

Figure 5.12: The obtained inner contour using $R_{x,y} = 30$ pixels (a) and $R_{x,y} = 10$ pixels (b).

dual contour distance sensitivity In order to achieve a correct segmentation of the cortical bone, the initial distance between the two contours needs to be selected properly. The second contour must be inward and the distance between the two contours cannot be very big or the inner contour will start evolving in the trabecular bone region as seen in Figure. 5.13c. This distance cannot also be very small or the contour will not evolve properly with a risk of stagnation as can be seen in Figure. 5.13.

initialisation sensitivity Usually, local based methods have an essential drawback which is the process of contour initialisation as illustrated in Figure. 5.14. The contour

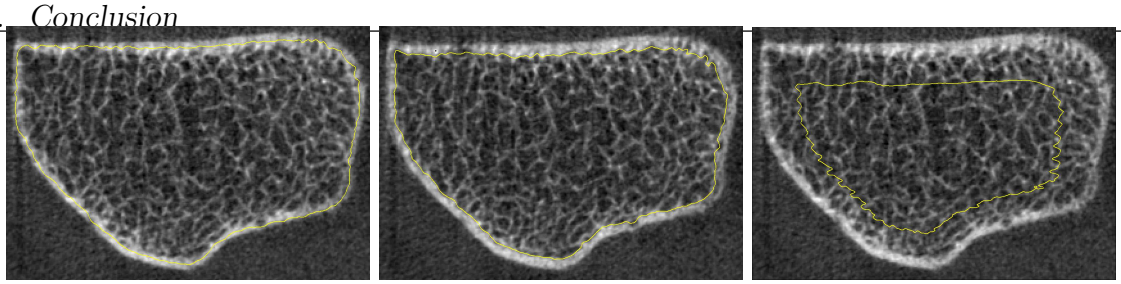

(a) D = -1 **(b)** D = -5 **(c)** D = -20

Figure 5.13: Initial contours distance effect

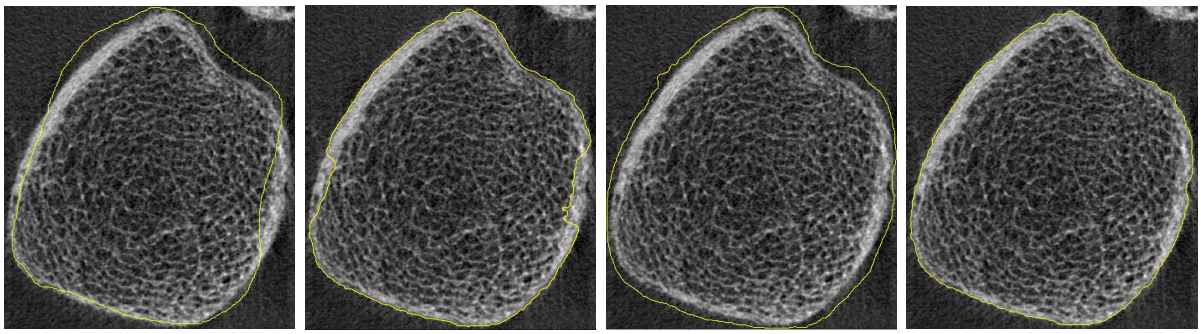

(a) Bad Initialisation **(b)** Bad result **(c)** Good Initialisation **(d)** Good result

Figure 5.14: The effect of bad and good initialisation result

of the proposed approach must be initialized relatively close to the object of interest. Because the form of the object of interest is known, the user intervention can be omitted, and hence, an automatic initialisation technique was proposed using the flowchart of Figure. 5.15.

DAC initialization

A specific initialization technique was proposed for the HRpQCT image. Since the bone shape is closed and round, a curve close to the object of interest can be identified automatically. The proposed pre-processing algorithm starts with the binarization of the image using a threshold of 40% of the highest gray level intensity in the image. Afterwards, a closing operation is used (dilation and erosion) with a structuring element (disk of 20 pixels) to fill in the trabecular bone. The last result serves as an initialisation mask for the DAC method as illustrated in Figure. 5.15.

5.4 Conclusion

To summarize, this chapter provided two distinct approaches proposed during this thesis. The first segmentation approach enables to segment accurately the HR-pQCT images in the ultra-distal sites. This was achieved using a new fuzzy energy active contours

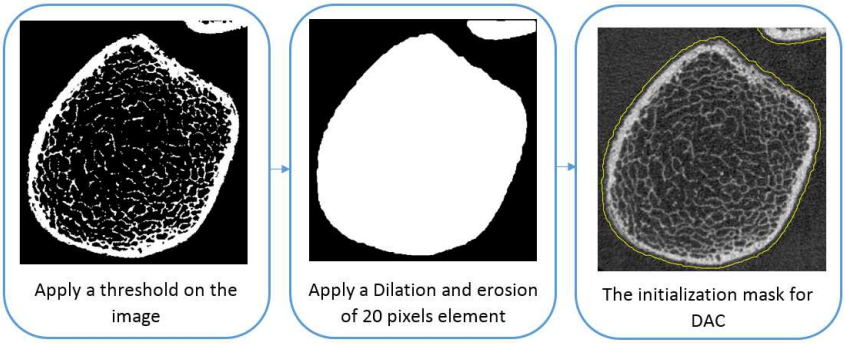

Figure 5.15: The proposed pre-processing algorithm to initialize DAC method.

approach. The latter is followed by a post-processing algorithm to mimic the clinicians behaviour for the separation between the two bones. The proposed algorithm provided accurate results and has the potential to provide more data due to its capability of handling the ultra-distal sites. However, this approach cannot quantify directly the porosity of the cortical bone, as the same post processing provided by [152] is needed. For that, we developed a new Dual Active Contours approach that can segment the cortical bone and its erosions automatically without any post-processing. The concept of DAC is based on evolving two contours in the image domain based on the energy between them, where they interact with each other to encapsulate the desired object.

After segmenting the cortical bone, an analysis of this compartement is needed to understand the effect of pathologies (osteoporosis) on it. The following chapter provides an overview of the different parameters extracted from the cortical bone and their relation with the fragility fractures.

Chapter 6

Osteoporotic Fractures Prediction

6.1 Introduction

The objective of this chapter is to illustrate the use of the segmentation result to quantify the different cortical parameters and thereby identify patients prone to fractures. The predictive capabilities of DAC approach were compared with the Xtreme Ct scanner segmentation method. The results achieved showed that the conventional analysis techniques of the cortical bone obscure potentially important regional variations in the cortical structure. Therefore, the cortical bone of the distal radius in this thesis is split into four regions to study the association between the local regional cortical parameters and fractures. The results prove that spatially resolved analysis is able to identify cortical sub-regions with increased fracture risk better than global analysis of the cortical bone.

6.2 Extracted parameters from the cortical bone

6.2.1 Global parameters

The standard method to quantitatively describe the bone architecture is the estimation of morphometric indices. These parameters represent the morphological and topological characteristics of the cortical bone and its porosity. The following Table 6.1 presents a detailed description of the parameters used in this study .

For the estimation of the mean cortical thickness, the following algorithm is applied to the binary result of the DAC method, which does not use the classical sphere technique, but, it produces the same results:

Table 6.1: Description of the Employed Cortical and Porosity Parameters

	Parameter (unit)	Description
Cortical	Ct.V (mm^3)	Cortical Volume = number of voxels of segmentation result including the pores × resolution ($0.082^3 mm^3$)
	Ct.Th (mm)	Average cortical thickness
	Ct.Ar (mm^2)	Cortical bone area = Ct.V ÷ (number of slices × slice thickness)
Porosity	Po. V (mm^3)	Porosity Volume = the void pixels in the segmentation result × resolution
	Ct.Po (%)	Cortical porosity = (Po.V ÷ Ct.V) × 100
	Po.N (n)	Pores Number
	Avg.Po.V (mm^3)	Average Pore Volume = Po.V ÷ Po.N
	Po.Dn (mm^{-3})	Pore density = Po.N ÷ Ct.V

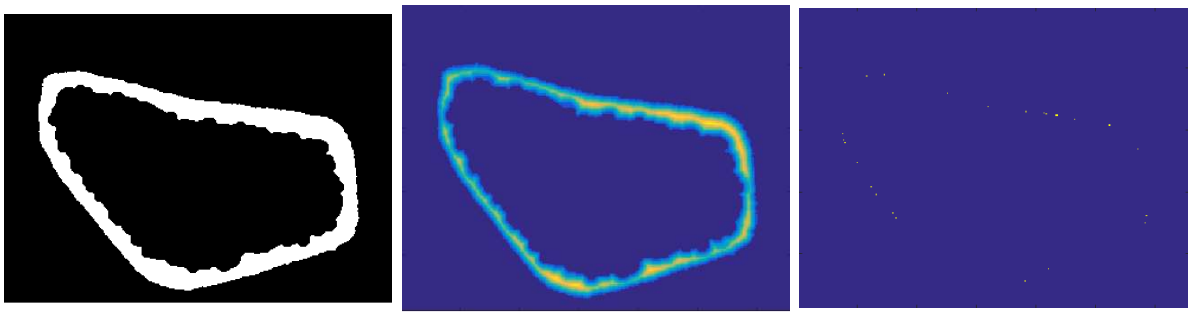

(a) **(b)** **(c)**

Figure 6.1: Illustration of the different steps to calculate the average cortical thickness, of a 2D distal radius slice (a), followed by the Euclidean distance transform (b), and the local maxima (c)

1. Compute the Euclidean distance transform of the binary image [171], so that all the background pixels are set to 0, and the foreground pixels are set to the distance from the background Figure 6.1b.

2. Find the local maxima in the distance transformed image. Assuming that there are spheres fitted in the binary image, the local maxima points represent the center of the spheres with maximum axis (Figure 6.1c).

3. Compute the average value of these points, which represents the mean cortical thickness.

6.2.2 Local parameters

As Kazakia *et. al* states in [172], while the importance of the cortical structure quantification is increasingly underscored by recent literature, the conventional analysis techniques obscure potentially important regional parameter variations. Therefore, re-

gional analysis has become recently an interesting field to understand and explore the anatomic distribution of geometric and microstructural features [172, 173, 174, 175, 59]. Analyses focusing on variation along the length of the bone have found considerable variation in geometry and microarchitecture measures [174, 176, 172]. Furthermore, in [176]a correlation between these measures and the mechanical competence of the bone illustrated. In site-specific analyses focused on the trabecular compartment, regional analysis has improved sensitivity to morphologic changes associated with age and gender differences [175] as well as those affected by antiresorptive therapy [175]. Regional analysis has also been used to detect a spatial association between cortical area and stress fracture prevalence at the tibia [173]. In this context, this work also studies the correlation between the regional cortical parameters and the bone fractures.

The first objective was therefore to partition all the images of the radius bone similarly To achieve that, an ellipse fitting technique on the image of the radius bone is applied. Then the two axis of the ellipse partition the image into four quadrants (Figure 6.2). The first step in the ellipse fitting technique is to extract the coordinates $(x_1, y_1), \ldots, (x_n, y_n)$ of all the n points of the outer contour of the cortical bone. Afterwards, the best fitted ellipse on these points is computed following the conic equation of an ellipse as follows:

$$\begin{aligned} ax^2 + bxy + cy^2 + dx + ey + f = 0 \\ AX + f = 0 \end{aligned} \tag{6.1}$$

where A is the vector of parameters to be estimated (a, b, c, d, e) along with f. X is the vector $(x^2, xy, y^2, x, y)^T$.

To fit an ellipse over the points $(x_1, y_1), \ldots, (x_n, y_n)$, we need to look for A that verifies:

$$\begin{bmatrix} AX_1 + f = 0 \\ AX_2 + f = 0 \\ \vdots \\ AX_N + f = 0 \end{bmatrix} \tag{6.2}$$

where $X_1, \ldots, X_n$ are the vector X for the points $(x_1, y_1), \ldots, (x_n, y_n)$, respectively. Using the least square technique, which considers that the best fit minimizes the sum of the

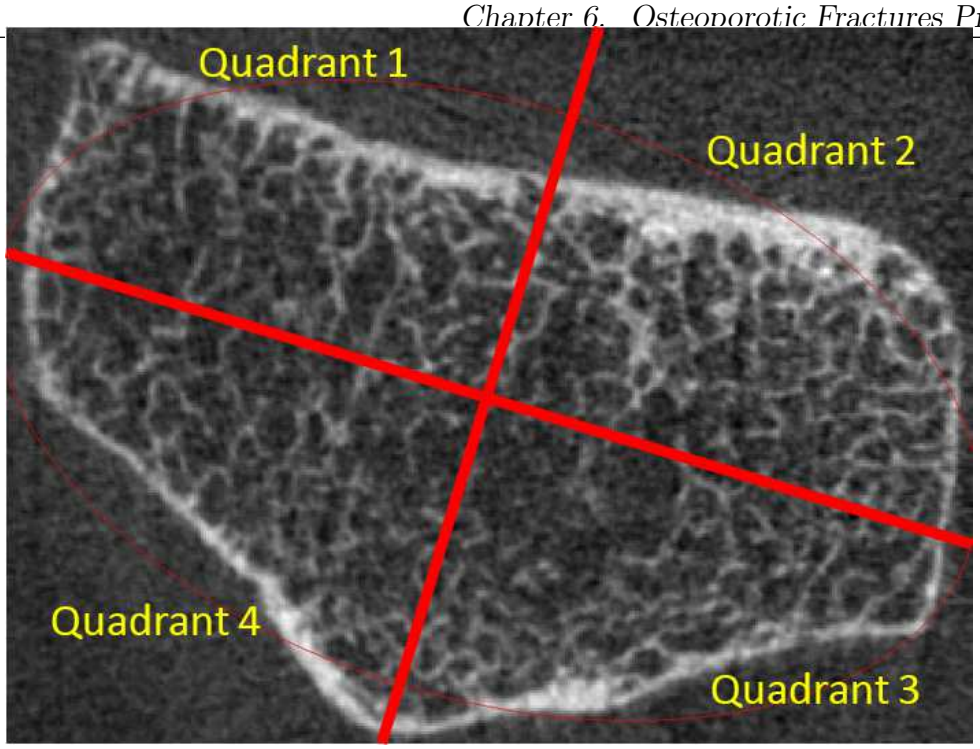

Figure 6.2: In red, the ellipse fitted to the ultra-distal scan of the radius bone using least squares method. The four quadrants used for the regional analysis are also illustrated.

squares of every single equation of the model is given by Equation (6.2). Considering $Y \equiv (X_1, X_2, \ldots, X_N)$, and $F \equiv (f, f, \ldots, f)$. The cost function to be minimized is then expressed as follows:

$$C \equiv (AY + F)^T \cdot (AY + F) \tag{6.3}$$

To estimate A that minimizes the cost function, the first derivative of Equation (6.3) is set to zero, A is then:

$$A = \frac{-f * \sum Y}{Y^T Y} \tag{6.4}$$

After the radius bone decomposition, the same parameters listed in the Chapter 6.2.1 are quantified for each quadrant, to serve as the local parameters of the radius bone.

6.3 Database

The subjects studied in this work come from the QUALYOR (Qualité Osseuse et Amélioration de la prédiction du risque fracturaire à LYon et ORléans) cohort described previously in Chapter 4.3. This is a prospective study of 1525 (1000 in Lyon, and 525 in Orléans) menopausal women aged ≥ 50, recruited between 2011 and 2012 with a 5 years follow-up for HRpQCT acquisition. The protocol was approved by a regional ethics

committee. Each subject was included in the study after signature of informed consent. Only the Orléans data were available during this thesis, with a limited number of fractured participants (31) along the follow up period. The Piala criterion for HRpQCT image quality was used [163] and then only 172 participants were selected where the acquired images were accurate with no motion and no ring artifacts. Over the 172 patients, 31 (18.12%) sustained one or more fracture during the in average 5-3 years follow-up period. Table 6.2 presents the baseline (clinical) characteristics of the 172 patients used in this study, where the clinical variables are presented as mean ± standard deviation.

Table 6.2: Baseline characteristics of the employed database

	Control (N=141)	**Fractured** (N=31)
Age (years)	69.63 ± 4.73	69.73 ± 6.42
Bone Mineral Index (BMI) (kg/m^2)	24.88 ± 4.04	24.56 ± 3.82
BMD (g/cm^2)	0.79 ± 0.08	0.77 ± 0.07

6.4 Statistical analysis

First, using the segmented database, the global cortical parameters are coupled with the clinical covariates (Age, BMI, menopause year, Hip BMD) to construct a feature vector. Then, to monitor the predictive capability of this vector of parameters, the logistic regression technique ([177]) is used with four distinct models.

1. **Model 1:** Clinical covariates (Age, BMI, Hip BMD and menopause year)
2. **Model 2:** Clinical covariates + Cortical parameters (Table 6.1)
3. **Model 3:** Clinical covariates + Porosity parameters (Table 6.1)
4. **Model 4:** Combination of all the above three models.

These models were used to test the effect of the clinical, cortical and porosity parameters individually and to identify the best set of parameters able on distinguishing between the two populations (controls and fractured). Each model was evaluated using the 10-fold cross-validation repeated 100 times in order to construct the Receiver Operating Characteristic (ROC) curves ([177]).

A comparison between the DAC parameters and the conventional technique of the Xtreme CT scanner is conducted to identify which method separates better the two populations. The area under the curve (AUC) from the ROC curves is used as performance criterion, in addition to the statistical classification rates such as: Accuracy, Sensitivity, Specificity, Positive Predictive Value (PPV), Negative Predictive Value (NPV), and Balanced Accuracy (BA). More details are provided in the Appendix A.

In the second experiment, we have realized a decomposition of each radius image of the database into four regions [175] using the ellipse fitting technique described in Chapter 6.2.2. The ROC curves and the classification rates are also used to evaluate the associations between the cortical bone parameters of each quadrant and the fractures.

Furthermore, the Cox Proportional Hazard (CPH) model developed by Cox [178] is used to evaluate the associations between each quadrant's parameters and the bone fractures. CPH is essentially a regression model commonly used in medical research for investigating the association between the survival time of patients and one or more predictor variables. The purpose of the CPH model is to evaluate simultaneously the effect of several factors on the survival. In other words, it allows us to examine how specific parameters influence the rate of a particular event happening (e.g. fracture) at a particular point in time. This rate is commonly referred as the Hazard Rate (HR) and is quantified for each parameter. HR above 1 indicates that a parameter (referred covariate) is positively associated with the event probability, and thus negatively associated with the length of survival. Three values are considered for the HR:

- HR = 1 : No effect on prognosis.
- HR < 1 : Reduction in hazard, meaning less risk of getting fracture is associated with the considered parameter.
- HR > 1 : Increase in hazard, meaning more risk of getting fracture is associated with the considered parameter.

Based on the CPH models, a composite variable was built, taking into account the age, BMI, and Hip BMD in combination with either cortical parameters or porosity ones.

All statistical analyzes were performed in R language (`https://www.r-project.org`, version 3.3.3), using the MASS packages (version 7.3 - for iterative optimization), Caret (version 6.0 - for cross-validation), pROC (version 1.10 - for the analysis of ROC

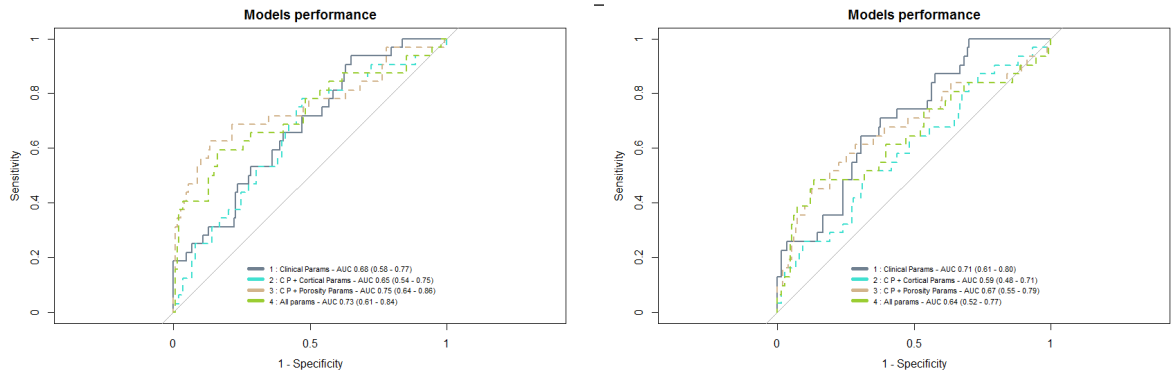

(a) **(b)**

Figure 6.3: ROC curves for a composite clinical variables, cortical parameters, porosity parameters, and all the previous models using (a) the DAC's segmentation result(b) Xtreme CT technique result

curves), and survival (version 2.41 - for the cox proportional hazard model). The documentation for these packages is available online (`https://cran.r-project.org/web/packages`)

6.5 Results

6.5.1 Fracture prediction using cortical global parameters

First, the database was segmented using the DAC and the Xtreme CT implemented method. Based on the segmentation results, the different parameters expressed in Chapter 6.2.1 are calculated in a global manner on each radius. Then, an evaluation of the outcome of each of the four models using both segmentations results is performed. Both techniques achieved the same conclusions, using the model 3 achieves better results compared to model 2, meaning that porosity parameters separate better than only cortical parameters. The separation between the fractured and the control patients using the model 2 and 3 was evaluated using the AUC. An increase of 10 % in the AUC value of the DAC approach (0.65 in model 2 to 0.75 in model 3), and an increase of 8% of the Xtreme CT (0.59 model 2 to 0.67 model 3) Figure 6.3.

Furthermore, Table 6.3 illustrates the performance of the two techniques using the model 4 which combines clinical, cortical and porosity parameters. Both techniques did not provide good performances on identifying the patients that are prone to experience fracture, with a sensitivity of 15.35% using DAC compared to 11.09% using Xtreme. The accuracy of the DAC method (82.05 %) is less than the one obtained from Xtreme CT (82.38%), which can be explained by the number of control patients that is superior than

the fractured ones. This can influence the accuracy result because, even if all the patients are classified as controls, the accuracy will remain high. Therefore, Balanced Accuracy (BA), which is equal to ((sensitivity+specificity)/2) was used to balance between the number of controls and fractured, and in this case the proposed approach (56,03%) exceeded Xtreme CT one (54,23%). However, it is obvious that no remarkable improvement is achieved between DAC and Xtreme CT, due to the very low sensitivity rate in both techniques.

Table 6.3: The Statistical Performance of DAC and Xtreme CT Segmentation results on the Predictions of Fractures

Method	Accuracy	Sensitivity	Specificity	PPV	NPV	BA
DAC	82.05	**15.35**	96.7	**50.63**	**83.86**	**56.03**
Xtreme CT	**82.38**	11.54	**96.9**	43.55	84.22	54.23

6.5.2 Fracture prediction using the local cortical parameters

After the radius bone decomposition into four quadrants, the cortical bone parameters are studied locally in each region. To test the associations between each part parameters with the incident fractures, we first used the ROC curves, and the CPH model explained in Appendix A. The performance of each quadrant is discussed in follows:

Quadrant 1

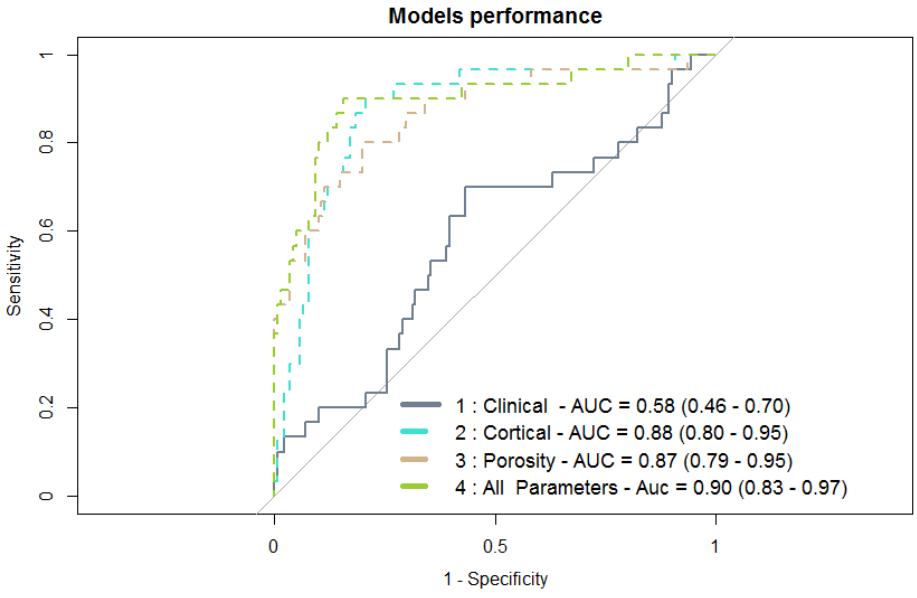

Figure 6.4: ROC curve for the "Quadrant 1"of the radius bone using the four models

Among the different quadrants, the first part (Figure 6.2), produced the best results with an AUC of 0.88 using the cortical parameters (model 2), 0.87 using the porosity parameters (model 3) and 0.90 using the model 4 (Figure 6.4). Compared to the global analysis, these results show that local bone observation achieve better associations with incident fractures. This can be related to the fact that this quadrant experience more remodeling than the other quadrants, which is yet to be anatomically proven. However, it is evident that different daily forces and activities influence the bone formation. Moreover, the results achieved (Figure 6.4) illustrate that cortical parameters slightly achieve better results than the porosity ones. To further exhibits the performance of this quadrant, Table 6.4 represent the statistical results, with a sensitivity of 59.53% and a balanced accuracy of 76.92% compared to global parameters with 15.35% for sensitivity and 56.03% for balanced accuracy.

Moreover, to identify the best parameters in the first quadrant, the CPH model is used. Table 6.5 represents the hazard ratio results of every parameter from the four quadrants. The base model was the clinical covariates (Age, BMI and Hip BMD), then we added individually each cortical and porosity parameter to evaluate its association with the fractures. If the HR > 1, this means that this parameter is a good fracture predictor. Three robust prediction values were noticed in the parameters CT.Ar1, Po.V1, and AvgPo.V1. The Ct.Ar1 in the fractured group decreased compared to healthy ones and the HR associated was (1.8; Confidence Interval (CI) of 1.5-2.2). An increase in the Po.V1 with (HR of 1.5; CI 1.2-1.8), and Avg.Po.V1 in the fractured group with (HR of 1.7; CI 1.4-2.1).

Quadrant 2

The same observations as the first quadrant were achieved in the second quadrant. AUC of 0.86 using the cortical parameters, 0.85 using the porosity parameters and 0.83 using the 4th model. Similar to Quadrant 1, compared to the global analysis, these results show that this part experience more noticeable changes compared to the cortical bone as a whole. Comparably good results were also achieved using the classification rates as can be seen in Table 6.4. However, using the CPH model none of the quadrant 2 parameters produced a robust HR (Table 6.5).

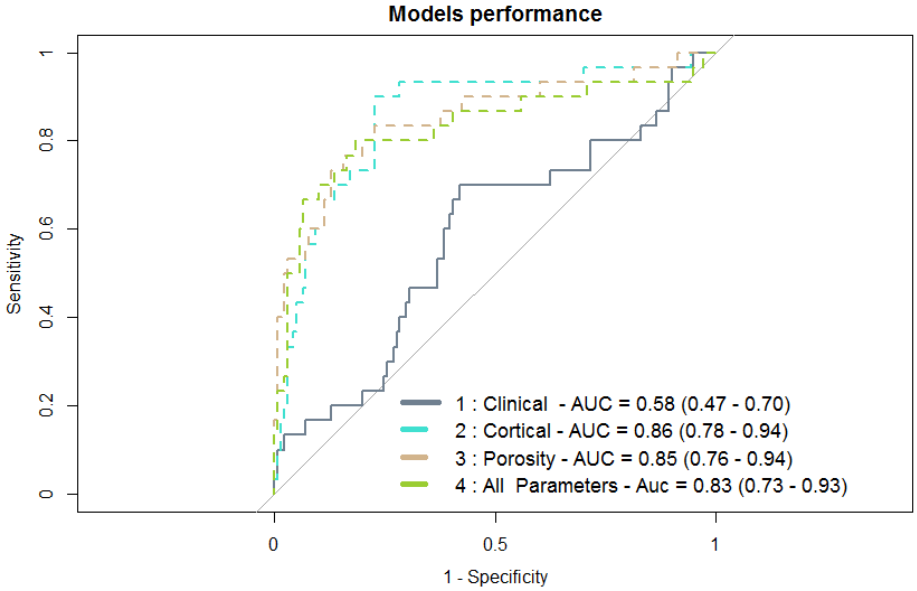

Figure 6.5: ROC of the "Quadrant 2 "parameters of the cortical bone of the radius

Table 6.4: The Statistical Classification Rates of the Local Cortical Parameters by Quadrant

Quadrant	Accuracy	Sensitivity	Specificity	PPV	NPV	BA
Part1	88.2	59.53	94.30	68.98	91.63	76.92
Part2	86.68	42.87	96.01	69.55	88.76	69.44
Part3	81.06	0.07	98.15	0.74	82.28	49.42
Part4	81.56	1.66	98.55	19.68	82.48	50.10

Quadrant 3

The parameters extracted from the quadrant 3, were not able to differentiate between the healthy and fractured participants. The statistical tests (Table 6.4) show that quadrant 3 could not predict fractures, with a sensitivity (0.07%) near to zero, which means that the majority of participants were identified as non prone to fractures. The same interpretation is reached using the CPH model (Table 6.5).

Quadrant 4

Similar to Quadrant 3, the Quadrant 4 was not able to differentiate between the healthy and prone to fractures group. The produced sensitivity 1.66 % effectively means that the parameters extracted from this quadrant are not good predictors for osteoporotic fractures with HR for all the parameters = 1 (Table 6.5).

Table 6.5: Association Between Multiple HR-pQCT Cortical Bone Variables and Fractures Using Cox Model

	Parameters	HR (95% CI for HR)
Global	Ct. Ar	1.1 (1-1.2)
	Ct. Th	1.1 (1-1.1)
	Ct. V	1 (1-1)
	Ct. Po	0.98 (0.67-1.4)
	Po. V	1 (0.96-1.1)
	Avg. Po. V	1.3 (0.97-1.8)
Quadrant 1	Ct. Ar 1	**1.8 (1.5-2.2)**
	Ct. Th 1	1 (1-1)
	Ct. V 1	1.1 (1-1.1)
	Ct. Po 1	1.1 (0.83-1.5)
	Po. V 1	**1.5 (1.2-1.8)**
	Avg. Po. V 1	**1.7 (1.4-2.1)**
Quadrant 2	Ct. Ar 2	1.3 (1.1-1.6)
	Ct. Th 2	1 (1-1)
	Ct. V 2	1 (1-1.1)
	Ct. Po 2	1 (0.78-1.3)
	Po. V 2	1.2 (0.97-1.4)
	Avg. Po. V 2	1.1 (0.98-1.3)
Quadrant 3	Ct. Ar 3	0.89 (0.73-1.1)
	Ct. Th 3	0.98 (0.95-1)
	Ct. V 3	0.99 (0.97-1)
	Ct. Po 3	0.83 (0.6-1.2)
	Po. V 3	0.83 (0.66-1)
	Avg. Po. V 3	0.79 (0.59-1)
Quadrant 4	Ct. Ar. 4	0.96 (0.8-1.2)
	Ct. Th 4	0.99 (0.96-1)
	Ct. V 4	1 (0.98-1)
	Ct. Po 4	0.77 (0.52-1.1)
	Po. V 4	0.8 (0.6-1.1)
	Avg. Po. V 4	0.63 (0.42-0.97)

6.6 Discussion

To our knowledge, this is the first study associating the regional cortical changes in radius with the osteoporotic fractures. As a conclusion from the local analysis of the cortical bone, we deduced that actually, the global cortical parameters obscure potentially important regional variations such as quadrants 1 and 2. Therefore, incorporating the global parameters of the cortical bone will use healthy portions of the bone that are not

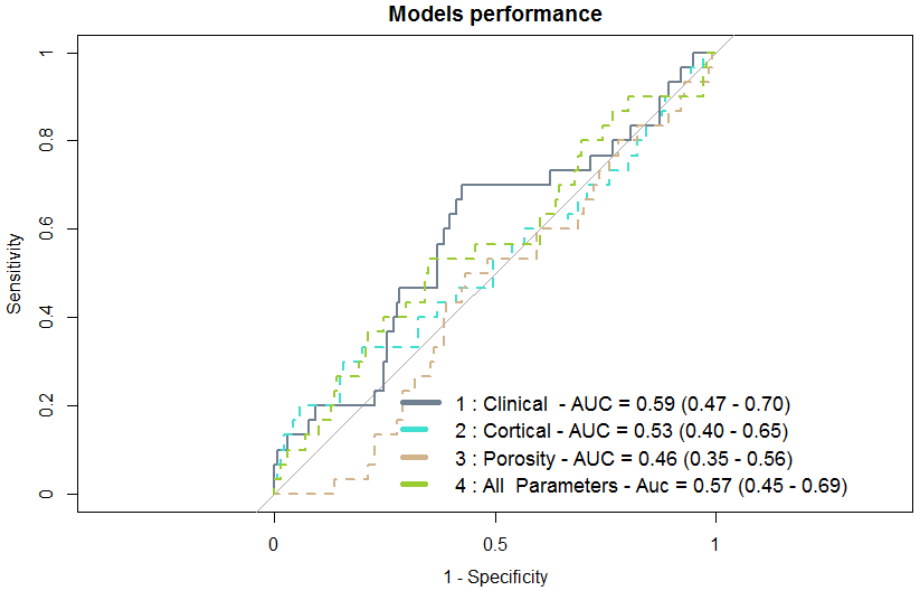

Figure 6.6: ROC curve of the "Quadrant 3"parameters of the cortical bone of radius using the four models

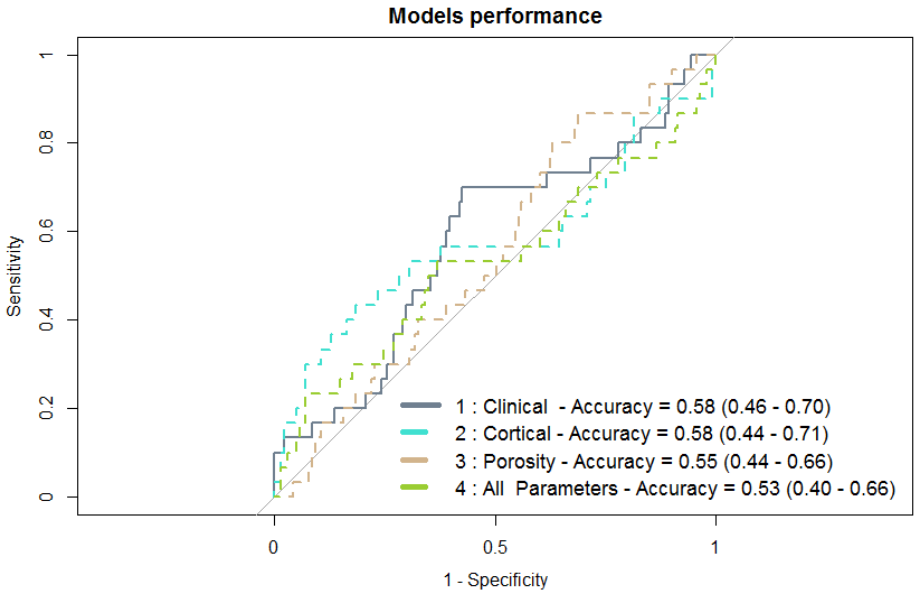

Figure 6.7: ROC curve of the "Quadrant 4"parameters of the cortical bone of the radius using the four models

prone to fractures, and hence, will bias the global results. For that reason, it is necessary to study the cortical bone locally instead of globally to construct a more robust predictive system of osteoporotic fractures.

Compared to [172], which evaluated the Age and gender related differences in the geometry and microstructure of the cortical bone subregions, significant regional variations were noticed in the cortical parameters in the radius as well as in the tibia. At both sites, Ct.Po displayed the greatest regional variations. Comparing women to men, differences in Ct.Po were most pronounced in the quadrant 1 of the radius (36% lower in women). As

for the comparison between the elderly to young women, differences in Ct.Po were most pronounced in the quadrant 1 and 2 of the radius (328% higher in the elderly women). Since, the oldest we get, the higher the probability of fracture we have. This result corroborates our findings, that Quadrant 1 and 2 are the most affected by the aging and more prone to fractures. These results suggest that regional analysis may be important in studies of disease and therapeutic effects. Particularly where microstructural parameters based on global analyses have thus far failed to identify a response in bone quality.

One limitation faces the proposed study is the lack of the anatomical explanation of the specific quadrants affections. As stated by [172, 173], the biomechanical parameters describing the load and the stress distribution all over the bone explains further how each bone region changes according to the mechanical forces applied on it. This can help explaining the results difference between the quadrants.

6.7 Conclusion

This cross-sectional study presents a novel investigation of the bone quality and the osteoporotic fractures using three-dimensional HR-pQCT, as well as a customized regional analysis method to examine spatial variations by quadrants. When analyzing the bone as a whole, cortical/prorosity parameters outcomes were not different between the different groups (controls and fractured). However, the regional analysis revealed trends of a thinner cortex, augmentation of porosity volume and a significantly smaller cortical area in the first quadrant of the fractured group. The anatomical interpretation of the finding is yet to be justified. However, these data suggest that there are significant differences in both the cortical, and porosity parameters between the control and fractured groups and that the differences are mostly localized in the quadrants 1 and 2 (Figure 6.2).

Conclusion

This work presents the problem of the HRpQCT image segmentation for the prediction of osteoporotic fractures. The aim of this thesis was to determine whether the morphological parameters of the cortical bone extracted from HRpQCT images could lead to a better identification of the participants that will experience fractures. The analysis of the cortical bone and the extraction of its morphological parameters cannot be accomplished until a correct segmentation of the latter is achieved. Therefore, our main objective was to propose an automatic and an accurate cortical bone segmentation of HRpQCT images.

Currently, in Xteme CT scanner, HRpQCT cortical bone segmentation is based on the semi-manual delineation of the periosteal surface, while the endosteal surface is extracted using Burghardt technique [59]. Two approaches were proposed to solve the problem of automatic and accurate segmentation of the cortical bone. The first approach segments the ultra-distal sites images based on a new fuzzy energy active contours approach. The approach does not use the intensity of the pixel to separate between inside and outside the contours, instead it uses a fuzzy membership function which describes the belonging of each pixel to each region. This approach proved its applicability in handling the image inhomogeneity in the ultra distal sites. However, another post processing algoithm is needed to extract the pores of the cortical bone.

On the other hand, the second approach can segment the cortical bone and its porosity. A new concept was introduced based on evolving two contours in the image domain based on the local energy between them, where they can interact with each other to encapsulate the desired object. This hypothesis can furthermore be used to improve the segmentation result of objects with difficult structures. Many conclusions can be drawn from the experiments of the approach DAC. First, an application of Dual Active Contour approach on synthetic data created using the Brodatz database illustrated the applicability of the latter. Moreover, to further validate the performance of DAC, medical

images such as HRpQCT images and MRI bladder wall were used.

In DAC, the idea of moving the second contour to ensure that the region between the two contours is homogeneous will never produce cortical breaks unlike the state of the art. Finally, due to the localized energy of the proposed technique, user intervention is needed to initialize the contour close to the object of interest. In this study, in the case of HRpQCT images, we have proposed a novel pre-processing algorithm that can provide an automatic initial contour based on a thresholding technique and closing operations. Furthermore, the time complexity was reduced using the FFT transform to simplify the convolution complexity. In spite of that, the computation cost of the approach in Matlab remains high in dealing with huge 3D volumes of data.

Using the DAC segmentation method on the QUALYOR database, allowed us to analyze and quantify the different cortical parameters such as: Cortical thickness, Cortical porosity, porosity volume, etc. Different experiments enlightened us the role of the cortical bone. When analyzing the bone as a whole, cortical/porosity parameters outcomes were not different between groups. However, the regional analysis revealed trends of a thinner cortex, augmentation of porosity volume and a significantly smaller cortical area in certain quadrants of the fractured group. The anatomical interpretation of the finding is yet to be justified. However, on the whole, these data suggest that there are significant differences in both the cortical, and porosity parameters between the control and fractured groups and that the differences are mostly localized in some quadrants.

Future studies will focus on several areas:

- The combination of the fuzzy logic introduced in the first approach to the DAC energy can be studied to further enhance the result of segmentation
- For the time complexity of DAC, a current work is undergoing to parallelize the two contours interaction, where each point of the inner contour will take into account only the neighboring points in the outer contour. Thereby, points all over the inner contour can start moving while the outer one hasn't converged yet
- Another interesting idea is to add a global fitting term to the DAC energy. This could help resolve the initialization problem and the execution time.
- A specific study could focus on understanding the mechanical behavior of the bone

along the different parts using Finite Element Analysis (FEA). This will help comprehend the stress and stiffness on each of them, which can explain the differences between the quadrant results.

- A complete study on the QUALYOR database. Recently we have retrieved the whole database in the two sites of Orleans and Lyon. More than 100 participants have endured fracture along the follow up study. Therefore, the number of fractured patients will no long be crippling as it was in the actual study. It remains to remake the statistical study with the different quadrants to consolidate the obtained results.

Appendix A

Statistic Tools used for Predictions

A.1 Logistic regression

Logistic regression is a method of data analysis widely used in the medical field to find characteristics specific to a pathology. This model of analysis is also used in other fields such as insurance or econometrics for the explanation of discrete variables. This method was proposed in 1958 by Cox [177].

As the name implies, it is a binomial regression model used to estimate the probability of a binary response in function of a set of independent qualitative or quantitative variables. In other words, we measure the association of a qualitative variable with two levels, called dependent, with one or more explanatory variables via a logistic function.

Let Y be the variable to be predicted and $X = (X1; \ldots; Xp)$ are the set of predictive variables. We note Y_j the observations of Y for $j = 1, \ldots, n$ and $X_{i,j}$ the observations of X for i=$1, \ldots, p$

The logit function of probability $Pr(1|X)$ is given by:

$$ln(\frac{Pr(1|X)}{1 - Pr(1|X)}) = \beta_0 + \beta_1 x1 + \cdots + \beta_j x_j$$

The logistic model is then written as follows:

$$ln(\frac{Pr(Y_j = 1|Xij)}{Pr(1 - Y_j = 1|X_{ij})}) = \beta_0 + \sum_{i=1}^{p} \beta_1 X_{ij}$$

The parameters β of the model are then estimated by maximizing the likelihood L

given by:

$$L(\beta) = \prod_{j=1}^{n} Pr(Y_j = 1|X_{ij})^{Y_j} \times Pr(Y_j = 0|X_{ij})$$
$$= \prod_{j=1}^{n} Pr(Y_j = 1|X_{ij})^{Y_j} \times [1 - Pr(Y_j = 1|X_{ij})Y_j]$$

The maximum likelihood estimation is done by an iterative optimization algorithm based on the Newton-Raphson method:

$$\beta^{i+1} = \beta^i - \left(\frac{\partial^2 L}{\partial\beta\partial\beta'}\right)^{-1} \times \frac{\partial L}{\partial\beta} \tag{A.1}$$

Each iteration refining the values of β, until the convergence towards the optimal values, is translated by a stability of the parameters β from one iteration to the other.

A.2 ROC Curves

ROC curves, also called performance characteristic curves or sensitivity/ specificity curves, are visual indicators of the performance of a binary classifier. To construct these curves, the sensitivity (Se) of a classifier against its specificity (Sp) is plotted for different thresholds of probability. Sensitivity is the probability of obtaining a positive prediction for a positive observation. Specificity measures the probability of obtaining a negative prediction for a negative observation.

In the case of a logistic regression, the probability $Pr(Yj = 1|X_{ij}) \in [0; 1]$ is computed for each sample. By varying the decision threshold $\sigma \in [0; 1]$, different confusion matrices tables are constructed (Table A.1).

Table A.1: Confusion Matrix

		Reference	
		Case	**Control**
Predicted	**Case**	TP	FP
	Control	FN	TN

From these confusion matrix, the sensitivity, and specificity associated with this threshold σ are calculated according to:

$$Se(\sigma) = \frac{TP}{TP + FN} \qquad SP(\sigma) = \frac{TN}{TN + FP}$$

with :

- TP: True Positive, the number of true observations classified true.
- FN: False Negatives, the number of true observations classified as false.
- TN: True Negative, the number of false observations classified false.
- FP: False Positive, the number of false observations classified as true.

Different parameters can be computed from the confusion matrix, using the following formulas :

$$Sensitivity = \frac{TP}{TP + FN}$$
$$Specificity = \frac{TN}{TN + FP}$$
$$Prevalence = \frac{(TP + FN)}{(TP + FP + TN + FN)}$$
$$PPV = \frac{(sensitivity \times prevalence)}{((sensitivity \times prevalence) + ((1 - specificity) \times (1 - prevalence)))}$$
$$NPV = \frac{(specificity \times (1 - prevalence))}{(((1 - sensitivity) \times prevalence) + ((specificity) \times (1 - prevalence)))}$$
$$BalancedAccuracy = \frac{(sensitivity + specificity)}{2}$$

The ROC curve is a fundamental tool for diagnostic test evaluation. In a ROC curve the true positive rate (Sensitivity) is plotted in function of the false positive rate (100-Specificity) for different cut-off points of a parameter. Each point on the ROC curve represents a sensitivity/specificity pair corresponding to a particular decision threshold. A test with perfect discrimination (no overlap in the two distributions) has a ROC curve that passes through the upper left corner (100% sensitivity, 100% specificity). Therefore the closer the ROC curve is to the upper left corner, the higher the overall accuracy of the test.

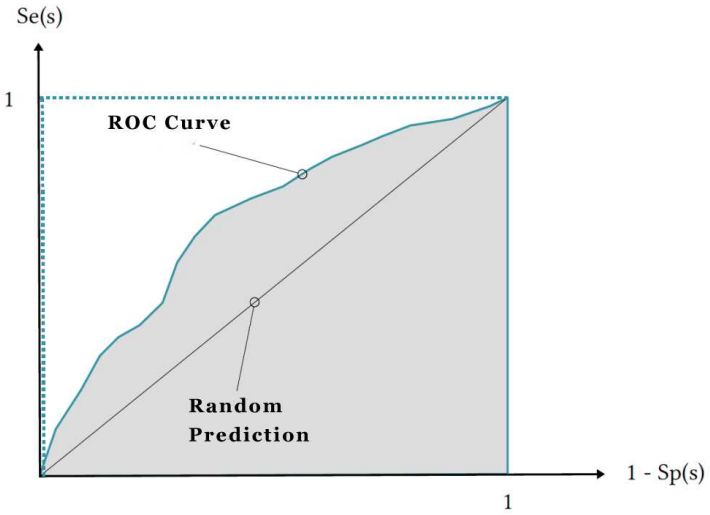

Figure A.1: Example of ROC curve. The blue dotted line corresponds to the ideal curve with sensitivity and specificity equal to 1. The gray area symbolizes the area under the curve (AUC).

From this curve, the area under the curve (AUC) is calculated as a performance indicator:

$$AUC = \int_0^1 Se(\sigma)(1 - Sp(\sigma))$$

The AUC is therefore between 0 and 1. A random prediction will have an AUC of 0.5, while a perfect classifier will have an AUC of 1. It is commonly assumed that a model is acceptable if it produces an AUC > 0.7.

A.3 Cox proportional hazard model

The Cox proportional-hazards model (Cox, 1972) [178] is essentially a regression model commonly used statistical in medical research for investigating the association between the survival time of patients and one or more predictor variables.

The purpose of the model is to evaluate simultaneously the effect of several factors on survival. In other words, it allows us to examine how specified factors influence the rate of a particular event happening (e.g., infection, death) at a particular point in time. This rate is commonly referred as the hazard rate. Predictor variables (or factors) are usually termed covariates in the survival-analysis literature.

The Cox model is expressed by the hazard function denoted by h(t). Briefly, the hazard function can be interpreted as the risk of dying at time t. It can be estimated as

follow:

$$h(t) = h_0(t) \times exp(b_1x_1 + b_2x_2 + ... + b_px_p)$$

where,

- t represents the survival time
- h(t) is the hazard function determined by a set of p covariates $(x_1, x_2, \ldots, x_p)$
- the coefficients $(b_1, b2, ..., b_p)$ measure the impact (i.e., the effect size) of covariates.
- the term h_0 is called the baseline hazard. It corresponds to the value of the hazard if all the x_i are equal to zero (the quantity exp(0) equals 1). The 't' in h(t) reminds us that the hazard may vary over time.

The Cox model can be written as a multiple linear regression of the logarithm of the hazard on the variables x_i, with the baseline hazard being an 'intercept' term that varies with time.

The quantities $exp(b_i)$ are called hazard ratios (HR). A value of b_i greater than zero, or equivalently a hazard ratio greater than one, indicates that as the value of the i^th covariate increases, the event hazard increases and thus the length of survival decreases.

Put another way, a hazard ratio above 1 indicates a covariate that is positively associated with the event probability, and thus negatively associated with the length of survival.

In summary,

- HR = 1: No effect
- HR < 1: Reduction in the hazard
- HR > 1: Increase in Hazard

Bibliography

[1] O. of the Surgeon General, "The Basics of Bone in Health and Disease: A report of the surgeon general.," *US Department of Health and Human Services. Rockville, Maryland, USA*, p. 404, 2004.

[2] E. F. Eriksen, D. W. Axelrod, and F. Melsen, "Bone histomorphometry," *New York: Raven Press*, 1994.

[3] U. Kini and B. N. Nandeesh, "Physiology of Bone Formation, Remodeling, and Metabolism," in *Radionuclide and Hybrid Bone Imaging*, pp. 29–57, Berlin, Heidelberg: Springer Berlin Heidelberg, 2012.

[4] C. H. Turner, "Three rules for bone adaptation to mechanical stimuli," *Bone*, vol. 23, no. 5, pp. 399–407, 1998.

[5] A. Bruzzaniti and R. Baron, "Molecular regulation of osteoclast activity," vol. 7, no. 1-2, pp. 123–139, 2006.

[6] G. D. Roodman, "Regulation of osteoclast differentiation," in *Annals of the New York Academy of Sciences*, vol. 1068, pp. 100–109, Blackwell Publishing Inc, apr 2006.

[7] *NIH Consensus Development Panel on Osteoporosis Prevention, Diagnosis, and Therapy.*, vol. 285. feb 2001.

[8] E. Seeman, "Chapter 1 – Modeling and Remodeling: The Cellular Machinery Responsible for the Gain and Loss of Bone's Material and Structural Strength," in *Principles of Bone Biology*, pp. 1–28, 2008.

[9] F. ALBRIGHT, P. H. SMITH, and A. M. RICHARDSON, "POSTMENOPAUSAL OSTEOPOROSIS," *Journal of the American Medical Association*, vol. 116, no. 22, p. 2465, 1941.

[10] R. B. Mazess, "On aging bone loss.," *Clinical orthopaedics and related research*, pp. 239–52, may 1982.

[11] J. A. Kanis, O. Johnell, A. Oden, C. De Laet, A. Dawson, and B. Jonsson, "Ten Year Probabilities of Osteoporotic Fractures According to BMD and Diagnostic Thresholds," *Osteoporosis International*, vol. 12, pp. 989–995, dec 2001.

[12] R. M. Zebaze, A. Ghasem-Zadeh, A. Bohte, S. Iuliano-Burns, M. Mirams, R. I. Price, E. J. Mackie, and E. Seeman, "Intracortical remodelling and porosity in the distal radius and post-mortem femurs of women: a cross-sectional study," *The Lancet*, vol. 375, pp. 1729–1736, may 2010.

[13] B. L. Riggs, H. W. Wahner, W. L. Dunn, R. B. Mazess, K. P. Offord, and L. J. Melton, "Differential changes in bone mineral density of the appendicular and axial skeleton with aging. Relationship to spinal osteoporosis," *Journal of Clinical Investigation*, vol. 67, pp. 328–335, feb 1981.

[14] H. K. Genant, C. Cooper, G. Poor, I. Reid, G. Ehrlich, J. Kanis, B. E. C. Nordin, E. Barrett-Connor, D. Black, J. P. Bonjour, B. Dawson-Hughes, P. D. Delmas, J. Dequeker, S. R. Eis, C. Gennari, O. Johnell, J. Johnston C.C., E. M. C. Lau, U. A. Liberman, R. Lindsay, T. J. Martin, B. Masri, C. A. Mautalen, P. J. Meunier, P. D. Miller, A. Mithal, H. Morii, S. Papapoulos, A. Woolf, W. Yu, and N. Khaltaev, "Interim report and recommendations of the World Health Organization Task-Force for Osteoporosis," *Osteoporosis International*, vol. 10, no. 4, pp. 259–264, 1999.

[15] "International Osteoporosis Foundation, Facts and statistics about osteoporosis and its impact." `https://www.iofbonehealth.org/facts-statistics`.

[16] A. Svedbom, E. Hernlund, M. Ivergård, J. Compston, C. Cooper, J. Stenmark, E. V. McCloskey, B. Jönsson, and J. A. Kanis, "Osteoporosis in the European Union: A compendium of country-specific reports," *Archives of Osteoporosis*, vol. 8, p. 137, dec 2013.

[17] C. L. Leibson, A. N. A. Tosteson, S. E. Gabriel, J. E. Ransom, and L. J. Melton, "Mortality, disability, and nursing home use for persons with and without hip fracture: A population-based study," *Journal of the American Geriatrics Society*, vol. 50, pp. 1644–1650, oct 2002.

[18] L. J. Melton, E. J. Atkinson, C. Cooper, W. M. O'Fallon, and B. L. Riggs, "Vertebral fractures predict subsequent fractures," *Osteoporosis International*, vol. 10, no. 3, pp. 214–221, 1999.

[19] B. L. Riggs, S. Khosla, and L. J. Melton, "A unitary model for involutional osteoporosis: estrogen deficiency causes both type I and type II osteoporosis in postmenopausal women and contributes to bone loss in aging men.," *Journal of bone and mineral*, vol. 13, pp. 763–73, may 1998.

[20] S. C. Manolagas, "Birth and death of bone cells: basic regulatory mechanisms and implications for the pathogenesis and treatment of osteoporosis.," *Endocrine reviews*, vol. 21, pp. 115–37, apr 2000.

[21] D. J. Torgerson, M. K. Campbell, R. E. Thomas, and D. M. Reid, "Prediction of perimenopausal fractures by bone mineral density and other risk factors.," *Journal of bone and mineral research : the official journal of the American Society for Bone and Mineral Research*, vol. 11, pp. 293–7, dec 1996.

[22] F. Cosman, S. J. de Beur, M. S. LeBoff, E. M. Lewiecki, B. Tanner, S. Randall, and R. Lindsay, "Clinician's Guide to Prevention and Treatment of Osteoporosis," *Osteoporosis International*, vol. 25, pp. 2359–2381, oct 2014.

[23] E. Sornay-Rendu, F. Munoz, P. Garnero, F. Duboeuf, and P. D. Delmas, "Identification of Osteopenic Women at High Risk of Fracture: The OFELY Study," *J Bone Miner Res*, vol. 20, pp. 1813–1819, jun 2005.

[24] J. A. Kanis, E. V. McCloskey, H. Johansson, C. Cooper, R. Rizzoli, and J. Y. Reginster, "European guidance for the diagnosis and management of osteoporosis in postmenopausal women," *Osteoporosis International*, vol. 24, pp. 23–57, jan 2013.

[25] B. L. Riggs and L. J. Melton, "The worldwide problem of osteoporosis: insights afforded by epidemiology," *Bone*, vol. 17, no. 5 Suppl, pp. S505–S511, 1995.

[26] R. D. Jackson and W. J. Mysiw, "Insights into the epidemiology of postmenopausal osteoporosis: the Women's Health Initiative," *Seminars in Reproductive Medicine*, vol. 32, no. 6, pp. 454–462, 2014.

[27] T. M. Link, "Osteoporosis Imaging: State of the Art and Advanced Imaging," *Radiology*, vol. 263, pp. 3–17, apr 2012.

[28] D. M. Black, M. P. Kelly, H. K. Genant, L. Palermo, R. Eastell, C. Bucci-Rechtweg, J. Cauley, P. C. Leung, S. Boonen, A. Santora, A. de Papp, and D. C. Bauer, "Bisphosphonates and Fractures of the Subtrochanteric or Diaphyseal Femur," *New England Journal of Medicine*, vol. 362, pp. 1761–1771, may 2010.

[29] E. S. Siris, Y.-T. Chen, T. A. Abbott, E. Barrett-Connor, P. D. Miller, L. E. Wehren, and M. L. Berger, "Bone Mineral Density Thresholds for Pharmacological Intervention to Prevent Fractures," *Archives of Internal Medicine*, vol. 164, p. 1108, may 2004.

[30] S. C. E. Schuit, M. van der Klift, A. E. A. M. Weel, C. E. D. H. de Laet, H. Burger, E. Seeman, A. Hofman, A. G. Uitterlinden, J. P. T. M. van Leeuwen, and H. A. P. Pols, "Fracture incidence and association with bone mineral density in elderly men and women: the Rotterdam Study.," *Bone*, vol. 34, pp. 195–202, jan 2004.

[31] M. L. Bouxsein, "Bone quality: where do we go from here?," *Osteoporosis International*, vol. 14, pp. 118–127, sep 2003.

[32] C. H. TURNER, "Bone Strength: Current Concepts," *Annals of the New York Academy of Sciences*, vol. 1068, pp. 429–446, apr 2006.

[33] J. E. Adams, "Advances in bone imaging for osteoporosis," *Nature Reviews Endocrinology*, vol. 9, pp. 28–42, dec 2012.

[34] A. Rosholm, L. Hyldstrup, L. B?ksgaard, M. Grunkin, and H. H. Thodberg, "Estimation of Bone Mineral Density by Digital X-ray Radiogrammetry: Theoretical Background and Clinical Testing," *Osteoporosis International*, vol. 12, pp. 961–969, nov 2001.

[35] J. T. Jorgensen, P. B. Andersen, A. Rosholm, and N. H. Bjarnason, "Digital X-ray radiogrammetry: a new appendicular bone densitometric method with high precision," *Clinical Physiology*, vol. 20, pp. 330–335, sep 2000.

[36] A. M. Laval-Jeantet, C. Bergot, R. Carroll, and F. Garcia-Schaefer, "Cortical bone senescence and mineral bone density of the humerus.," *Calcified tissue international*, vol. 35, pp. 268–72, may 1983.

[37] M. L. Bouxsein, L. Palermo, C. Yeung, and D. M. Black, "Digital X-ray Radiogrammetry Predicts Hip, Wrist and Vertebral Fracture Risk in Elderly Women: A Prospective Analysis from the Study of Osteoporotic Fractures," *Osteoporosis International*, vol. 13, pp. 358–365, may 2002.

[38] P. Bach-Mortensen, L. Hyldstrup, M. Appleyard, K. Hinds?, P. Gebuhr, and S. Sonne-Holm, "Digital X-Ray Radiogrammetry Identifies Women at Risk of Osteoporotic Fracture: Results from a Prospective Study," *Calcified Tissue International*, vol. 79, pp. 1–6, jul 2006.

[39] J. Kälvesten, L.-Y. Lui, T. Brismar, and S. Cummings, "Digital X-ray radiogrammetry in the study of osteoporotic fractures: Comparison to dual energy X-ray absorptiometry and FRAX," *Bone*, vol. 86, pp. 30–35, may 2016.

[40] G. M. Blake and I. Fogelman, "The clinical role of dual energy X-ray absorptiometry," *European Journal of Radiology*, vol. 71, pp. 406–414, sep 2009.

[41] E. M. Lewiecki and J. L. C. Borges, "Bone density testing in clinical practice.," *Arquivos brasileiros de endocrinologia e metabologia*, vol. 50, pp. 586–95, aug 2006.

[42] J. A. Kanis and C. C. Glüer, "An update on the diagnosis and assessment of osteoporosis with densitometry. Committee of Scientific Advisors, International Osteoporosis Foundation.," *Osteoporosis international : a journal established as result of cooperation between the European Foundation for Osteoporosis and the National Osteoporosis Foundation of the USA*, vol. 11, no. 3, pp. 192–202, 2000.

[43] T. E. Dufresne, P. A. Chmielewski, M. D. Manhart, T. D. Johnson, and B. Borah, "Risedronate Preserves Bone Architecture in Early Postmenopausal Women In 1 Year as Measured by Three-Dimensional Microcomputed Tomography," *Calcified Tissue International*, vol. 73, pp. 423–432, oct 2003.

[44] N. B. Watts, E. M. Lewiecki, P. D. Miller, and S. Baim, "National Osteoporosis Foundation 2008 Clinician's Guide to Prevention and Treatment of Osteoporosis and the World Health Organization Fracture Risk Assessment Tool (FRAX): What They Mean to the Bone Densitometrist and Bone Technologist," *Journal of Clinical Densitometry*, vol. 11, pp. 473–477, oct 2008.

[45] A. Unnanuntana, B. P. Gladnick, E. Donnelly, and J. M. Lane, "The assessment of fracture risk.," *The Journal of bone and joint surgery. American volume*, vol. 92, pp. 743–53, mar 2010.

[46] W. Yu, C. C. Glüer, S. Grampp, M. Jergas, T. Fuerst, C. Y. Wu, Y. Lu, B. Fan, and H. K. Genant, "Spinal bone mineral assessment in postmenopausal women: a comparison between dual X-ray absorptiometry and quantitative computed tomography.," *Osteoporosis international : a journal established as result of cooperation between the European Foundation for Osteoporosis and the National Osteoporosis Foundation of the USA*, vol. 5, no. 6, pp. 433–9, 1995.

[47] C. Bergot, A. M. Laval-Jeantet, K. Hutchinson, I. Dautraix, F. Caulin, and H. K. Genant, "A comparison of spinal quantitative computed tomography with dual energy X-ray absorptiometry in European women with vertebral and nonvertebral fractures.," *Calcified tissue international*, vol. 68, pp. 74–82, feb 2001.

[48] C. Schouten, G. J. Meijer, J. J. van den Beucken, P. H. Spauwen, and J. A. Jansen, "The quantitative assessment of peri-implant bone responses using histomorphometry and micro-computed tomography," *Biomaterials*, vol. 30, pp. 4539–4549, sep 2009.

[49] T. Hildebrand and P. Ruegsegger, "A new method for the model-independent assessment of thickness in three-dimensional images," *Journal of Microscopy*, vol. 185, pp. 67–75, jan 1997.

[50] G. J. Kazakia and S. Majumdar, "New imaging technologies in the diagnosis of osteoporosis," *Reviews in Endocrine and Metabolic Disorders*, vol. 7, no. 1-2, pp. 67–74, 2007.

[51] B. Cortet, N. Boutry, P. Dubois, P. Bourel, A. Cotten, and X. Marchandise, "In Vivo Comparison Between Computed Tomography and Magnetic Resonance Image

Analysis of the Distal Radius in the Assessment of Osteoporosis," *Journal of Clinical Densitometry*, vol. 3, no. 1, pp. 15–26, 2000.

[52] F. W. Wehrli, M. B. Leonard, P. K. Saha, and B. R. Gomberg, "Quantitative high-resolution magnetic resonance imaging reveals structural implications of renal osteodystrophy on trabecular and cortical bone," *Journal of Magnetic Resonance Imaging*, vol. 20, pp. 83–89, jul 2004.

[53] F. W. Wehrli, B. R. Gomberg, P. K. Saha, H. K. Song, S. N. Hwang, and P. J. Snyder, "Digital Topological Analysis of In Vivo Magnetic Resonance Microimages of Trabecular Bone Reveals Structural Implications of Osteoporosis," *Journal of Bone and Mineral Research*, vol. 16, pp. 1520–1531, aug 2001.

[54] M. Benito, B. Gomberg, F. W. Wehrli, R. H. Weening, B. Zemel, A. C. Wright, H. K. Song, A. Cucchiara, and P. J. Snyder, "Deterioration of Trabecular Architecture in Hypogonadal Men," *The Journal of Clinical Endocrinology & Metabolism*, vol. 88, no. 4, pp. 1497–1502, 2003.

[55] J. S. Bauer, T. M. Link, C. Bergot, M. Hausard, A. Sautet, J. Laredo, H. Genant, and S. Cummings, "Advances in osteoporosis imaging.," *European journal of radiology*, vol. 71, no. 3, pp. 440–9, 2009.

[56] Scanco Medical, "HRpQCT : Systems & Solutions : Scanco Medical: micro CT scanners, image analysis software, microtomography scan services."

[57] "Guidelines for assessment of bone microstructure in rodents using micro-computed tomography," vol. 25, pp. 1468–1486, jul 2010.

[58] J. A. Macneil, S. K. Boyd, S. Majumdar, L. Lanyon, R. Poss, N. Portero-Muzy, and P. Delmas, "Bone strength at the distal radius can be estimated from high-resolution peripheral quantitative computed tomography and the finite element method.," *Bone*, vol. 42, pp. 1203–13, jun 2008.

[59] A. J. Burghardt, A. S. Issever, A. V. Schwartz, K. A. Davis, U. Masharani, S. Majumdar, and T. M. Link, "High-Resolution Peripheral Quantitative Computed Tomographic Imaging of Cortical and Trabecular Bone Microarchitecture in Patients with Type 2 Diabetes Mellitus," *The Journal of Clinical Endocrinology & Metabolism*, vol. 95, pp. 5045–5055, nov 2010.

[60] E. Sornay-Rendu, S. Boutroy, F. Munoz, and P. D. Delmas, "Alterations of Cortical and Trabecular Architecture Are Associated With Fractures in Postmenopausal Women, Partially Independent of Decreased BMD Measured by DXA: The OFELY Study," *Journal of Bone and Mineral Research*, vol. 22, pp. 425–433, mar 2007.

[61] E. Sornay-Rendu, J.-L. Cabrera-Bravo, S. Boutroy, F. Munoz, and P. D. Delmas, "Severity of Vertebral Fractures Is Associated With Alterations of Cortical Architecture in Postmenopausal Women," *Journal of Bone and Mineral Research*, vol. 24, pp. 737–743, apr 2009.

[62] X. S. Liu, E. M. Stein, B. Zhou, C. A. Zhang, T. L. Nickolas, A. Cohen, V. Thomas, D. J. McMahon, F. Cosman, J. Nieves, E. Shane, and X. E. Guo, "Individual trabecula segmentation (ITS)-based morphological analyses and microfinite element analysis of HR-pQCT images discriminate postmenopausal fragility fractures independent of DXA measurements.," *Journal of bone and mineral research : the official journal of the American Society for Bone and Mineral Research*, vol. 27, pp. 263–72, feb 2012.

[63] E. J. Atkinson, T. M. Therneau, L. J. Melton, J. J. Camp, S. J. Achenbach, S. Amin, S. Khosta, and S. Khosla, "Assessing fracture risk using gradient boosting machine (GBM) models.," *Journal of bone and mineral research : the official journal of the American Society for Bone and Mineral Research*, vol. 27, pp. 1397–404, jun 2012.

[64] L. J. Melton, B. L. Riggs, G. H. van Lenthe, S. J. Achenbach, R. Müller, M. L. Bouxsein, S. Amin, E. J. Atkinson, and S. Khosla, "Contribution of In Vivo Structural Measurements and Load/Strength Ratios to the Determination of Forearm Fracture Risk in Postmenopausal Women," *Journal of Bone and Mineral Research*, vol. 22, pp. 1442–1448, may 2007.

[65] L. Vico, M. Zouch, A. Amirouche, D. Frère, N. Laroche, B. Koller, A. Laib, T. Thomas, and C. Alexandre, "High-Resolution pQCT Analysis at the Distal Radius and Tibia Discriminates Patients With Recent Wrist and Femoral Neck Fractures," *Journal of Bone and Mineral Research*, vol. 23, pp. 1741–1750, nov 2008.

[66] E. M. Stein, X. S. Liu, T. L. Nickolas, A. Cohen, V. Thomas, D. J. McMahon, C. Zhang, P. T. Yin, F. Cosman, J. Nieves, X. E. Guo, and E. Shane, "Abnormal microarchitecture and reduced stiffness at the radius and tibia in postmenopausal women with fractures.," *Journal of bone and mineral research : the official journal of the American Society for Bone and Mineral Research*, vol. 25, pp. 2572–81, dec 2010.

[67] S. Boutroy, B. Van Rietbergen, E. Sornay-Rendu, F. Munoz, M. L. Bouxsein, and P. D. Delmas, "Finite Element Analysis Based on In Vivo HR-pQCT Images of the Distal Radius Is Associated With Wrist Fracture in Postmenopausal Women," *Journal of Bone and Mineral Research*, vol. 23, pp. 392–399, nov 2007.

[68] N. Vilayphiou, S. Boutroy, E. Sornay-rendu, B. Van rietbergen, F. Munoz, P. D. Delmas, and R. Chapurlat, "Finite element analysis performed on radius and tibia HR-pQCT images and fragility fractures at all sites in postmenopausal women," *Bone*, vol. 46, pp. 1030–1037, apr 2010.

[69] N. Vilayphiou, S. Boutroy, P. Szulc, B. van Rietbergen, F. Munoz, P. D. Delmas, and R. Chapurlat, "Finite element analysis performed on radius and tibia HR-pQCT images and fragility fractures at all sites in men," *Journal of Bone and Mineral Research*, vol. 26, pp. 965–973, may 2011.

[70] C. Graeff, F. Marin, H. Petto, O. Kayser, A. Reisinger, J. Peña, P. Zysset, and C.-C. Glüer, "High resolution quantitative computed tomography-based assessment of trabecular microstructure and strength estimates by finite-element analysis of the spine, but not DXA, reflects vertebral fracture status in men with glucocorticoid-induced osteoporosis," *Bone*, vol. 52, pp. 568–577, feb 2013.

[71] N. Otsu, "A Threshold Selection Method from Gray-Level Histograms," *IEEE Transactions on Systems, Man, and Cybernetics*, vol. 9, pp. 62–66, jan 1979.

[72] S. L. S. Abdullah, H. Hambali, and N. Jamil, "Segmentation of Natural Images Using an Improved Thresholding-Based Technique," *Procedia Engineering*, vol. 41, pp. 938–944, 2012.

[73] S. Aja-Fernández, A. H. Curiale, and G. Vegas-Sánchez-Ferrero, "A local fuzzy thresholding methodology for multiregion image segmentation," *Knowledge-Based Systems*, vol. 83, pp. 1–12, jul 2015.

[74] L. Jianzhuang, L. Wenqing, and T. Yupeng, "Automatic thresholding of gray-level pictures using two-dimension Otsu method," in *IEEE International Conference of Circuits and Systems*, pp. 325–327, 1991.

[75] T. Kanungo, D. Mount, N. Netanyahu, C. Piatko, R. Silverman, and A. Wu, "An efficient k-means clustering algorithm: analysis and implementation," *IEEE Transactions on Pattern Analysis and Machine Intelligence*, vol. 24, pp. 881–892, jul 2002.

[76] M. Li, M. Ng, Y.-m. Cheung, and J. Huang, "Agglomerative Fuzzy K-Means Clustering Algorithm with Selection of Number of Clusters," *IEEE Transactions on Knowledge and Data Engineering*, vol. 20, pp. 1519–1534, nov 2008.

[77] N. Mat Isa, S. Salamah, and U. Ngah, "Adaptive fuzzy moving K-means clustering algorithm for image segmentation," *IEEE Transactions on Consumer Electronics*, vol. 55, pp. 2145–2153, nov 2009.

[78] J. Wang and X. Su, "An improved K-Means clustering algorithm," in *2011 IEEE 3rd International Conference on Communication Software and Networks*, pp. 44–46, IEEE, may 2011.

[79] S. Panda, S. Sahu, P. Jena, and S. Chattopadhyay, "Comparing fuzzy-C means and K-means clustering techniques: A comprehensive study," in *Advances in Intelligent and Soft Computing*, vol. 166 AISC, pp. 451–460, Springer, Berlin, Heidelberg, 2012.

[80] J. Jianbo Shi and J. Malik, "Normalized cuts and image segmentation," *IEEE Transactions on Pattern Analysis and Machine Intelligence*, vol. 22, no. 8, pp. 888–905, 2000.

[81] Y. Boykov and G. Funka-Lea, "Graph cuts and efficient N-D image segmentation," *International Journal of Computer Vision*, vol. 70, pp. 109–131, nov 2006.

[82] S. Beucher and C. Lantuéjoul, "Use of watersheds in contour detection," *International workshop on image processing, real-time edge and motion detection*, 1979.

[83] A. A. Yahya, J. Tan, and M. Hu, "A novel model of image segmentation based on watershed algorithm," *Advances in Multimedia*, vol. 2013, pp. 1–8, sep 2013.

[84] D. Mumford and J. Shah, "Optimal approximations by piecewise smooth functions and associated variational problems," *Communications on Pure and Applied Mathematics*, vol. 42, pp. 577–685, jul 1989.

[85] T. F. Chan and L. A. Vese, "Active contours without edges," *IEEE transactions on Image processing*, vol. 10, no. 2, pp. 266–277, 2001.

[86] N. Paragios and R. Deriche, "Geodesic Active Regions and Level Set Methods for Supervised Texture Segmentation," *International Journal of Computer Vision*, vol. 46, no. 3, pp. 223–247, 2002.

[87] M. Kass, A. Witkin, and D. Terzopoulos, "Snakes: Active contour models," *International Journal of Computer Vision*, vol. 1, pp. 321–331, jan 1988.

[88] H. Delingette and J. Montagnat, "Shape and Topology Constraints on Parametric Active Contours," *Computer Vision and Image Understanding*, vol. 83, pp. 140–171, aug 2001.

[89] S. Osher and J. A. Sethian, "Fronts propagating with curvature-dependent speed: Algorithms based on Hamilton-Jacobi formulations," *Journal of Computational Physics*, vol. 79, pp. 12–49, nov 1988.

[90] J. Sethian, "Tracking Interfaces with Level Sets: An "act of violence" helps solve evolving interface problems in geometry, fluid mechanics, robotic navigation and materials sciences," in *Sigma Xi, The Scientific Research Society*, vol. 85, p. 10, Sigma Xi, The Scientific Research Society, 1997.

[91] R. Malladi, J. Sethian, and B. Vemuri, "Shape modeling with front propagation: a level set approach," *IEEE Transactions on Pattern Analysis and Machine Intelligence*, vol. 17, no. 2, pp. 158–175, 1995.

[92] A. Yezzi, S. Kichenassamy, A. Kumar, P. Olver, and A. Tannenbaum, "A geometric snake model for segmentation of medical imagery," *IEEE Transactions on Medical Imaging*, vol. 16, pp. 199–209, apr 1997.

[93] V. Caselles, F. Catté, T. Coll, and F. Dibos, "A geometric model for active contours in image processing," *Numerische Mathematik*, vol. 66, pp. 1–31, dec 1993.

[94] R. Malladi and J. A. Sethian, "Image processing via level set curvature flow.," *Proceedings of the National Academy of Sciences of the United States of America*, vol. 92, pp. 7046–50, jul 1995.

[95] F. S. Cohen and Z. Fan, "Maximum likelihood unsupervised textured image segmentation," *CVGIP: Graphical Models and Image Processing*, vol. 54, pp. 239–251, may 1992.

[96] V. Caselles, R. Kimmel, and G. Sapiro, "Geodesic Active Contours," *International Journal of Computer Vision*, vol. 22, no. 1, pp. 61–79, 1997.

[97] V. Caselles, R. Kimmel, and G. Sapiro, "Geodesic active contours," *Proceedings of IEEE International Conference on Computer Vision*, vol. 10, no. 10, pp. 694–699, 2001.

[98] S. Kichenassamy, A. Kumar, P. Olver, A. Tannenbaum, and A. Yezzi, "Gradient flows and geometric active contour models," *Proceedings of IEEE International Conference on Computer Vision*, pp. 4–9, 1995.

[99] G. Sapiro and Guillermo, "Color Snakes," *Computer Vision and Image Understanding*, vol. 68, pp. 247–253, nov 1997.

[100] G. Aubert and L. Blanc-Féraud, "An Elementary Proof of the Equivalence between 2D and 3D Classical Snakes and Geodesic Active Contours," Tech. Rep. RR-3340, INRIA, Jan. 1998.

[101] G. Aubert and L. Blanc-Féraud, "Some Remarks on the Equivalence between 2D and 3D Classical Snakes and Geodesic Active Contours," *International Journal of Computer Vision*, vol. 34, no. 1, pp. 19–28, 1999.

[102] C. Xu, A. Yezzi, and J. L. Prince, "A summary of geometric level-set analogues for a general class of parametric active contour and surface models," in *Proceedings - IEEE Workshop on Variational and Level Set Methods in Computer Vision, VLSM 2001*, pp. 104–111, IEEE Computer Soc, 2001.

[103] C. Xu, J. Yezzi, a., and J. Prince, "On the relationship between parametric and geometric active contours," *Conference Record of the Thirty-Fourth Asilomar Conference on Signals, Systems and Computers (Cat. No.00CH37154)*, vol. 1, no. October, pp. 483–489, 2000.

[104] A. Pratondo, C.-K. Chui, and S.-H. Ong, "Robust Edge-Stop Functions for Edge-Based Active Contour Models in Medical Image Segmentation," *IEEE Signal Processing Letters*, vol. 23, pp. 222–226, feb 2016.

[105] T. Chan and L. Vese, "An Active Contour Model without Edges," pp. 141–151, Springer, Berlin, Heidelberg, 1999.

[106] T. Chan and L. Vese, "Active contours without edges," *IEEE Transactions on Image Processing*, vol. 10, no. 2, pp. 266–277, 2001.

[107] D. H. U. Mumford and J. N. U. Shah, "Boundary detection by minimizing functionals," in *IEEE Conference on Computer Vision and Pattern Recognition*, vol. 17, pp. 137–154, 1985.

[108] L. Vese, "Multiphase Object Detection and Image Segmentation," in *Geometric Level Set Methods in Imaging, Vision, and Graphics*, pp. 175–194, New York: Springer-Verlag, 2003.

[109] A. Tsai, A. Yezzi, and A. Willsky, "A curve evolution approach to smoothing and segmentation using the Mumford-Shah functional," in *Proceedings IEEE Conference on Computer Vision and Pattern Recognition. CVPR 2000 (Cat. No.PR00662)*, vol. 1, pp. 119–124, IEEE Comput. Soc, 2000.

[110] A. Tsai, A. Yezzi, and A. Willsky, "Curve evolution implementation of the Mumford-Shah functional for image segmentation, denoising, interpolation, and magnification," *IEEE Transactions on Image Processing*, vol. 10, no. 8, pp. 1169–1186, 2001.

[111] T. F. Chan and L. A. Vese, "Image segmentation using level sets and the piecewise-constant mumford-shah model," tech. rep., Computational Applied Math Group, 2000.

[112] Chunming Li, Chiu-Yen Kao, J. Gore, and Zhaohua Ding, "Minimization of Region-Scalable Fitting Energy for Image Segmentation," *IEEE Transactions on Image Processing*, vol. 17, pp. 1940–1949, Oct. 2008.

[113] S. Lankton and A. Tannenbaum, "Localizing Region-Based Active Contours," *IEEE Transactions on Image Processing*, vol. 17, pp. 2029–2039, Nov. 2008.

[114] X.-F. Wang, D.-S. Huang, and H. Xu, "An efficient local Chan–Vese model for image segmentation," *Pattern Recognition*, vol. 43, pp. 603–618, mar 2010.

[115] C. Li, C.-Y. Kao, J. C. Gore, and Z. Ding, "Implicit Active Contours Driven by Local Binary Fitting Energy," in *2007 IEEE Conference on Computer Vision and Pattern Recognition*, pp. 1–7, IEEE, jun 2007.

[116] Chunming Li, Chiu-Yen Kao, J. Gore, and Zhaohua Ding, "Minimization of Region-Scalable Fitting Energy for Image Segmentation," *IEEE Transactions on Image Processing*, vol. 17, pp. 1940–1949, oct 2008.

[117] S. Lankton and A. Tannenbaum, "Localizing Region-Based Active Contours," *IEEE Transactions on Image Processing*, vol. 17, pp. 2029–2039, nov 2008.

[118] W. Liu, Y. Shang, and X. Yang, "Active contour model driven by local histogram fitting energy," *Pattern Recognition Letters*, vol. 34, pp. 655–662, apr 2013.

[119] C. He, Y. Wang, and Q. Chen, "Active contours driven by weighted region-scalable fitting energy based on local entropy," *Signal Processing*, vol. 92, pp. 587–600, feb 2012.

[120] A. Shiozaki, "Edge extraction using entropy operator," *Computer Vision, Graphics, and Image Processing*, vol. 36, pp. 1–9, oct 1986.

[121] A. Yezzi, A. Tsai, and A. Willsky, "A Fully Global Approach to Image Segmentation via Coupled Curve Evolution Equations," *Journal of Visual Communication and Image Representation*, vol. 13, pp. 195–216, mar 2002.

[122] A. Bhattacharyya, "On a Measure of Divergence between Two Multinomial Populations," vol. 7, no. 4, pp. 401–406, 1946.

[123] O. Michailovich, Y. Rathi, and A. Tannenbaum, "Image Segmentation Using Active Contours Driven by the Bhattacharyya Gradient Flow," *IEEE Transactions on Image Processing*, vol. 16, pp. 2787–2801, nov 2007.

[124] N. Paragios and R. Deriche, "Geodesic Active Regions: A New Framework to Deal with Frame Partition Problems in Computer Vision," *Journal of Visual Communication and Image Representation*, vol. 13, pp. 249–268, mar 2002.

[125] N. Paragios and S. A. Cedex, "Unifying Boundary and Region-based information for Geodesic Active Tracking," in *Proc. Comput. Vis. Patt. Recog.*, pp. 300–305, IEEE Comput. Soc, 2004.

[126] N. Paragiosl and R. Deriche, "Coupled Geodesic Active Regions for Image Segmentation : A Level Set Approach," in *Computer Vision—ECCV 2000. Springer Berlin Heidelberg*, pp. 224–240, Springer, Berlin, Heidelberg, 2000.

[127] S. Jehan-Besson, M. Gastaud, M. Borland, and G. Aubert, "Region-based active contours using geometrical and statistical features for image segmentation," in *Proceedings 2003 International Conference on Image Processing (Cat. No.03CH37429)*, vol. 3, pp. II–643–6, IEEE, 2003.

[128] Jehan-Besson, Barlaud, Aubert, and Faugeras, "Shape gradients for histogram segmentation using active contours," in *Proceedings Ninth IEEE International Conference on Computer Vision*, pp. 408–415 vol.1, IEEE, 2003.

[129] K. Zhang, L. Zhang, H. Song, and W. Zhou, "Active contours with selective local or global segmentation: A new formulation and level set method," *Image and Vision Computing*, vol. 28, pp. 668–676, apr 2010.

[130] Q. Thieu, M. Luong, J.-M. Rocchisani, N. Sirakov, and E. Viennet, "Segmentation by a Local and Global Fuzzy Gaussian Distribution Energy Minimization of an Active Contour Model," in *IWCIA 2012: Proceedings of the 15th International Workshop on Combinatorial Image Analysis*, vol. 7655, pp. 298–312, Springer, Berlin, Heidelberg, nov 2012.

[131] K. K. Shyu, V. T. Pham, T. T. Tran, and P. L. Lee, "Global and local fuzzy energy-based active contours for image segmentation," *Nonlinear Dynamics*, vol. 67, no. 2, pp. 1559–1578, 2012.

[132] T. Liu, H. Xu, W. Jin, Z. Liu, Y. Zhao, and W. Tian, "Medical image segmentation based on a hybrid region-based active contour model," *Computational and Mathematical Methods in Medicine*, vol. 2014, p. 890725, 2014.

[133] S. Zhou, J. Wang, S. Zhang, Y. Liang, and Y. Gong, "Active contour model based on local and global intensity information for medical image segmentation," *Neurocomputing*, vol. 186, pp. 107–118, apr 2016.

[134] M. Rousson, T. Brox, and R. Deriche, "Active unsupervised texture segmentation on a diffusion based feature space," in *EEE Computer Society Conference on Computer Vision and Pattern Recognition*, vol. 2, pp. II–699–704 vol.2, IEEE Comput. Soc, 2003.

[135] W. Förstner and E. Gülch, "A Fast Operator for Detection and Precise Location of Distinct Points, Corners and Centres of Circular Features," 1987.

[136] J. Bigun, G. Granlund, and J. Wiklund, "Multidimensional orientation estimation with applications to texture analysis and optical flow," *IEEE Transactions on Pattern Analysis and Machine Intelligence*, vol. 13, no. 8, pp. 775–790, 1991.

[137] J. Weickert and T. Brox, "Diffusion and regularization of vector- and matrix-valued images," *Inverse problems, image analysis, and medical imaging*, vol. 313, pp. 251–268, 2002.

[138] Chen Sagiv, N. Sochen, and Y. Zeevi, "Integrated active contours for texture segmentation," *IEEE Transactions on Image Processing*, vol. 15, pp. 1633–1646, jun 2006.

[139] a. K. Jain and F. Farrokhnia, "Unsupervised texture segmentation using Gabor filters," *Systems, Man and Cybernetics, 1990. Conference Proceedings., IEEE International Conference on*, vol. 000, pp. 14–19, 1990.

[140] N. Sochen, R. Kimmel, and R. Malladi, "A general framework for low level vision," *IEEE Transactions on Image Processing*, vol. 7, pp. 310–318, mar 1998.

[141] T. Ojala, M. Pietikainen, and T. Maenpaa, "Multiresolution gray-scale and rotation invariant texture classification with local binary patterns," *IEEE Transactions on Pattern Analysis and Machine Intelligence*, vol. 24, pp. 971–987, jul 2002.

[142] Qinggang Wu, Jubai An, and Bin Lin, "A Texture Segmentation Algorithm Based on PCA and Global Minimization Active Contour Model for Aerial Insulator Images," *IEEE Journal of Selected Topics in Applied Earth Observations and Remote Sensing*, vol. 5, pp. 1509–1518, oct 2012.

[143] D. Reska, C. Boldak, and M. Kretowski, "A Texture-Based Energy for Active Contour Image Segmentation," in *Advances in Intelligent Systems and Computing*, vol. 313 AISC, pp. 187–194, Springer, Cham, 2015.

[144] M. Li, Y. Tang, L. Wang, and Z. Shi, "Fractal active contour model for segmenting the boundary of man-made target in nature scenes," in *Proceedings of the SPIE, Volume 6150, id. 615053 (2006).* (X. Hou, J. Yuan, J. C. Wyant, H. Wang, and S. Han, eds.), vol. 6150, p. 615053, feb 2006.

[145] A. Tatu and S. Bansal, "A Novel Active Contour Model for Texture Segmentation," *Energy Minimization Methods Computer Vision Pattern Recognition*, pp. 223–236, 2015.

[146] S. Krinidis and V. Chatzis, "Fuzzy Energy-Based Active Contours," *IEEE Transactions on Image Processing*, vol. 18, pp. 2747–2755, dec 2009.

[147] Y. Yu, C. Zhang, Y. Wei, and X. Li, "Active contour method combining local fitting energy and global fitting energy dynamically," in *Lecture Notes in Computer Science (including subseries Lecture Notes in Artificial Intelligence and Lecture Notes in Bioinformatics)*, vol. 6165 LNCS, pp. 163–172, Springer, Berlin, Heidelberg, 2010.

[148] Q. T. Thieu, M. Luong, J.-M. Rocchisani, N. M. Sirakov, and E. Viennet, "Efficient segmentation with the convex local-global fuzzy Gaussian distribution active contour for medical applications," *Annals of Mathematics and Artificial Intelligence*, vol. 75, pp. 249–266, oct 2015.

[149] K.-K. Shyu, V.-T. Pham, T.-T. Tran, and P.-L. Lee, "Global and local fuzzy energy-based active contours for image segmentation," *Springer Nonlinear Dynamics*, vol. 67, pp. 1559–1578, jan 2012.

[150] K.-K. Shyu, T.-T. Tran, V.-T. Pham, P.-L. Lee, and L.-J. Shang, "Fuzzy distribution fitting energy-based active contours for image segmentation," *Springer Nonlinear Dynamics*, vol. 69, pp. 295–312, jul 2012.

[151] H. R. Buie, G. M. Campbell, R. J. Klinck, J. A. MacNeil, and S. K. Boyd, "Automatic segmentation of cortical and trabecular compartments based on a dual threshold technique for in vivo micro-CT bone analysis," *Elsevier Bone*, vol. 41, no. 4, pp. 505–515, 2007.

[152] A. J. Burghardt, H. R. Buie, A. Laib, S. Majumdar, and S. K. Boyd, "Reproducibility of direct quantitative measures of cortical bone microarchitecture of the distal radius and tibia by HR-pQCT," *Elsevier Bone*, vol. 47, no. 3, pp. 519–528, 2010.

[153] A. Laib and P. Rüegsegger, "Comparison of structure extraction methods for in vivo trabecular bone measurements," *Computerized Medical Imaging and Graphics*, vol. 23, no. 2, pp. 69–74, 1999.

[154] A. Valentinitsch, J. M. Patsch, J. Deutschmann, C. Schueller-Weidekamm, H. Resch, F. Kainberger, and G. Langs, "Automated threshold-independent cortex segmentation by 3D-texture analysis of HR-pQCT scans," *Bone*, vol. 51, pp. 480–487, apr 2012.

[155] A. Valentinitsch, J. Patsch, D. Mueller, F. Kainberger, and G. Langs, "Texture analysis in quantitative osteoporosis assessment: Characterizing microarchitecture," in *2010 7th IEEE International Symposium on Biomedical Imaging: From Nano to Macro, ISBI 2010 - Proceedings*, pp. 1361–1364, IEEE, 2010.

[156] R. M. Haralick, K. Shanmugam, and I. Dinstein, "Textural Features for Image Classification," *IEEE Transactions on Systems, Man, and Cybernetics*, vol. SMC-3, no. 6, pp. 610–621, 1973.

[157] V. Kovalev, F. Kruggel, H.-J. Gertz, and D. von Cramon, "Three-dimensional texture analysis of MRI brain datasets," *IEEE Transactions on Medical Imaging*, vol. 20, pp. 424–433, may 2001.

[158] Y. Sato, S. Nakajima, N. Shiraga, H. Atsumi, S. Yoshida, T. Koller, G. Gerig, and R. Kikinis, "Three-dimensional multi-scale line filter for segmentation and visualization of curvilinear structures in medical images.," *Medical Image Analysis*, vol. 2, pp. 143–68, jun 1998.

[159] A. F. Frangi, W. J. Niessen, K. L. Vincken, and M. A. Viergever, "Multiscale vessel enhancement filtering," pp. 130–137, Springer, Berlin, Heidelberg, oct 1998.

[160] R. Zebaze, A. Ghasem-Zadeh, A. Mbala, and E. Seeman, "A new method of segmentation of compact-appearing, Transitional and trabecular compartments and quantification of cortical porosity from high resolution peripheral quantitative computed tomographic images," *Bone*, vol. 54, pp. 8–20, may 2013.

[161] D. D. Thompson, "Age changes in bone mineralization, cortical thickness, and haversian canal area.," *Springer, Calcified Tissue International*, vol. 31, no. 1, pp. 5–11, 1980.

[162] S. Qiu, D. P. Fyhrie, S. Palnitkar, and D. S. Rao, "Histomorphometric assessment of Haversian canal and osteocyte lacunae in different-sized osteons in human rib," *The Anatomical Record*, vol. 272A, no. 2, pp. 520–525, 2003.

[163] J. B. Pialat, A. J. Burghardt, M. Sode, T. M. Link, and S. Majumdar, "Visual grading of motion induced image degradation in high resolution peripheral computed tomography: Impact of image quality on measures of bone density and micro-architecture," *Bone*, vol. 50, pp. 111–118, jan 2012.

[164] P. A. Yushkevich, J. Piven, H. C. Hazlett, R. G. Smith, S. Ho, J. C. Gee, and G. Gerig, "User-guided 3d active contour segmentation of anatomical structures: significantly improved efficiency and reliability," *Elsevier NeuroImage*, vol. 31, no. 3, pp. 1116–1128, 2006.

[165] L. R. Dice, "Measures of the Amount of Ecologic Association Between Species," *Ecology*, vol. 26, no. 3, p. 297, 1945.

[166] P. Cignoni, C. Rocchini, and R. Scopigno, "Metro: measuring error on simplified surfaces," in *Computer Graphics Forum*, vol. 17, pp. 167–174, Wiley Online Library, 1998.

[167] N. Aspert, D. Santa Cruz, and T. Ebrahimi, "Mesh: measuring errors between surfaces using the hausdorff distance.," in *International Conference in Multimedia and ExpoICME (1)*, pp. 705–708, 2002.

[168] S. Krinidis and V. Chatzis, "Fuzzy Energy-Based Active Contours," *IEEE Transactions on Image Processing*, vol. 18, no. 12, pp. 2747–2755, 2009.